# A Fourier Description of Covariance, and Separation of Simultaneously Encoded Slices with In-Plane Acceleration in fMRI

Mary C. Kociuba
*Marquette University*

# A FOURIER DESCRIPTION OF COVARIANCE, AND SEPARATION OF SIMULTANEOUSLY ENCODED SLICES WITH IN-PLANE ACCELERATION IN FMRI

by

Mary C. Kociuba

A Dissertation submitted to the Faculty of the Graduate School,
Marquette University,
in Partial Fulfillment of the Requirements
for the Degree of Doctor of Philosophy

Milwaukee, WI

December 2016

ABSTRACT
A FOURIER DESCRIPTION OF COVARIANCE, AND SEPARATION OF SIMULTANEOUSLY ENCODED SLICES WITH IN-PLANE ACCELERATION IN FMRI

Mary C. Kociuba

Marquette University, 2016

Functional magnetic resonance imaging (fMRI) studies aim to identify localized neural regions associated with a cognitive task performed by the subject. An indirect measure of the brain activity is the blood oxygenation level dependent (BOLD) signal fluctuations observed within the complex-valued spatial frequencies measured over time. The standard practice in fMRI is to discard the phase information after image reconstruction, even with evidence of biological task-related change in the phase time-series. In the first aim of this dissertation, a complex-valued time-series covariance is derived as a linear combination of second order temporal Fourier frequency coefficients. As opposed to magnitude-only analysis, the complex-valued covariance increases the sensitivity and specificity in fMRI correlation analysis, which is particularly advantageous for low contrast-to-noise ratio (CNR) fMRI time-series. In the remaining aims, increased statistical significance is achieved through a higher sampling rate of the fMRI time-course, by simultaneously magnetizing multiple slice images. With multi-frequency band excitations, a single *k*-space readout reconstructs to an image of composite aliased slice images. To disentangle the signal, or aliased voxels, phase and coil encoding techniques are incorporated into the data acquisition and image reconstruction. Inter-slice signal leakage, which also manifests as improper placement of the BOLD signal, presents in the separated slice images from induced correlations as a result of suboptimal simultaneous multi-slice (SMS) reconstruction methods. In the second aim of this dissertation, the Multi-coil Separation of Parallel Encoded Complex-valued Slices (mSPECS) reconstruction method is proposed as a solution to preserve the activation statistics in the separated slice images through a Bayesian approach of sampling calibration images. In the third aim of this dissertation, the mSPECS reconstruction is extended to include In-Plane Acceleration (mSPECS-IPA), to reconstruct aliased slice images with additional in-plane subsampling using a two-dimensional orthogonal phase encoding derivation of Hadamard encoding. Mitigating induced correlations with mSPECS(-IPA), results in accurately placed functional activation in the previously aliased complex-valued slice images. The development of novel complex-valued analysis and reconstruction methods in fMRI strengthens the significance of the activation statistics and precludes inter-slice signal leakage, so the true underlying neural dynamics are modeled in complex-valued fMRI data analysis.

TABLE OF CONTENTS

# LIST OF TABLES

# LIST OF FIGURES

# Chapter 1: Introduction

## 1.1 Motivation

Functional magnetic resonance imaging (fMRI) is a noninvasive technique to map and characterize brain activity through time. Across the magnetic resonance (MR) imaging pipeline of acquisition, reconstruction, processing, and analysis, the optimization of each step is central to motivate the use of fMRI in clinical applications along with accurate modeling of population neural dynamics. The standard in fMRI is to discard the phase before the statistical analysis of the data, despite evidence of biologically induced task related change in the phase time-series. The primary research goal of this dissertation is to develop novel statistical methods in complex-valued fMRI correlation analysis and simultaneous multi-slice functional magnetic resonance imaging (SMS-fMRI) reconstruction methods.

In this dissertation, the increased sensitivity and specificity of complex-valued time-series correlation analysis in fMRI, versus the standard of a magnitude-only time-series correlation analysis, is demonstrated with a temporal Fourier frequency description of covariance. A key motivation for including the phase information in correlation analysis is to utilize task information from low contrast-to-noise ratio (CNR) fMRI data sets. The noise in the phase time-series also scales relative to the signal-to-noise ratio (SNR), as . Improving the significance of fMRI activation statistics in data with relatively high noise variability reduces the extent signal processing is required to examine the

signal of interest, and thus avoiding processing induced correlations, so the true underlying signal of interest can be examined in the fMRI statistical analysis.

A higher sampling rate of slice images in MR is possible with parallel imaging methods or simultaneously magnetizing multiple slice images, and corresponds to increased statistical significance in fMRI analysis. Often fast image acquisition and reconstruction methods focus on speed rather than accuracy. Correlation induced from substandard aliased slice image separation, presenting as "clusters" of false activation, is a substantial obstacle in SMS-fMRI acquisition and reconstruction schemes. In this dissertation, a complex-valued SMS-fMRI reconstruction method, Multi-coil Separation of Parallel Encoded Complex-valued Slice (mSPECS), is developed to separate simultaneously excited slice images while preserving the fMRI blood oxygenation level dependent (fMRI-BOLD) signal in the separated fMRI time-series. The mSPECS model is extended to include additional In-Plane Acceleration (mSPECS-IPA), the mSPECS-IPA reconstruction method, through a novel orthogonal 2-dimensional Hadamard phase encoding of the aliased measured slice images with subsampling in-plane and aliasing through-plane. Reducing the scan time required to measure the signal in MR without sacrificing image quality, is one of the prominent research challenges in modern MRI. The development of SMS-fMRI reconstruction methods, to yield high spatial and temporal resolution, is critical for accurate whole brain image volume mapping and advancing the field of fast imaging methods in fMRI.

## 1.2 Aims

### 1.2.1 Aim 1: A Fourier Description of Covariance

The goal of the first aim of this dissertation is to develop a linear matrix representation of correlation between the complex-valued time-series of voxels in the temporal Fourier frequency domain. With a real-valued isomorphism representation of Fourier reconstruction, complex-valued correlation is computed in the voxel temporal frequency domain with complex-valued time-series data, rather than with the standard of time-series correlation of magnitude only data. The advantage of the framework is demonstrated through a comparison of the sensitivity and specificity of complex-valued time-series correlation to magnitude-only time-series correlation in simulation with surfaces representing varying magnitude and phase CNR values. The framework is also demonstrated with experimental human subject fMRI data, where the magnitude-only and complex-valued time-series for low and high CNR voxels are examined.

### 1.2.2 Aim 2: mSPECS

The goal of the second aim of this dissertation is to develop an SMS-fMRI reconstruction method, mSPECS, to minimize residual artifacts from un-aliasing of slice images throughout a time-series, so the BOLD signal in the separated slice images is placed in the proper slice. Improving temporal resolution while mitigating inter-slice signal leakage is a significant challenge of SMS imaging in fMRI. Inter-slice signal

leakage manifests as “clusters” of false activations or as residual anatomical structure in previously aliased regions. Fast imaging methods often focus on speed with little attention to the statistical implications of SMS acquisition and reconstruction methods. To implement the mSPECS slice image separation method, the SMS-fMRI time-series is acquired with a Hadamard multi-frequency band (MB) pulse sequence, which simultaneously magnetizes multiple slice images with a modulated phase encoding of the complex-valued slice images. The mSPECS method combines orthogonal square Hadamard matrices with the coil and phase encoding of the measured aliased slice images, and a bootstrap sampling algorithm to disentangle the complex-valued aliased slice images at each time point in the fMRI time-series. The mSPECS reconstruction method is demonstrated by computing the activation statistics, in a simulated complex-valued fMRI time-series and using artificially aliased complex-valued experimental human subject fMRI data, for acceleration factors up to 8. This speed-up of the acquisition is ideal to achieve a higher sampling rate of slice images, and hence voxel time points, increasing the sensitivity of fMRI activation statistics in the fMRI time-series analysis, allowing faster observation of brain function.

### 1.2.3 Aim 3: mSPECS-IPA

The goal of the third aim of this dissertation is to integrate in-plane subsampling within mSPECS, to develop the mSPECS-IPA reconstruction method. An increased acceleration is achieved by separating aliased slice images with mSPECS-IPA from omitting spatial frequency measurements in the *k*-space readout, which results in wrap

around artifacts in the raw reconstructed slice image. The mSPECS-IPA reconstruction method simultaneously unstacks complex-valued slice images through-plane, unwraps the complex-valued slice images in-plane, and combines the complex-valued coil images with a strategic phase encoding of the aliased slice images. The method employs 2-dimensional phase encodes both in-plane and through-plane to conserve the Hadamard orthogonality introduced in mSPECS. The mSPECS-IPA encoding and reconstruction technique speeds-up the complex-valued fMRI time-series acquisition, while maintaining the integrity of separated slice images through strategic in-plane phase encoding. The mSPECS-IPA reconstruction method is demonstrated by computing the activation statistics, in a simulated complex-valued fMRI time-series and with a simulation using artificially aliased complex-valued experimental human subject fMRI data, for a net acceleration factor up to 16. This aim also serves to examine the trade-off between in-plane and through-plane net accelerations for mSPECS(-IPA), as there is an SNR penalty from in-plane subsampling not observed with through-plane only SMS acquisitions. As with mSPECS, the speed-up of the acquisition, possible with an mSPECS-IPA reconstruction, improves the statistical definition of networks in the brain and reveals subtleties within the BOLD signal.

## 1.3 Background

### 1.3.1 Signal Acquisition

The nuclear magnetic resonance signal measured with magnetic resonance (MR) techniques is a measure of the net magnetization of protons within a voxel. The main magnetic field, $B_0$, from the MR scanner is created from electric current flowing through loops of wire at superconducting temperatures. Protons will align to this strong external magnetic field with a net magnetization parallel to the main magnetic field. To produce the MR signal, the protons are perturbed from this equilibrium state with a radio frequency (RF) pulse. The RF pulse, tuned to the Larmor frequency of the proton, is transmitted to transfer energy from the RF coil to the protons. As the protons absorb the RF energy, the longitudinal net magnetization is tipped towards the transverse plane, and after the RF transmitter is turned off, the protons return to the lower energy state. The protons emit energy equal to the difference between the two energy states, this creates a sinusoidally varying voltage in the receiver coils, which is the MR signal.

The difference in magnetic susceptibilities between physiological tissues is a basic contrast mechanism in MR imaging. The longitudinal relaxation constant, $T_1$, is a measure of the exponential recovery time of the net magnetization to the parallel state, and the transverse exponential decay of signal is characterized by spin-spin interactions, $T_2$, or both spin-spin interactions and magnetic field inhomogeneties, $T_2$*. Immediately following the tipping of the net magnetic field, the net spins are in phase and over time they lose their coherence and the transverse magnetization decays, resulting in a decaying

signal. Phase coherence is required for a strong MR signal, a spin echo reverses this dephasing, so the signal produced in the receive coils is strongest when the spins are in phase. For different contrast in the slice images, e.g. $T_2$*-weighted slice images or $T_1$-weighted slice images, the echo time (TE) and time repetition (TR), or the time to repeat the experiment, are chosen based on the tissue relaxation and recovery properties at a given magnet strength. In fMRI, a longer TE, on the order of 30-40 ms for 3T, is required to measure the signal for $T_2$*-weighted slice images [Lauterbur, 1973; Bloch, 1946].

To form MR images, magnetic gradient fields spatially encode the object in the scanner by changing the local precession frequency, so each measurement in *k*-space readout is a unique orientation of the frequency and phase of the spins. The *k*-space readout is the spatial frequency coefficients of the object in the two-dimensional image space, with the center of the image defining the object, and the periphery defining the spatial resolution. The introduction of echo planar imaging (EPI) [Mansfield, 1977; Mansfield et al., 1977], offered a significant reduction in scan time, making it possible to acquire data fast enough, i.e. a TR less than 3 seconds, to model neural dynamics in fMRI studies. In EPI, an entire slice image is acquired after a single RF excitation, which is possible with spatial encoding from rapidly switching gradients traversing through *k*-space. Although, one of the largest obstacles in MRI today is still the time required to measure the *k*-space signal.

With no omission of *k*-space measurements, the *k*-space readout is sampled systematically over time. The gradients are spatially varied in the phase, frequency, and slice encoding directions to Fourier encode the object in the scanner. When an electromagnetic field in the transverse plane tips the longitudinal spins, and if a gradient

is applied in the direction of slice selection only spins that have a specific Larmor frequency will match the excitation pulse. The complex-valued MR signal measured is the sum of the signals generated by the net magnetization of the protons excited within the voxel, and the measured complex-valued signal is reconstructed to the image domain with an inverse Fourier transform (IFT) [Lauterbur, 1973, Haacke et al., 1999].

### 1.3.2 Functional MRI

Functional MRI is a valuable non-invasive tool for mapping brain activity and useful in diagnostic settings, as well as the study of cognitive dynamics in specialized patient settings. Certain patient populations, i.e. populations with degenerative neurological conditions, will exhibit decreased activation as disease progresses or before the onset of physical disease symptoms. For example, Alzheimer's patient populations have shown decreased activation when performing memory tasks compared to healthy subjects [Golby et al., 2005]. In the past decade studies published implementing or researching fMRI methods have increased exponentially, and large publically available fMRI data sets, like the human connectome project or the UK biobank, continue to make the analysis of fMRI data popular and lead to technical developments such as improved MR scanner hardware for higher quality images.

Functional MRI studies aim to identify localized neural regions associated with a cognitive task. The increased neural activity increases blood flow and the metabolic rate in the active region, leading to a decreased ratio of deoxygenated hemoglobin to oxygenated hemoglobin in the localized area. Since the deoxygenated hemoglobin has a

higher magnetic susceptibility, reducing the deoxygenated to oxygenated hemoglobin ratio contributes to less spin dephasing in the local signal. Thus active neural regions experience a prolonged $T_2$* signal, and fMRI data are generally acquired with $T_2$* based pulse sequences, i.e. gradient echo-echo planar imaging, to detect local inhomogeneities in the magnetic field. This contrast mechanism is known as the blood oxygen level dependent signal (BOLD) [Thulborn et al., 1982; Bandettini et al., 1992; Ogawa et al., 1990]. The complex-valued signal is measured over time, while the subject performs the prescribed task, generally in a block design, moderated with a stimulus. While fluctuations are observed in the BOLD signal during task performance through successively measuring image slices, the BOLD signal is an indirect measure of the hemodynamic response to neural activity. An experimental design of periodically presenting the stimulus to the subject reduces noise and increases the statistical power of the analysis of task fMRI data by matching the voxel time-series to the experimental block design, rather than a single event.

The BOLD fluctuations are measured as a complex-valued fMRI signal over time in the spatial frequency domain, then the *k*-space readout is reconstructed to the image domain with the inverse Fourier transform. Before the statistical analysis of the fMRI data, the phase portion of the data is generally discarded, despite physiologically useful information contained in the phase [Hoogenraad et al., 2001]. Previous research suggests that phase-only change arises from large draining vessels [Menon et al., 2002], or proposes methods to filter phase signal contributions from large vessels [Menon et al., 2002; Nencka et al. 2007]. Although, other models support the notion that randomly oriented vasculature yield phase change in fMRI studies [Zhao et al., 2007; Feng et al.,

2009]. Neuronal action potentials reflected in the BOLD signal may also be present in the phase [Bodurka et al., 1999, 2002; Bandettini et al., 2005; Heller et al., 2007]. Compared to the magnitude time-series, the noise in the phase time-series is prominent, and particularly susceptible to magnetic field inhomogeneities and physiological fluctuations. Before the statistical analysis of complex-valued data, dynamic modeling of the phase time-series is required to extract the biological signal of interest. It has been previously demonstrated that modeling an fMRI time-series with both magnitude and phase increases the power of the activation statistics [Rowe et al., 2004; Rowe et al., 2005a; Rowe 2005b; Rowe et al., 2009] over those from magnitude-only models.

### 1.3.3 Complex-Valued fMRI Reconstruction and Activation

To describe complex-valued image reconstruction in MRI, consider a $p_{row} \times p_{col}$ complex-valued *k*-space readout reconstructed to a single image with the discrete inverse Fourier transform (IFT). With a real-valued isomorphism representation [Rowe et al., 2007] of the Fourier reconstruction operator, $\Omega$, and the *k*-space readout in vector form, $s_t$, an image vector, $y_t$, for a single image time point, $t$, is reconstructed as

$$y_t = \Omega s_t. \qquad [1.1]$$

Equivalently, with the forward Fourier Transform

$$\Omega^{-1} = \overline{\Omega},$$

the *k*-space readout is written as

$$s_t = \overline{\Omega} y_t. \qquad [1.2]$$

In Eq. [1.1] and [1.2], the signal and image vectors are $2p\times1$, where $p=p_{row}p_{col}$ is the number of voxels, and the real parts are stacked over the imaginary parts, so $s_t = (s_R', s_I')'$ and $y_t = (y_R', y_I')'$. The real parts in each vector are organized as $s_R = (s_{R1},\ldots,s_{Rp})'$ and $y_R = (y_{R1},\ldots,y_{Rp})'$, and the imaginary parts in each vector are organized as $s_I = (s_{I1},\ldots,s_{Ip})'$ and $y_I = (y_{I1},\ldots,y_{Ip})'$. To build up the real-valued matrix framework, consider the representation of the inverse Fourier reconstruction operator, where $\Omega_R$ and $\Omega_I$ denote the real and imaginary parts of the IFT, respectively,

$$\Omega = \begin{bmatrix} \Omega_R & -\Omega_I \\ \Omega_I & \Omega_R \end{bmatrix}$$

where $\Omega_R$ and $\Omega_I$ are constructed with the Kronecker product,

$\Omega_R = [(\Omega_{yR} \otimes \Omega_{xR}) - (\Omega_{yI} \otimes \Omega_{xI})]$

$\Omega_I = [(\Omega_{yR} \otimes \Omega_{xI}) + (\Omega_{yI} \otimes \Omega_{xR})]$.

The $jk^{\text{th}}$ element of the $p_{col}\times p_{col}$ Fourier matrix $\Omega_x$ is

$$(\Omega_x)_{jk} = w^{(-\frac{pcol}{2}+j)(-\frac{pcol}{2}+k)}$$

where $j$ and $k$ have indexing values from 0 to $p_{col}$-1 with

$w = \frac{1}{N} e^{i2\pi/p_{col}}$ for the IFT and $w = e^{-i2\pi/p_{col}}$ for the forward Fourier transform (FT), [Rowe et al., 2007]. In Fig. 1.1, the complex-valued measured signal, or spatial frequencies, $S_R + iS_I$, is reconstructed with the real and imaginary parts of the IFT, $\Omega_{xR} + i\,\Omega_{xI}$, to the complex-valued image with real and imaginary parts, $V_R + iV_I$, which correspond to the magnitude and phase images for a single TR.

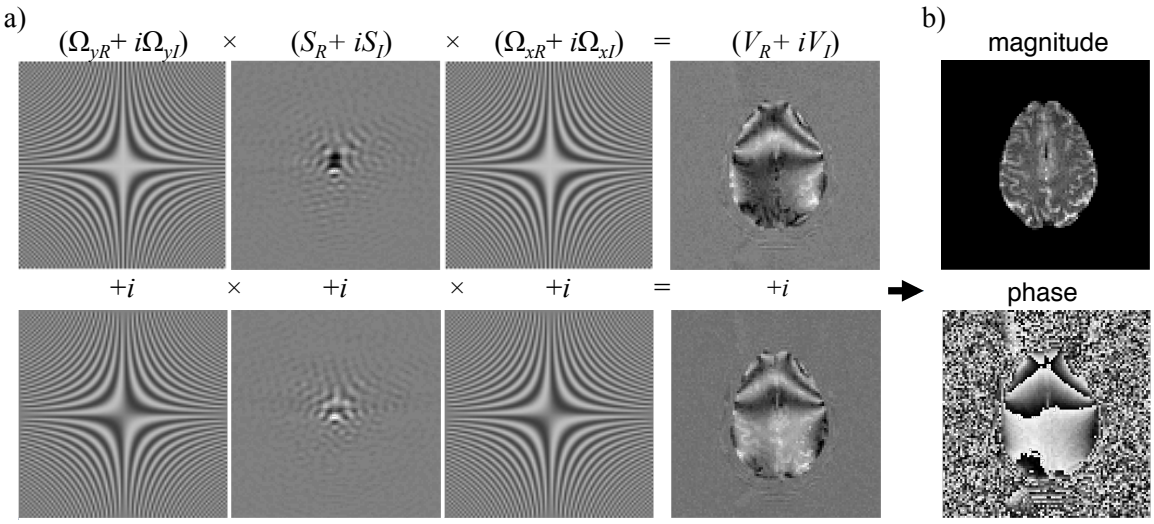


**Figure 1.1:** (a) Complex-valued image reconstruction for a single *k*-space readout, and (b) the equivalent magnitude and phase images.

At this step in the functional MR imaging pipeline, after the acquisition of the signal and image reconstruction, and before the statistical analysis of the fMRI data, the standard is to process the data to improve the signal-to-noise ration (SNR). Typical processing operations include spatial and temporal smoothing, image registration, global signal regression, motion correction. Despite the perceived gains in SNR or reduced variability in fMRI data sets achieved during processing, serious statistical implications result from commonly applied processing operations [Friston et al., 1999; Klein et al., 2009; Murphy et al., 2009; Nencka et al. 2009; Chai et al., 2012; Saad et al., 2012; Karaman et al., 2014;]. The primary effort of this dissertation is not to address the complications of signal processing in fMRI, but rather to motivate the use of the phase time-series in the analysis of fMRI data, and most notably to develop a novel image reconstruction method for fast imaging methods. Reaching the processing step in the MR

imaging pipeline with higher quality data, requires less signal processing, so processing induced correlations are avoided, thus the true signal is observed during analysis.

After image reconstruction and processing of the functional MRI data, the activation statistics are computed on the image time-series to detect the regions of activation associated with the task performed in the experiment. In this dissertation, the complex-valued activation statistics are computed on the complex-valued image time-series, as described in Rowe 2005b. A complex-valued image reconstructed from the observed complex-valued spatial frequencies observed at time-point $t$ for a single voxel, is represented in a 2×1 vector with the real and imaginary parts, $y_{Rt}$ and $y_{It}$,

$$\begin{bmatrix} y_{Rt} \\ y_{It} \end{bmatrix} = \begin{bmatrix} \rho_t \cos(\theta_t) \\ \rho_t \sin(\theta_t) \end{bmatrix} + \begin{bmatrix} \eta_{Rt} \\ \eta_{It} \end{bmatrix}. \quad [1.3]$$

Eq. [1.3] is also equivalently written in terms of polar coordinates for the observed magnitude and phase, $r_t$ and $\phi_t$, a time point $t$,

$$\begin{bmatrix} r_t \cos(\phi_t) \\ r_t \sin(\phi_t) \end{bmatrix} = \begin{bmatrix} \rho_t \cos(\theta_t) \\ \rho_t \sin(\theta_t) \end{bmatrix} + \begin{bmatrix} \eta_{Rt} \\ \eta_{It} \end{bmatrix}. \quad [1.4]$$

This complex-valued model includes both the temporally varying magnitude, $\rho_t$, and phase, $\theta_t$, at time-point $t$, with the real and imaginary error, $\eta_{Rt}$ and $\eta_{It}$. For a time-series of length $n$, the complex-valued model is more generally written,

$$y = \begin{bmatrix} A_1 & 0 \\ 0 & A_2 \end{bmatrix} \begin{bmatrix} X & 0 \\ 0 & X \end{bmatrix} \begin{bmatrix} \beta \\ \beta \end{bmatrix} + \eta, \quad [1.5]$$

where $y$ is a $2n$×1 vector, with real parts stacked over the imaginary parts. The design matrix $X$, is of dimension $n$×($q$+1), where $q$ is the number of non-baseline regressors. The $n$×$n$ matrices $A_1$ and $A_2$ contain the $n$×1 vectors, cos($\theta$) and sin($\theta$), along the diagonals, respectively. In the fMRI analysis in this dissertation $q$=1, so only the baseline signal and

the block design task are considered in the model. In Eq. [1.5], both magnitude and phase are written at time-point *t,* for *q* regressors as,

$\rho_t = \beta_0 + \beta_1 x_{1t} + \ldots + \beta_q x_{qt}$,

$\theta_t = \gamma_0 + \gamma_1 x_{1t} + \ldots + \gamma_q x_{qt}$.

The $2n\times1$ error vector, $\eta$, with the real parts stacked over the imaginary parts, is distributed as $\eta \sim N(0,\sigma^2 I_2 \otimes I_n)$. Functional activation in a voxel is detected by testing the null hypothesis of $H_0: C\beta=0,\ D\gamma=0$ (no activation in the voxel magnitude and phase time-courses), against the alternative hypothesis of $H_1: C\beta\neq0,\ D\gamma\neq0$ (activation in the voxel magnitude and phase time-courses). For $q=1$, the full row rank hypothesis constraint matrices for the magnitude and phase, *C* and *D,* are set equal to (0,1) to test if the coefficient in the reference functions is 0.

The maximum likelihood estimates (MLEs) of the parameters- magnitude, phase, and variance- are estimated under each of the hypotheses. For the alternative hypothesis, $H_1: C\beta\neq0,\ D\gamma\neq0$, of unrestricted magnitude and phase, the MLEs for the magnitude, $\breve{\beta}$, phase, $\breve{\gamma}$, and variance, $\breve{\sigma}^2$, are derived as,

$$\breve{\beta} = (X'X)^{-1}X'\breve{r},$$

$$\breve{\gamma} = (\breve{Z}'\breve{Z})^{-1}\breve{Z}'\breve{\phi},$$

$$\breve{\sigma}^2 = \frac{1}{2n}[(r - X\breve{\beta})'\left(r - X\breve{\beta}\right) + 2(r - \breve{r})'\, X\breve{\beta}].$$

Where $\breve{r}$ is the $n\times1$ vector, with time-point *t* corresponding to the $t^{th}$ element in the vector is represented as

$$\breve{r}_t = r_t\cos(\phi_t - x_t'\breve{\phi}),$$

$\breve{Z}$ is the $n\times(q+1)$ matrix with the $t^{th}$ row written as

$$\breve{z}_t = x_t' \sqrt{r_t x_t' \breve{\beta}}$$

and $\breve{\phi}$ is the $n\times1$ vector with time-point $t$ corresponding to the $t^{th}$ element in the vector is represented as

$$\breve{\phi}_t = \phi_t \sqrt{r_t x_t' \breve{\beta}}$$

and the observed magnitude and phase, $r_t$ and $\phi_t$, at time-point $t$ are as described in Eq. [1.4].

As for the linearly restricted magnitude and phase hypothesis, or the null hypothesis, $H_0$:$C\beta$=0, $D\gamma$=0, the MLEs are estimated with the magnitude and phase Lagrange restrictions, $\psi'(C\beta - 0)$ and $\delta'(D\gamma - 0)$, and the magnitude, $\tilde{\beta}$, phase, $\tilde{\gamma}$, and variance, $\tilde{\sigma}^2$, are derived as,

$$\tilde{\beta} = \psi(X'X)^{-1}X'\tilde{r},$$

$$\tilde{\gamma} = \Lambda(\tilde{Z}'\tilde{Z})^{-1}\tilde{Z}'\tilde{\phi},$$

$$\tilde{\sigma}^2 = \frac{1}{2n}[(r - X\tilde{\beta})'(r - X\tilde{\beta}) + 2(r - \tilde{r})' X\tilde{\beta}],$$

$$\psi = I_2 - (X'X)^{-1}C'[C(X'X)^{-1}C']^{-1}C,$$

$$\Lambda = I_2 - (\tilde{Z}'\tilde{Z})^{-1}D'[D(\tilde{Z}'\tilde{Z})^{-1}D']^{-1}D.$$

Where $\tilde{r}$ is the $n\times1$ vector, with time-point $t$ corresponding to the $t^{th}$ element in the vector is represented as

$$\tilde{r}_t = r_t \cos(\phi_t - x_t'\tilde{\phi}),$$

$\tilde{Z}$ is the $n\times(q+1)$ matrix with the $t^{th}$ row written as

$$\tilde{z}_t = x_t' \sqrt{r_t x_t' \tilde{\beta}},$$

and $\tilde{\phi}$ is the $n\times1$ vector with time-point $t$ corresponding to the $t^{th}$ element in the vector is represented as

$$\tilde{\phi}_t = \phi_t\sqrt{r_t x_t'\tilde{\beta}}$$

and the observed magnitude and phase, $r_t$ and $\phi_t$, at time-point $t$ are as described in Eq. [1.4].

With the MLEs for both hypotheses derived, the generalized likelihood statistics for the complex valued activation model, $-2\log\lambda_C$, is derived as

$$-2\log\lambda_C = 2n\log\left(\frac{\tilde{\sigma}^2}{\breve{\sigma}^2}\right),$$

with the variance for the null hypothesis in the numerator, and the variance for the alternative in the denominator. For large sample sizes and a constraint difference between the null hypothesis and alternative hypothesis of 1, the signed likelihood ratio,

$$Z_C = sign(C\breve{\beta})\sqrt{-2\log\lambda_C},$$

is approximated to the standard normal distribution [Rowe and Logan, 2004; Severini, 2001]. Even with evidence of task-related change in the phase time-series and the increased power of the activation statistics with the inclusion of the phase, the standard in the MR imaging pipeline is to discard the phase portion of the data after image reconstruction. In the first chapter of this dissertation, the utility of correlation between complex-valued time-series in fMRI analysis, is demonstrated in low CNR voxels.

### 1.3.4 Parallel MRI

The remaining parts of this introduction chapter return to the acquisition and reconstruction of the fMRI time-series. Temporal resolution in fMRI is important to distinguish neural events through time, and spatial resolution is important to correctly identify brain regions of interest. Although, achieving both satisfactory spatial and temporal resolution is difficult. Increasing the dimensions of the *k*-space readout for each slice acquisition increases the spatial resolution of the reconstructed images, yet reduces the temporal resolution by extending the time for successive acquisition of slice images. Decreasing the *k*-space readout measurements for each slice image acquisition reduces the time for successive acquisition, so spatial resolution is reduced with increased temporal resolution. Parallel imaging, or in-plane acceleration, methods achieve a speed-up of acquisition through subsampling the *k*-space readout at multichannel receive coils, by reducing the number of phase encodes. The spatial information from the multichannel receive coil sensitivities is incorporated in the image reconstruction to recover spatial information. The two standard pMRI reconstruction methods for in-plane accelerated imaging are SENSitivity Encoding (SENSE) [Pruessman et. al, 1999] and Generalized Autocalibrating Partially Parallel Acquisition (GRAPPA) [Griswold et. al, 2002]. Accelerated in-plane imaging methods do not increase the rate at of *k*-space measurements, but omit the number of measurements for a single *k*-space readout, allowing a speed-up of acquisition time without requiring faster switching gradients. SENSE is an image space reconstruction method, where the in-plane aliased are reconstructed before the signal is and disentangled, and GRAPPA is a *k*-space

reconstruction method, where the *k*-space readout is interpolated before image reconstruction, the mSPECS and mSPECS-IPA reconstruction methods presented in this dissertation are image space models, so the SENSE reconstruction algorithm will be focused upon.

Multichannel receive coils are advantageous in MRI since combining multiple coil images improves the image SNR, through increasing the number of averages for the slice image. As the number of receive coils is increased the sensitivity at each coil is reduced because the coils are smaller, thus there is an optimal SNR and noise trade-off regarding the number of coils used in MR imaging studies. For fully sampled *k*-space readouts, the default procedure to combine coil images with the root mean square of the coil images for each slice. In the context of reconstruction of subsampled the *k*-space readout with multichannel receive coils, optimal coil geometry and distinct coil sensitivity profiles among the aliased voxels, leads to improved slice images during the voxel separation. The SENSE reconstruction algorithm is also implemented with fully sampled *k*-space. The geometry factor or *g*-factor is a coil dependent noise amplification factor that is derived from a ratio of SNR with no acceleration to an SNR with acceleration for each slice. The *g*-factor increases as the acceleration factor increases and varies spatially, and also describes how well aliased voxels are separated based on a given coil configuration.

In second and third aims of this dissertation, the complex-valued receive coil sensitivity profiles are estimated by taking the image mean in the time dimension at each coil. An example of mean magnitude unprocessed images is show in Fig. 1.2a for 32-channel receive coils. The mean coil images are normalized and the anatomical structure

is removed, by averaging the mean coil images to a single image. To refine the raw coil sensitivity profiles, a low order, i.e. on the order of 2 or 3, polynomial is fit to a local plane for each voxel, as shown in Fig. 1.2b, this is a standard image processing procedure.

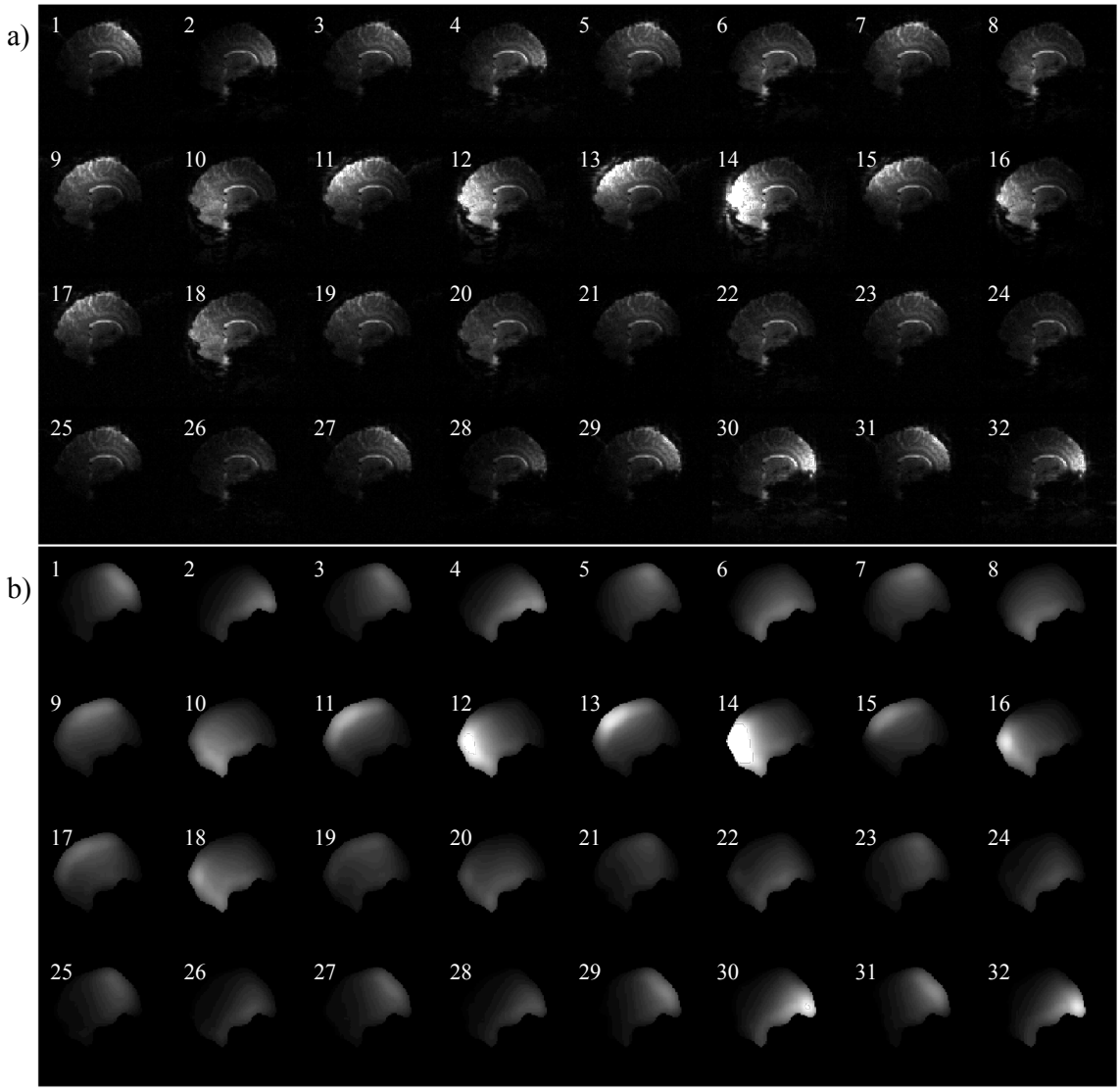


**Figure 1.2:** Experimental example of (a) magnitude mean coil slice images, and the (b) the corresponding estimated receive coil sensitivity maps.

To accelerate the acquisition, the number of phase encodes in the *k*-space readout are decreased in a systematic approach. Switching one encoding gradient consistently in the same direction is less demanding on the gradients than alternating the switching in two directions, both phase encoding (PE) and frequency encoding (FE), and thus less time consuming during the *k*-space readout. A fully sampled *k*-space readout corresponds to an acceleration factor of $R$=1, as seen in Fig. 1.a where $R$=2, increasing the acceleration factor corresponds in a distance between acquired lines of $R\Delta k_y$. In fMRI, in-plane parallel imaging methods are often implemented with an acceleration of only 2 to 3.

The center of the *k*-space readout is included in the signal readout, as it defines the general distribution of the object in image space, and skipping lines of the *k*-space readout results in wrap around aliasing artifacts of the reconstructed slice images due to failure to meet the Shannon-Nyquist sampling criteria. Fig. 1.3b is an illustration of the magnitude reconstructed images from subsampled the *k*-space readout for $R$=2, at 4 receiver coils located at the four edges of the slice image, where the image at each acceleration has $R$ voxels aliased. As illustrated in Fig. 1.3c, the spatial information derived from receiver coil sensitivity profiles are required to compensate for the missing phase encoding lines in the subsampled arrays.

With SENSE aliased images are reconstructed from a subsampled *k*-space readout of acceleration $R$. Consider a single $(x,y)$ voxel location, for $n_C$ receiver coils the complex-valued coil sensitivities at the $j^{th}$ coil measuring the voxel is represented as $S_j = [S_R, -S_I; S_I, S_R]_j$.

The complex-valued $R$ aliased voxels in the aliased images are described with a $2n_C \times 1$ real-valued vector $a$, with real and imaginary parts measured at $n_C$ coils

$$a = Sv + \varepsilon. \quad [1.6]$$

This subsampling creates an inverse imaging problem with an over determined system of equations. In Eq. [1.6], $S$ is an $2n_C \times 2R$ matrix with the fully sampled complex-valued coil sensitivities, illustrated in Fig. 1.3a, for the $R$ aliased voxels in the $n_C$ coils, $v$ is a $2R \times 1$ vector of the real and imaginary parts of the $R$ aliased true voxel values, and $\varepsilon$ is a $2n_C \times 1$ vector of the $n_C$ complex-valued additive measurement noise in each aliased voxel.

The aliased slice images, reconstructed from the subsampled $k$-space readout acquired at each coil, are un-aliased through a least squares estimation with the fully sampled coil sensitivity maps. Thus, the images are measured as illustrated with Fig. 1.3b for a single TR, then using the spatial information of the complex-valued coil sensitivity profiles shown in Fig. 1.3a the images are reconstructed as in Fig. 1.3c. In SENSE reconstruction, the SNR is not uniform throughout the reconstructed slice image, in-plane acceleration methods have an SNR penalty equal to the square root of the acceleration, $R$. Aliased voxel separation with SENSE reconstruction has also been shown to induce a systematic spatial correlation across previously aliased voxels [Bruce et al., 2011]. The residual aliasing artifacts resulting from in-plane pMRI methods, present differently than from the through-plane SMS methods. Intra-slice leakage with pMRI methods is readily identifiable, as it will appear as ghosting artifacts in the unwrapped image. With through-plane accelerations, the source of inter-slice signal leakage is difficult to identify, as the artifacts lack the continuity observed with the in-plane accelerations.

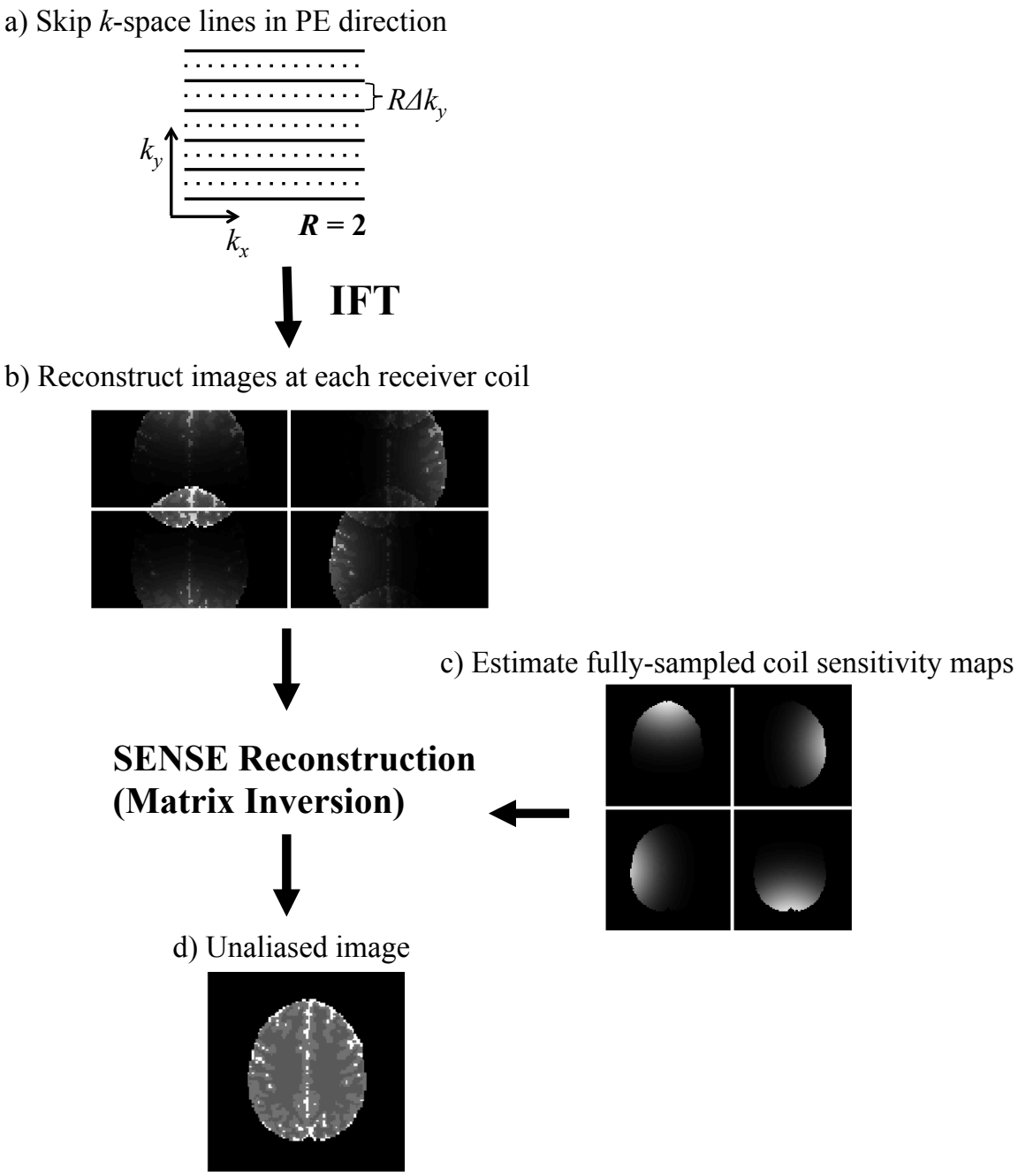


**Figure 1.3:** Schematic of SENSE reconstruction for an acceleration factor of 2, (a) *k*-space readout subsampled with $R = 2$, with the sampled lines marked with a straight line and the dotted lines are the skipped lines in the *k*-space readout, (b) the subsampled *k*-space readout is reconstructed to aliased images, (c) receiver coil sensitivity maps estimated from fully sampled data, (d) the aliased images and sensitivity maps are combined with the SENSE matrix inversion to reconstruct the aliased image.

### 1.3.5 Simultaneous Multi-Slice

Echo planar imaging methods are commonly used to measure BOLD contrast in fMRI studies, where each slice image is individually magnetized from a RF pulse and reconstructed from a single complex-valued *k*-space readout. In-plane acceleration methods achieve an acceleration factor of 2 or 3, with an SNR penalty relative to the number of skipped rows. Shortening the length of the echo train, or the number of echoes required for the phase encoding lines within a TR, by omitting *k*-space measurements reduces image distortions from magnetic field inhomogeneities, since long echo trains are susceptible to geometric distortions from $T_2$* relaxation. Reducing the TE also decreases the specific absorption rate (SAR), or RF heating, by reducing the number of RF pulses required for the acquisition. Although in fMRI, temporal resolution is constrained by the long TE required to maintain the BOLD contrast in the reconstructed slice images, yet a short enough TR is desirable to model neural dynamics with full brain coverage. SMS-fMRI imaging techniques overcome this limitation by simultaneously exciting multiple slice images, while maintaining a long enough TE for BOLD contrast, to achieve higher acceleration rates than in-plane acceleration methods alone. SMS is a rapidly advancing imaging technique which substantially speeds up scan time compared to traditional in-plane methods, with a marginal SNR loss in the reconstructed slice images. There is some signal loss associated with SMS methods, from a reduction of the excitation with the Ernst angle to avoid complications with SAR, and the magnetization is not fully recovered from one excitation to the next.

Omission of measurements of the spatial frequency coefficients or the simultaneous magnetization of multiple slice images allows for a higher sampling rate of time points in a given time period. This is an important development for fMRI analysis in high-resolution whole brain acquisitions. Similar to increasing the number of averages with multiple measurements via multi-channel receive coils, increasing the number of time points decreases the noise variability within the BOLD measurements. A higher image sampling rate also reveals more subtleties within neural networks for a better statistical definition of the neural networks. Often the primary focus in fast imaging methods is to increase image speed at the expense of accuracy of the acquisition and reconstruction methods. Data quality is compromised when suboptimal reconstruction methods are implemented. This induces aliasing artifacts in the separated slice images where it may be difficult to identify the origin of artifacts, or the improper placement of the BOLD signal, where false activation is detected in regions previously aliased with the functional region of interest. Poorly designed reconstruction methods may also result in temporal autocorrelation is the separated slice image time-series.

Multiple slices in the image domain are simultaneously excited with multi-frequency band RF pulses, or composite RF pulsed, during acquisition. In single-band imaging a single slice image is reconstructed from a single *k*-space readout; in multi-band imaging a single image, of superimposed slice images, is reconstructed from a single *k*-space readout. The aliased slice locations are selected through altering the RF pulse with the Fourier shift theorem, such that the desired offset of the slice images is observed in the image domain. Before the introduction of multi-channel phased receive coil arrays in MR scanners, early method for simultaneously magnetizing multiple slice images

implemented phase encoding techniques in the pulse sequence to disentangle the slice images.

In Hadamard encoded slice image acquisitions, the simultaneously excited slice images are individually labeled with multi-frequency band slice selection RF pulses, where the RF pulse modulates the phase encoding in a Hadamard pattern. So the complex-valued reconstructed Hadamard encoded slice images are resolved through solving a system of linear equations after the aliased images are reconstructed. The $n_S$ Hadamard encoded aliased slice image time repetition patterns are illustrated in Fig. 1.4, for an example of $n_S$=4 aliased slice images for the $\delta$=$n_S$ aliasing patterns. Fig. 1.4a is the aliased reconstructed image, which is a sum or a difference of the slice images represented in Fig. 1.4b. In this dissertation, the aliased image time-series, for the mSPECS(-IPA) reconstruction, is acquired with a Hadamard multi-frequency band pulse sequence, with the Hadamard encoding matrices constructed with the Sylvester method [Sylvester, 1867],

$$H_1 = [1]$$

for a two slice image aliasing scheme, where the $z^{\text{th}}$ column refers to the $z^{\text{th}}$ slice image and the $\delta^{\text{th}}$ row refers the $\delta^{\text{th}}$ aliasing pattern,

$$H_2 = \begin{bmatrix} 1 & 1 \\ 1 & -1 \end{bmatrix},$$

this is generalized to include the number of aliased slice images, $n_S$, in powers of 2

$$H_{2^k} = \begin{bmatrix} H_{2^{k-1}} & H_{2^{k-1}} \\ H_{2^{k-1}} & -H_{2^{k-1}} \end{bmatrix} \qquad [1.7]$$

where $k \geq 2$, and $H_{2^k}$ is of dimension $2^k \times 2^k$.

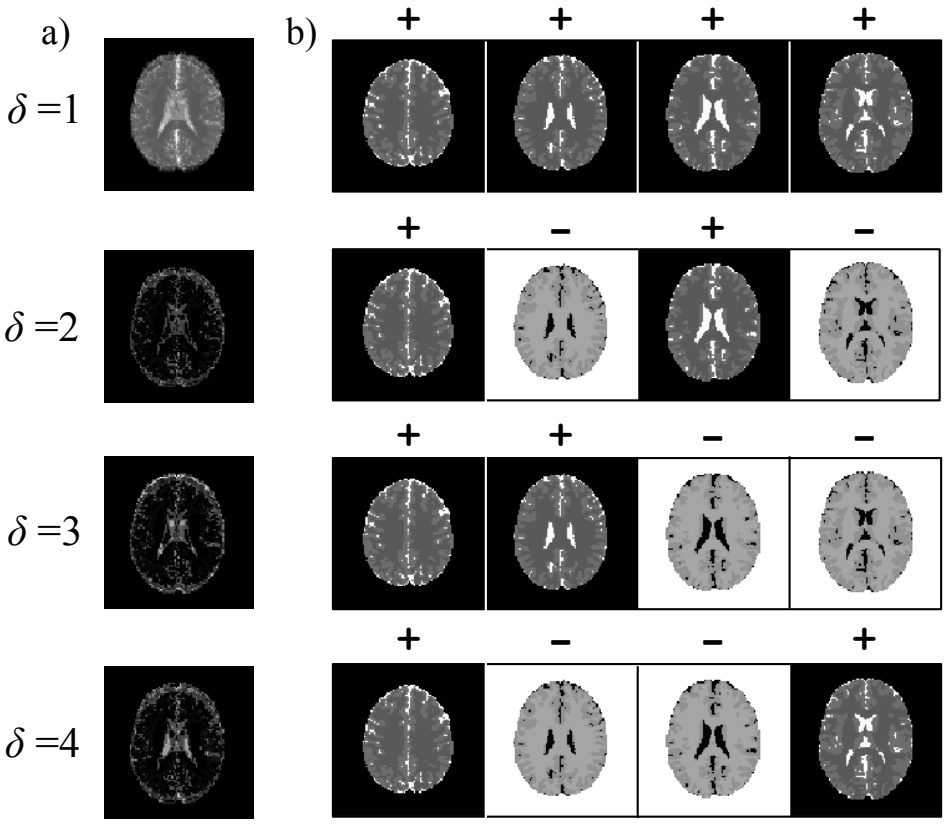


**Figure 1.4:** (a) The $n_S$=4 complex-valued aliased slice images acquired over 4 consecutive time repetitions, corresponding to the $\delta^{th}$ aliasing patterns, are the sum and difference of the (b) the individual complex-valued slice images.

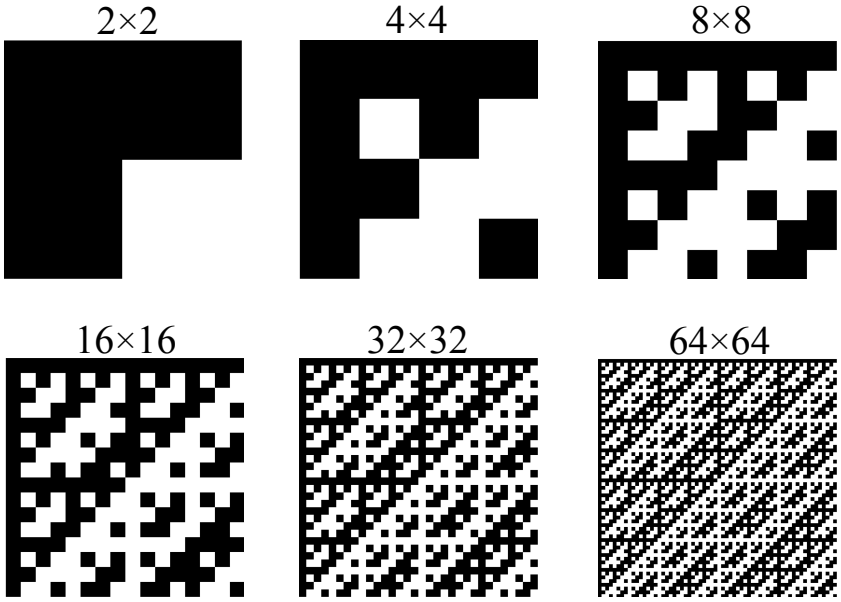


**Figure 1.5:** Hadamard matrices increase in powers of two with mutually orthogonal rows and columns. The black boxes denote +1, and the white boxes denote -1.

In standard Hadamard separation schemes, the superimposed slice images are separated from measurements over the length of TRs equivalent to the number of simultaneously excited slice images. So, if two slice images are simultaneously measured over two time repetitions with a Hadamard pattern of order 2, the two sequential time repetitions are summed to resolve the first slice image, and subtracted to resolve the second slice image. The slice image separation, by solving a system of linear equations, results in an increased SNR compared to standard single-band EPI, although there is no net reduction in scan time. The addition and subtraction schemes are also more susceptible to signal loss from motion or other instabilities during acquisition than standard single-band EPI [Mueller et al., 1988; Souza et al., 1988]. Phase Offset Multi-Planar (POMP) [Glover, 1991], is another early SMS phase encoding technique, where only the phase of one slice image is partially manipulated in a two slice image excitation experiment. With the field-of-view (FOV) increased, the reconstructed image consists of the two simultaneously magnetized slice images, where one slice image is shifted by half a FOV, from the phase manipulation, so there is no overlap between the two slice images.

With the advent of multi-channel phased receive coil arrays, coil encoding methods are introduced as another means to speed-up acquisition in the context of SMS methods. A multi-slice version of in-plane SENSE implements the complex-valued receiver coil sensitivity profiles to disentangle the aliased voxels across multiple slice images at once. The technique requires the number of slice images aliased to be less than or equal to the number of receiver coils, and separates the aliased voxels with a matrix inverse approach using in-plane SENSE methodology with additional equations [Larkman et al., 2001]. Although, for whole volume brain acquisitions, the small

distances between the aliased slice images presents an ill-conditioned unaliasing problem and *g*-factor noise amplification in the reconstructed images. A standard practice in SMS acquisitions is to interleave slice images during acquisition, with an odd number of total packets to prevent signal saturation [Setsompop et al., 2012].

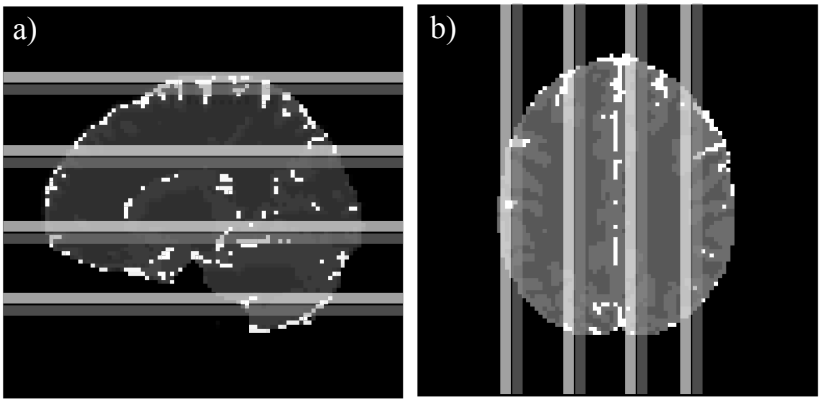


**Figure 1.6:** Diagram of interleaved slice images for two packets, packet 1 is denoted by the white lines and packet 2 is denoted by the grey lines of (a) 4 axial slice images in each packet, and (b) 4 sagittal slice images in each packet.

An example of slice interleaving for whole volume acquisitions is shown for the first two packets consisting of four simultaneously excited slice images, where the slice images in packet one are denoted by the white lines and the slice images in packet two are denoted by the grey lines, containing four aliased slices in Fig. 1.6. Other studies investigating full volume acquisition employed SMS imaging methods with a 3-dimensional Fourier transform (3DFT) and coil encoding imaging techniques [Weiger et al., 2002; Breuer et al., 2006], although preference is given to an SMS approach for fMRI studies.

In the past five years, SMS acquisition and reconstruction methods have quickly evolved. One of the most significant advancements in the field of SMS imaging is the development of Controlled Aliasing in Parallel Images Results in Higher Acceleration (CAIPIRINHA). CAIPIRINHA is an SMS multi-frequency EPI method where the phase in the slice images is partially modulated [Breuer et al., 2005; Nunes et al., 2006]. Similar to POMP, the phase is partially manipulated in the simultaneously magnetized slice images, although the reconstructed images acquired with a CAIPIRINHA sequence have superimposed slices, and coil encoding methods provide additional spatial information to separate the aliased slice images. The phase manipulation of the spatial frequency coefficients during acquisition corresponds to shifts in the FOV in the image domain. The CAIPIRINHA shifts present a solution for the ill-conditioned unaliasing problem, by increasing distances in the aliased voxel values and the related coil sensitivity profiles, as well as utilizing the full FOV, thus reducing the number of aliased voxels in the aliased image.

To achieve high acceleration factors and successfully disentangle aliased slice images, multiple encoding methods, i.e. phase and coil encoding, are required during multi-frequency band acquisitions. Although, images significantly degrade for accelerations higher than 8 [Chen et al., 2015], and fMRI inter-slice signal leakage is introduced in acquisitions with multi-frequency band factors greater than 4, [Todd et al., 2015]. Inter-slice signal leakage or residual aliasing artifacts, arise from the correlation between previously aliased slices, where substandard encoding methods result in improper placement on the mean signal in the separated slice images. In addition to strategic experimental design with encoding patterns during image acquisition, the slice

image separation reconstruction methods also play a critical role in the quality of the separation of aliased slice images, since the accuracy of the slice image separation is a function of both acquisition and reconstruction. Efforts have been made to characterize and mitigate the inter-slice leakage arising from suboptimal reconstruction methods [Cauley et al., 2014; Moeller et al., 2012; Xu et al., 2013]. However, a more recent study has shown that the reconstruction methods, in a comparison of commonly applied SMS *k*-space slice separation methods, introduce inter-slice leakage of the BOLD signal in SMS-fMRI reconstructed time-series [Todd et al., 2015]. The last two chapters of this dissertation address the need for novel statistical methods for the reconstruction of multi-frequency band acquisitions in fMRI.

# Chapter 2: A Fourier Description of Covariance

## 2.1 Introduction

This chapter outlines a method to describe correlation between two time-series with both magnitude and phase, equivalently real and imaginary parts, through exploiting the linear relationship between the image domain and spatial frequency domain. Traditionally both magnitude-only and complex-valued models require time-series with the time-points, however, complex-valued time-series correlation analysis with temporal frequency coefficients is also possible. It has previously been shown how complex-valued temporal frequency coefficients contribute to the correlations between voxels in the cerebral cortex for magnitude-only non-task data [Cordes et al., 2001]. Similarly, in this manuscript the spatial correlation between complex-valued time series is described as a linear combination of second order voxel temporal frequency coefficients. The chapter advances the frequency correlation description into a linear matrix framework with an application to a complex-valued simulation demonstrating the strength of the framework at varying degrees of magnitude and phase CNR values, as well demonstrating its utility in experimental complex-valued human subject fMRI data through examining correlations for voxel time-courses with high and low CNRs.

While measuring the *k*-space readout, unwanted image acquisition artifacts and physiological noise obscure the true underlying signal of interest. To improve the SNR, various preprocessing operations, i.e. temporal frequency filtering or magnitude image smoothing, are incorporated in the processing and reconstruction pipeline, and

physiologic noise sources are commonly regressed out from the signal [Birn et al., 2006; Glover et al., 2000; Hahn et al., 2012; Hu et al., 1995]. It is well documented that the application of these operations induce local spatial and temporal correlations into neural regions that were previously uncorrelated [Friston et al., 2000; Nencka et al., 2009; Davey et al., 2013]. One application of the linear framework developed in this chapter, is to describe how signal processing alters the structure of the spatial covariance matrix, such that induced correlation is a result of increased overlapping frequency content between voxels after processing. Signal processing will alter the activated voxel's temporal frequency spectrums, by spreading voxel task activated peaks temporally and spatially. Correlation will be induced between voxels as a result of increased overlapping frequency content between the two voxels' Fourier frequency spectrums.

An experimental fMRI time-series is plotted in Fig. 2.1a with the real and imaginary parts of the voxel's time-series and the corresponding temporal frequency coefficients; Fig. 2.1b with the magnitude and phase parts of the voxel's time-series and the corresponding temporal frequency coefficients. Note, the task-related peak in Fig. 2.1, is observed in both the real and imaginary spectra, and the magnitude and phase spectra. So, if another voxel has a task-activated peak, the two voxels would be expected to share a significant correlation. This notation for spatial correlation is advantageous since various physiological signals are also confined to specific frequency ranges. Respiratory and cardiac cycle fluctuations are characterized around 0.2-0.3 Hz and 1 Hz in a voxel's temporal frequency spectrum, although they are often aliased to low frequencies in fMRI signal acquisition [Birn et al., 2006; Bhattacharyya et al., 2004; Shmueli et al., 2007]. The summation notation of spatial correlation that is described here, allows relative

contributions to the correlation to be quantified by segregating the natural partitions in a voxel's temporal frequency spectrum. Compared to magnitude-only correlations, applying this framework with complex-valued data more accurately identifies regions of spatial correlation, and reduces the false positives in correlation maps. This result is most significant in low magnitude CNR data sets since including the phase in the complex-valued correlation results in increased sensitivity of identifying correlated regions.

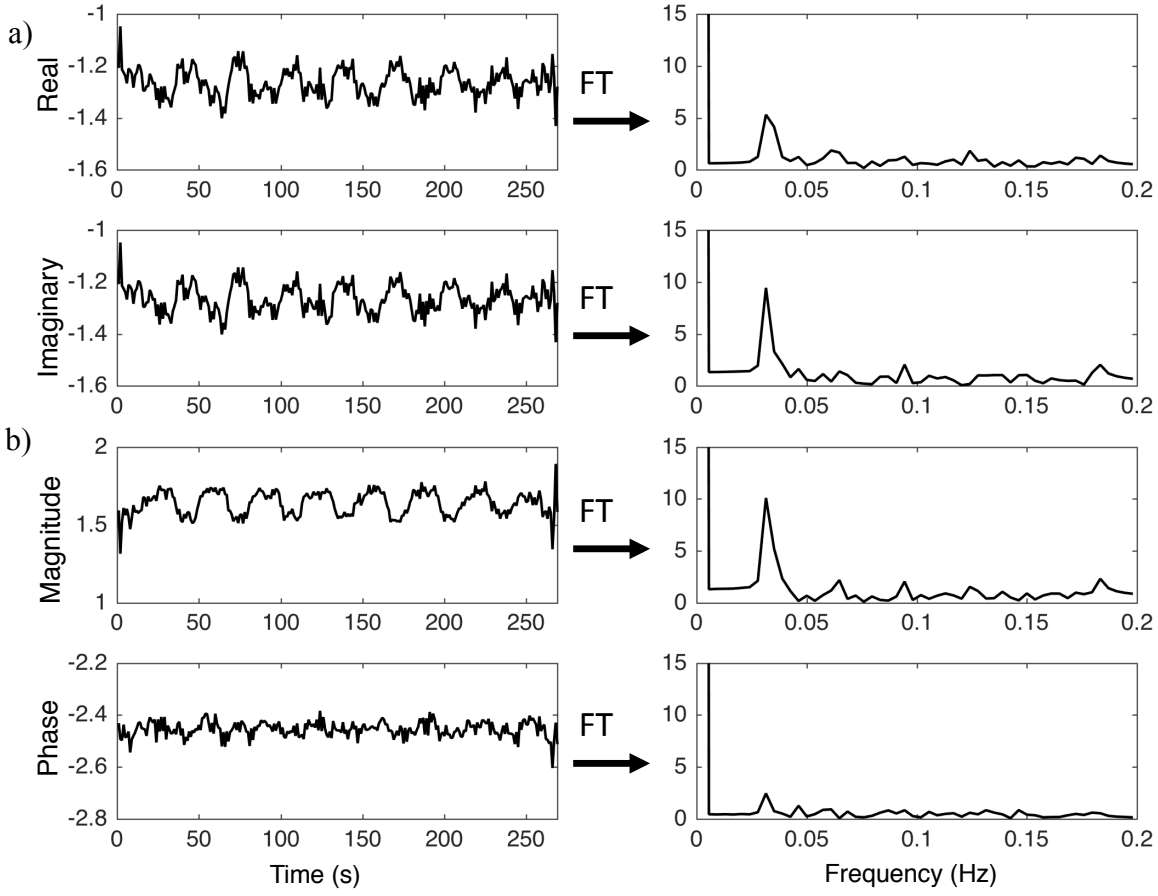


**Figure 2.1**: (a) The real and imaginary parts of an "activated" voxel time-series from an fMRI experiment, and the Fourier transform of the time-series, with the corresponding task-peak observed in both real and imaginary parts, (b) The magnitude and phase parts of a voxel an "activated" time-series from an fMRI experiment, and the Fourier transform of the time-series, or temporal frequencies, with the corresponding task-peak observed in both magnitude and phase parts.

## 2.2 Theory

To reconstruct images over $n$ TRs, the complex-valued spatial frequencies are represented in the real-valued $2pn\times1$ vector $s$, with each successive TR concatenated to the vector. An analogous explanation describes the organization of the real-valued image $2pn\times1$ vector, $v$, which is reconstructed with the Kronecker product,

$$v = (I_n\otimes\Omega)s. \quad [2.1]$$

A $2pn\times2pn$ permutation matrix, $P$, reorders the elements of vector $v$ so the real-valued time-series $2pn\times1$ vector

$$y=Pv$$

is now ordered by voxel rather than ordered by image. The voxel ordered time-series is Fourier transformed into the temporal frequency domain, with the $2n\times2n$ temporal forward Fourier transform (FT) matrix, $\overline{\Omega}_T$, as opposed to the $2p\times2p$ spatial Fourier operations. The real-valued $2pn\times1$ vector $f$ consists of the temporal frequencies of each voxel stacked upon the corresponding imaginary temporal frequencies is represented,

$$f = (I_p\otimes\overline{\Omega}_T)v. \quad [2.2]$$

For voxel $\omega$, the $2n\times1$ real-valued voxel time-series is denoted $y_\alpha$, with real parts stacked over imaginary parts $y_\omega=(y_{\omega R}',y_{\omega I}')'$ so the real and imaginary parts in each vector are organized as $y_{\omega R}=(y_{\omega R1},\ldots,y_{\omega Rn})'$ and $y_{\omega I}=(y_{\omega I1},\ldots,y_{\omega In})'$, with a mean and covariance structure of $\mu_{R\omega}$ and $\mu_{I\omega.}$, $\sigma^2_{R\omega}\mathrm{I}_n$ and $\sigma^2_{I\omega}\mathrm{I}_n$. The corresponding temporal frequencies for voxel $\alpha$ are denoted in the $2n\times1$ vector $f_\omega$, where

$$y_\omega = \Omega_T f_\omega$$

and

$f_\omega = \overline{\Omega}_T y_\omega,$

are organized similarly to the time-series equivalent. With an analogous description of another voxel $\vartheta$, the spatial covariance between the two voxels is simply written,

$\text{cov}(y_\omega, y_\vartheta) = (y_\omega - \mu_\omega)' (y_\vartheta - \mu_\vartheta)/(2n).$

Assuming the time-series is demeaned, then the covariance between two voxels in terms of temporal frequencies is represented as,

$$\text{cov}(y_\omega, y_\vartheta) = (y_\omega' y_\vartheta)/(2n) = (\overline{\Omega}_T f_\omega)' (\overline{\Omega}_T f_\vartheta) = (f_\omega' f_\vartheta)/4 \quad [2.3]$$

The spatial covariance in Eq. [2.3] is expanded to a $p \times p$ spatial covariance matrix, $\Sigma$, such that the entry $(\omega, \vartheta)$ in $\Sigma$ represents the spatial covariance between the two demeaned real-valued voxel time-series of voxel $\omega$ and voxel $\vartheta$. By defining $D$ as the diagonal matrix consisting of the diagonal elements of $\Sigma$, a $p \times p$ spatial correlation matrix is written as,

$$R = D^{-1/2} \Sigma D^{-1/2}. \quad [2.4]$$

By aggregating the second order temporal frequencies into biologically meaningful or experimentally relevant bands, the influence preprocessing steps have on each voxel temporal frequency spectrum can be quantitatively measured. In an fMRI study, the frequency corresponding to the activation is considered when dividing the spectrum into bands. To understand the contribution each temporal frequency band yields to spatial correlation, the correlation is expressed as, the spatial covariance matrix can be written as a summation of covariance of each band and $b$ is the total number of bands,

$$\Sigma = \Sigma_1 + \ldots + \Sigma_b, \quad [2.5]$$

and the Eq. [2.5] spatial correlation matrix can be written as a summation of correlation of bands

$$R = D^{-1/2}(\Sigma_1 + \ldots + \Sigma_b)D^{-1/2} = R_1 + \ldots + R_b. \quad [2.6]$$

The linear matrix representation of the spatial covariance and correlation, allows one to measure the effect of the temporal and spatial processing operators. Define a $p \times p$ spatial smoothing operator, $S_m$, which filters the real and imaginary components separately with a Gaussian kernel. Continuing the notation used in Eq. [2.1] with a demeaned time-series notation, the smoothed $2pn \times 1$ temporal frequency vector is constructed with the multiplication

$$y_s = (I_p \otimes \overline{\Omega}_T)P(I_{2n} \otimes S_m)v.$$

The series of operations applied to the temporal frequencies is defined with $2pn \times 2pn$ operator,

$$O = (I_{2n} \otimes S_m)P(I_p \otimes \overline{\Omega}_T)$$

such that the $2pn \times 1$ unprocessed and processed time-series vectors ordered by voxel are represented as in Eqn. [2.3],

$$v = (I_p \otimes \overline{\Omega}_T)y \text{ and } v_s = Ov .$$

The $2pn \times 2pn$ spatiotemporal covariance matrix for the $2pn \times 1$ real-valued image time-series, $v$, in terms of temporal frequency spectrum, is defined as

$$\text{cov}[v] = \Gamma, \quad [2.7]$$

and the covariance matrix with processing operators is defined

$$\text{cov}[v_s] = O\Gamma O'. \quad [2.8]$$

Eq. [2.7] and [2.8] are described in terms of temporal frequencies, where the spatial component of Eq. [2.7] is equivalent to $\Sigma$ described in Eq. [2.3], through a process of summing real and imaginary diagonal values to achieve a $p \times p$ magnitude-squared spatial correlation matrix such that the temporal component is held constant. Magnitude-squared

correlation is asymptotically equivalent to magnitude-only correlation [Birn et al, 2006; Rowe et al, 2009].

## 2.3 Methods

### 2.3.1 Simulation

To demonstrate the improved sensitivity and specificity of correlation between complex-valued time-series over correlation between magnitude time series in functional MRI studies, a MATLAB simulation is run with a varying degree of magnitude contrast-to-noise ratio ($CNR_\rho$) and the phase contrast-to-noise ratio ($CNR_\phi$). The SNR is defined as the baseline magnitude signal over the standard deviation of the noise in the time-series,

$$\text{SNR} = \frac{\rho}{\sigma} \qquad [2.9]$$

For the CNR, the amplitude is defined as the difference between the baseline signal and the task related change in the signal for the magnitude and phase components of the time-series, $A_\rho$ and $A_\phi$, so

$$\text{CNR}_\rho = \frac{A_\rho}{\sigma}, \qquad [2.10]$$

$$\text{CNR}_\phi = \frac{A_\phi}{\sigma/\rho}. \qquad [2.11]$$

Assuming normally distributed noise in the real and imaginary channels, with a large SNR, the standard deviation of a phase-only time-series is $\sigma/\rho$, and the $CNR_\phi$ is

proportional to the SNR. Typically in fMRI studies, the task related signal change in the magnitude $A_\rho$ corresponds to approximately a 1-2% signal change, and the task related change in the phase $A_\phi$ has been found to be approximately π/36 [Menon et al., 2002]. To compare magnitude-only and complex-valued correlations, two 96×96 surfaces are generated with 720 time-points and standard normal random noise added to the real and imaginary channels. As visualized in Fig. 2.2, each voxel has a $\rho$ between 0 and 50, and a task generated to represent a magnitude amplitude $A_\rho$ between 0 and 1, and a phase amplitude $A_\phi$ between 0 and π/36. The magnitude-only and complex-valued correlations are computed between the two time-series in each surface with equivalent parameter settings, so there is a 96×96 corresponding matrix for magnitude-only and complex-valued. To compare the correlations between the two models, the Fisher-$z$ transform, $z$, is computed and plotted for each time-series correlation, $r$, as

$z = \frac{1}{2} \ln\left(\frac{1+r}{1-r}\right)$.

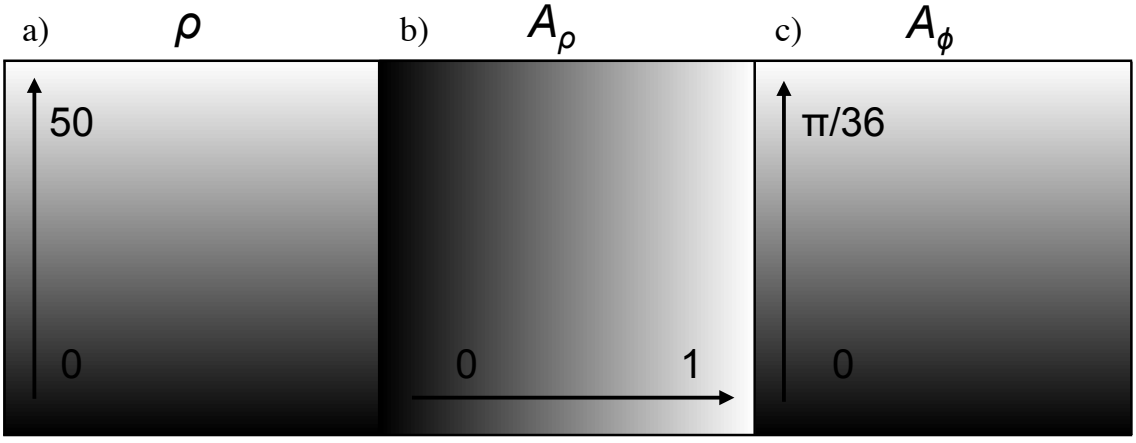


**Figure 2.2:** Surfaces representing the (a) magnitude, $\rho$, (b) $A_\rho$, and (c) $A_\phi$ parameters used to generate the simulated time-series.

### 2.3.1 Human Subject Data

An experimental fMRI human data set was acquired with bilateral finger tapping in a block design with an initial 16 s rest followed by 22 epochs of 16 s of task and 16 s of no task using a 3.0 T Discovery MR750 MRI scanner (General Electric, Milwaukee, WI) with a GE single channel quadrature head coil. The data was acquired with ten interleaved axial slices that are 96×96 in dimension and 4 mm thick. A superior slice with activation was chosen for analysis. The imaging parameters included a 24.0 cm FOV, a TR/TE of 1000/39 ms, a flip angle of 25°, an acquisition bandwidth of 111 kHz, and an effective echo spacing of 0.672 ms. The phase encoding direction was oriented as posterior to anterior (bottom to top in images). Images were Nyquist ghost corrected using the three navigator echoes method [Nencka et al., 2009] and dynamic $B_0$ field corrected using the TOAST single echo technique [Hahn et al., 2009].

To demonstrate the utility of the framework, voxel temporal spectrums are analyzed after applying a spatial smoothing operator with a Gaussian kernel with a full-width-half-max (FWHM) of 3 voxels, followed by an ideal high-pass band filter (<0.009 Hz) and an ideal low-pass band filter (>0.08 Hz). The spatial correlation is decomposed into three correlation bands, $R_1$, $R_2$, $R_3$, such that sum of the bands equals the total correlation. The complex-valued correlation bands that are selected correspond to the frequency band ranges 0.0009 - 0.024 Hz, 0.026 - 0.037 Hz, 0.038 - 0.08 Hz, with the task-activated frequency peak is observed in $R_2$. The complex activation for the data was computed as described in the first chapter of this dissertation [Rowe 2005b], and four

voxels were chosen based on their complex-valued activation locations: two in the motor cortex and two in the supplementary motor cortex.

The two voxels in each location are chosen so that one voxel has a high $\text{CNR}_{\rho}$ and $\text{CNR}_{\phi}$, and the other has a low $\text{CNR}_{\rho}$ and $\text{CNR}_{\phi}$. As shown in Fig. 2.3, the locations are chosen from the SNR, $\text{CNR}_{\rho}$, and $\text{CNR}_{\phi}$ maps for the experimental human subject data. These values for each voxel time-series are computed with the unrestricted MLEs, from the complex-valued model described in the introductory chapter, presented in Eq. [1.5], for the magnitude $\breve{\beta}$, phase, $\breve{\varphi}$, and variance, $\breve{\sigma}^2$ parameters. Aside from the baseline signal, or intercept, the only regressor, $\beta_1$, corresponds to the on and off periods in the time-series for the bilateral finger tapping task. In this complex-valued model the magnitude and phase for a single time-point $t$ is described or modeled as,

$\rho_t = \beta_0 + \beta_1 x_{1t}$,

$\phi_t = \varphi_0 + \varphi_1 x_{1t}$ .

The SNR, $\text{CNR}_{\rho}$, and $\text{CNR}_{\phi}$, written in Eq. [2.9], Eq. [2.10], and Eq. [2.11], is analogously defined for the complex-valued experimental human subject data, with the unrestricted MLEs,

$$\text{SNR} = \frac{\breve{\beta}_0}{\breve{\sigma}}$$

$$\text{CNR}_{\rho} = \frac{\breve{\beta}_1}{\breve{\sigma}},$$

$$\text{CNR}_{\phi} = \frac{\breve{\varphi}_1}{\breve{\sigma} \big/ \breve{\beta}_0}.$$

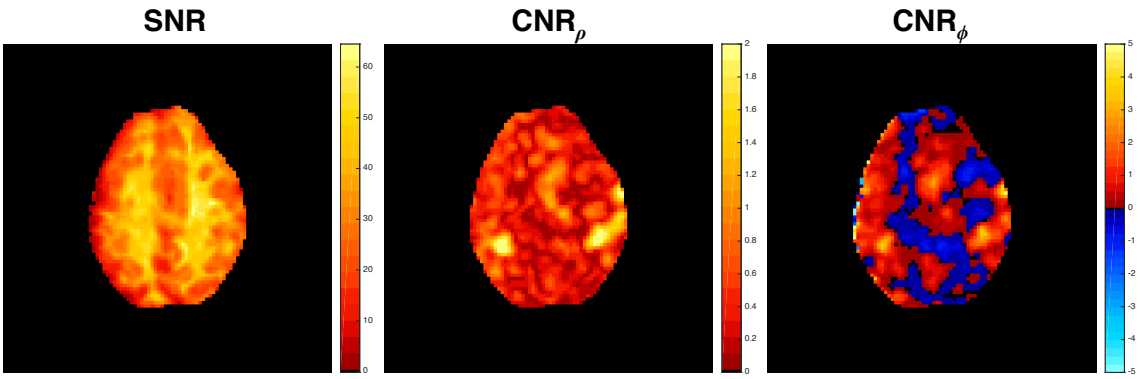


**Figure 2.3:** The SNR, CNR$_\rho$, and CNR$_\phi$ maps for the experimental human data.

## 2.4 Results

### 2.4.1 Simulation Results

In Fig. 2.4, the Fisher-*z* transform statistics for the magnitude-only and complex-valued correlations are computed for the surfaces generated with the parameters described in Fig. 2.2. Including the phase half of the data in the complex-valued correlation calculation yields an increased sensitivity of the correlation value, as illustrated by comparing the top left corner of the Fisher-*z* map in Fig. 2.4a to the one in Fig. 2.4b, with a difference map of magnitude-only and complex-valued in Fig. 2.4c. The additional information of the phase time-series improves the strength of correlation detected at lower magnitude CNR values.

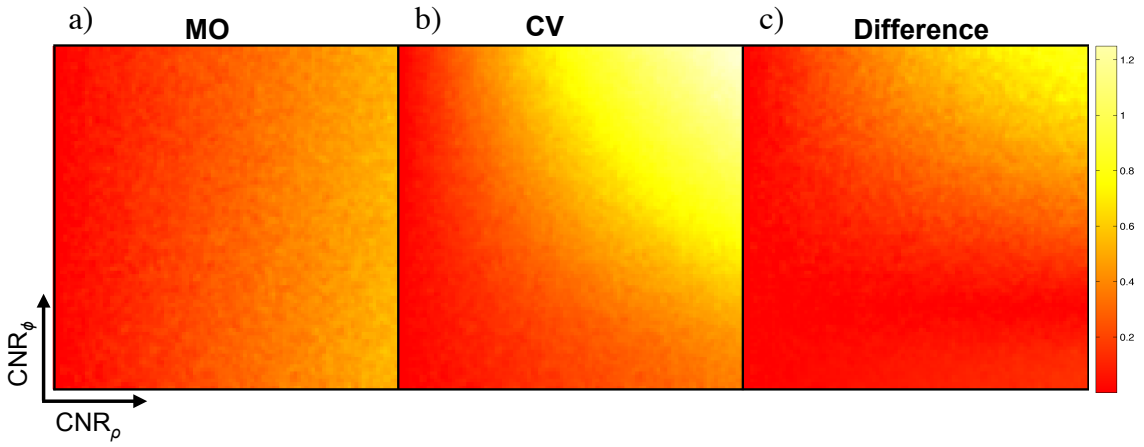


**Figure 2.4:** The Fisher-*z* transform of the (a) magnitude-only, MO, and (b) complex-valued, CV, correlation, and the (c) difference (CV – MO) between the correlations.

### 2.4.2 Human Subject Data Results

Fig. 2.5 and Fig. 2.6 contain the four seed voxel complex-valued and magnitude-only correlation maps for the experimental fMRI data in the motor cortex and supplementary motor cortex. In Fig. 2.5b, the magnitude-only and complex-valued correlation maps are identical since computing the magnitude-only and complex-valued correlations are equivalent for a magnitude-only data set. In Fig. 2.6b, the magnitude-only and complex-valued correlation maps are noticeably distinguishable since computing the magnitude-only and complex-valued correlations are not equivalent for a complex-valued data set. As described in Eq. [2.6], the spatial correlations are computed with the temporal frequencies, which are aggregated into bands as seen in Fig. 2.5a and Fig. 2.6a. The magnitude-only correlation maps appear to contain more correlations outside the expected task-activated region compared to the complex-valued maps. Particularly in the low CNR seed voxels, the less defined motor cortex in the magnitude-

only correlation maps corroborates the results observed in the simulation in Section 2.4.1. The complex-valued correlations have a higher sensitivity than the magnitude-only correlations in both regions with activation. All voxels are located in the motor cortex or supplementary motor cortex, and exhibit task-activated correlation in $R_2$, where the task frequency peak is located, as in Fig. 2.5a and Fig. 2.6a. In Fig. 2.5b, the general location of the apparent false positive magnitude-only correlation is around the edge of the brain as is characteristic of a motion artifact. Since the data has been minimally processed, motion artifacts are present in the data and have not been corrected, as observed along the edges of the brain.

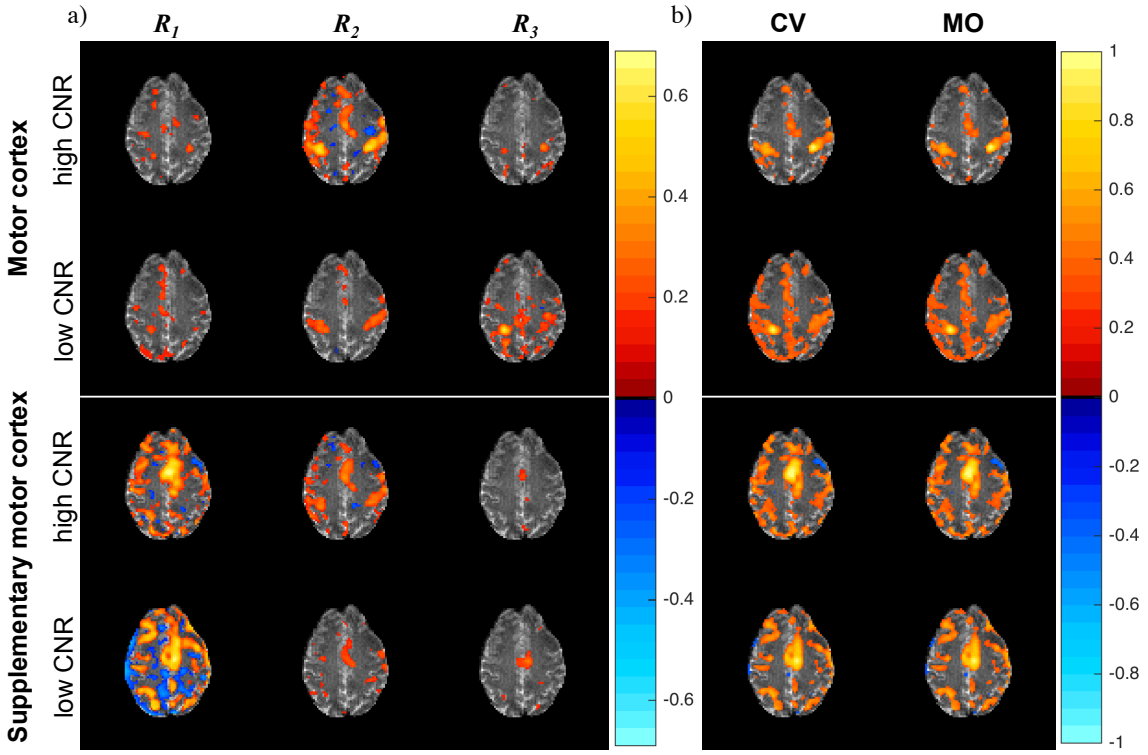


**Figure 2.5:** Experimental magnitude-only, MO, fMRI spatial correlation maps for each seed voxel (a) by the correlation bands, $R_1$, $R_2$, $R_3$ corresponding to the frequency band ranges 0.0009 - 0.024 Hz, 0.026 - 0.037 Hz, 0.038 - 0.08 Hz, and (b) the total correlation map magnitude-only, MO, and complex-valued, CV, and for high and low CNR in motor cortex and supplementary motor cortex.

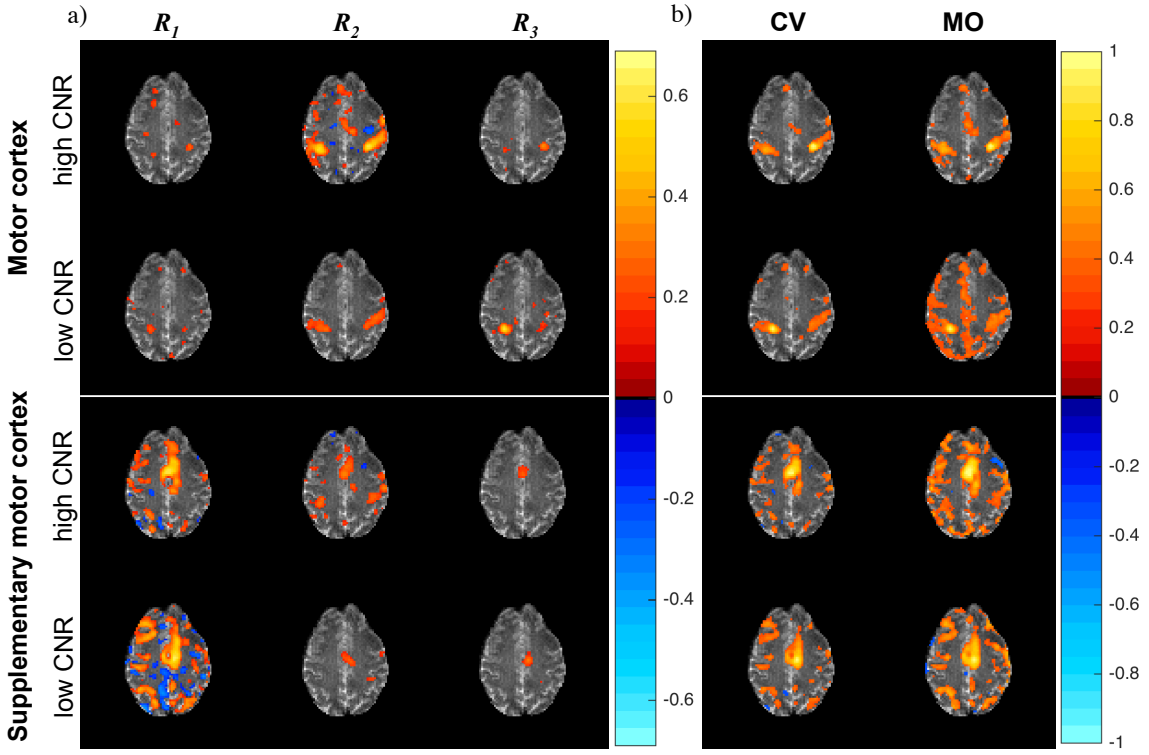


**Figure 2.6:** Experimental complex-valued, CV, fMRI spatial correlation maps for each seed voxel (a) by the correlation bands, $R_1$, $R_2$, $R_3$ corresponding to the frequency band ranges 0.0009 - 0.024 Hz, 0.026 - 0.037 Hz, 0.038 - 0.08 Hz, and (b) the total correlation map magnitude-only, MO, and complex-valued, CV, for high and low CNR in motor cortex and supplementary motor cortex.

## 2.5 Discussion

A linear matrix representation of correlation between complex-valued time-series in the temporal Fourier frequency domain for functional MRI (fMRI) data analysis was developed. In a simulation comparing decreasing CNR magnitude and phase values, it was illustrated that the Fisher-*z* transform of complex-valued correlations were higher than for magnitude-only correlations for low CNR fMRI time-series. In the experimental human data, a comparison of $R_2$ in Fig. 2.6a and Fig. 2.6a shows increased sensitivity of

estimating correlations with including the phase time-series. These results agree with previous studies investigating the statistical power of using complex-valued data over magnitude-only data in fMRI studies. In comparison to the magnitude-only correlations, the complex-valued correlations have reduced error, and more distinctive regions of activation in the motor cortex and the supplementary motor cortex for voxels with lower magnitude and phase CNR, since the magnitude-only signal has no rotational information to leverage for sensitivity. While the framework is demonstrated for task fMRI data, a natural application of this framework is to non-task fMRI, where the spatial correlation is measured to detect long-range connectivity.

The temporal Fourier frequency description in this study is also advantageous to locate the temporal frequency range where correlations are induced. Common processing and reconstruction methods have been shown to induce correlation of no biological origin [Davey et al. 2013; Bruce et al. 2011; Bruce et al. 2013]. In this study a framework is presented where signal processing operations and parallel image reconstruction procedures, applied to the complex-valued *k*-space readout, can be represented as real-valued matrix operators. The second order temporal frequency spatial covariance representation describes spatial correlation as a function of increased overlapping frequency content. Consider a scenario where initially voxel *a* and *b* are correlated, *b* and *c* are correlated, but *a* and *c* are not correlated. If the reconstructed images are smoothed, which has been previously shown to induce correlation, spatial correlation between *a* and *b* arises from overlapping frequency content between temporal frequency spectrums of *a* and *c*. Similar reasoning can be used to discuss the correlation between *b* and *c,* and the lack of correlation between *a* and *c.* As shown in Section 2.4.1, the matrix multiplication

of the linear operators with the spatial covariance matrix, quantitatively describes the compounding impact of spatial and temporal operators to the second order temporal frequencies. Combining this matrix multiplication framework with biologically or experimentally relevant frequency bands pertaining to fMRI data, provides insight into the impact of signal processing on statistical analysis and clinical interpretations from the data. The application of the theory to complex-valued data validates the increased statistical strength of using complex-valued models, specifically in minimally processed data sets or data sets with high noise variability. Including the phase in the analysis increases the sensitivity of the correlation in low magnitude contrast-to-noise ratio functional MRI data.

# Chapter 3: mSPECS

## 3.1 Introduction

This chapter presents an SMS reconstruction method, a Multi-coil Separation of Parallel Encoded Complex-valued Slices (mSPECS), for a Hadamard encoded MB acquisition in fMRI. An early SMS imaging strategy used only receiver coil sensitivity profiles to separate the individual slice images [Larkman et. al, 2001]. More recently, studies combine coil sensitivities along with the use of incremental shifts in either the frequency or the phase encoding directions [Setsompop et. al, 2013]. These CAIPRIHANA shifts in the FOV achieve a larger differential among the coil sensitivity profiles and aliased voxel values, improving the stability, or condition number, of the separation matrix and aliased voxel separation. Implementing multiple slice image encoding methods allows higher MB factors in SMS-fMRI acquisitions, as there is more spatial information to disentangle the signal. With SMS imaging, temporal efficiency is limited by high-resolution images, or improved at the expense of aliasing artifacts in previously aliased slices. Efforts have been made to characterize and alleviate signal leakage in separated slice images in the context of optimized SMS acquisition and reconstruction methods [Moeller S et. al, 2012; Setsompop et. al, 2013; Cauley et. al, 2014]. Despite the advancements in SMS imaging, as acceleration factors increase, there is not always sufficient information for placing the BOLD signal in the un-aliased voxels, resulting in signal leakage in the previously aliased voxels. SMS inter-slice signal leakage may be non-uniform across previously aliased slices, making it difficult to

identify the source of the image distortion, and the unsatisfactory slice image separation may appear as brain connectivity during the fMRI analysis [Todd et. al, 2016].

To use Hadamard phase encoding in SMS acquisitions, the RF pulse modulates the phase magnetization in each excited slice image, so a single *k*-space readout is reconstructed into a single slice image with the excited slices superimposed [Muller et. al, 1988; Souza et. al, 1988]. With Hadamard encodes, a unique phase is imparted to each slice in a cyclical pattern throughout the complex-valued time-series, individual complex-valued slice images are resolved through solving a system of linear equations over sequential time repetitions, with no net acceleration achieved after the slice separation. With the mSPECS reconstruction for Hadamard encoded aliased slice images, a MB factor of $n_S$ simultaneously excited slices achieves an acceleration factor up to $A=n_S$. In this dissertation, the MB factor refers to the number of aliased slice images acquired during the slice image acquisition, and $A$ refers to the observed acceleration after the aliased slice image separation.

The mSPECS reconstruction model combines the spatial encoding information from a phased array of multi-channel receive coils and the intrinsic orthogonal properties of Hadamard matrices. The standard in the SMS-fMRI reconstruction methods is to derive spatial information from fully sampled reference data to derive spatial information regarding the individual slice images, i.e. the multi-channel receive coil sensitivity profiles, or calibrate the aliased slice time-series. In mSPECS, fully sampled complex-valued calibration images are bootstrapped sampled and artificially aliased. The bootstrap sampling algorithm at each time point is the key mechanism of the mSPECS reconstruction to prevent induced correlation between previously aliased voxels, and

most significantly, to accurately place the BOLD signal in the separated slice images. Without the mitigation inter-slice signal leakage in SMS-fMRI acquisition and reconstructions, brain networks will not be appropriately modeled in whole volume fMRI studies.

### 3.2 Theory

The Multi-coil Separation of Parallel Encoded Complex-valued Slices (mSPECS) reconstruction method is a one-step process of slice image separation and coil image combination, as opposed to methods of separating the coil images for each slice image then combining the $n_C$ coil images into a single image. The coil sensitivity profiles are derived from fully sampled slice images, i.e. from slice images acquired with no in-plane or through plane acceleration. In the mSPECS method, $H$, as constructed in Eq. [1.7], is the Hadamard aliasing matrix for an experiment with $n_S$ aliased slice images, and is of dimension $n_S \times n_S$. For example, an acquisition of $n_S = 4$ aliased slice images uses the orthogonal Hadamard aliasing matrix,

$$H = \begin{bmatrix} 1 & 1 & 1 & 1 \\ 1 & -1 & 1 & -1 \\ 1 & 1 & -1 & -1 \\ 1 & -1 & -1 & 1 \end{bmatrix}.$$

The scaling of Hadamard matrices in powers of 2 is visually demonstrated in Fig. [1.5]. Row $\delta$ and column $z$ of $H$ is denoted $H_{\delta,z}$ for the Hadamard aliasing pattern $\delta$, corresponding to a given TR, for slice $z$. The $n_S$ aliased slice images is the number of aliased slice images per packet, also known as the MB factor. The term packet refers to the number of aliased slice groups, i.e. $n_S = 4$ for 2 packets is a total of 8 slices images

acquired with MB 4. For a full volume acquisition, multiple interleaved slice image packets are excited for a TR, as shown in Fig. 1.6. Fig. 3.1 is a diagram of the slice profiles for 2 aliased slice images in 2 packets acquired over 2 TRs, where the first TR corresponds to the [+ +] Hadamard excitation, the second TR corresponds to the [+ -] Hadamard excitation, then the pattern will repeat for the subsequent TRs.

The remaining parts of the Theory section is divided into three parts, first is a description of a single aliased voxel value from a Hadamard encoded acquisition measured at multiple coils, second is a description of the bootstrap sampling and the artificial aliasing of the voxel values from the calibration slice images measured at multiple coils, and third is a description of the separation of the aliased voxel values with a discussion on the correlation of the previously aliased voxel values.

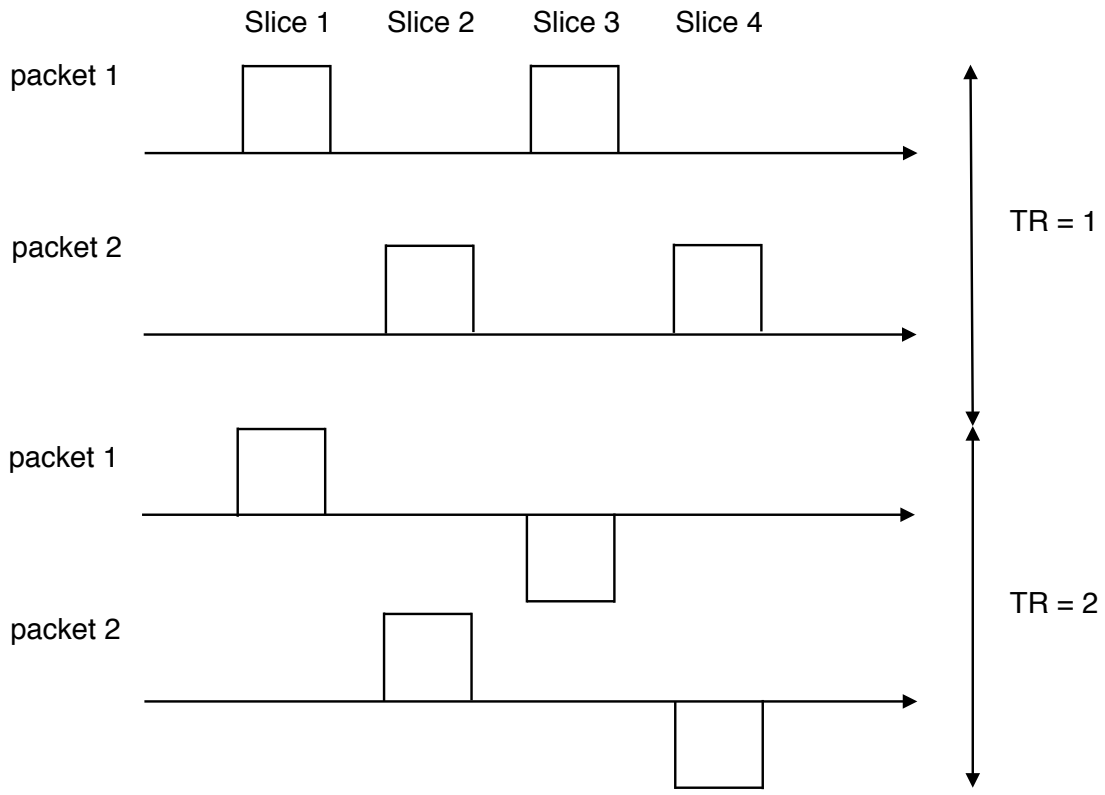


**Figure 3.1:** Slice profiles for a Hadamard encoded acquisition of $A = n_S = 2$ aliased slice images in 2 packets for a total of 4 slice images.

***A Single Aliased Voxel***

In one packet, a single aliased voxel, $a_{j,\delta}$, in the same $(x,y)$ voxel location across $n_S$ slices, with the Hadamard encode $\delta$, measured at coil $j$, in image space is written as the summation

$$a_{j,\delta} = \sum_{s=1}^{n_S} H_{\delta,s} S_{j,s} \beta_s + \varepsilon_j. \quad [3.1]$$

The Hadamard coefficient $H_{\delta,z}$ will be either 1 or -1, and the 2×1 vector $a_{j,\delta}$ is the real and imaginary parts of an aliased voxel acquired with the Hadamard aliasing pattern $\delta$ measured at coil $j$. In Eq. [3.1], $a_{j,\delta}$ is written as the sum of the 2×1 vector $\beta_z$, the real and

imaginary parts of the true voxel value in slice $z$, weighted by the 2×2 matrix of real and imaginary coil sensitivities at coil $j$. The real and imaginary coil sensitivities correspond to the same $(x,y)$ voxel location as $\beta_z$ for slice $z$ at coil $j$, in a skew symmetric matrix, $S_{j,z} = [S_R,-S_I;S_I,S_R]_{j,z}$.

The 2×1 vector $\varepsilon_j=(\varepsilon_{jR},\varepsilon_{jI})$ is the measurement error with real and imaginary parts at coil $j$ with a mean of $E(\varepsilon_j) = 0$ and covariance of $\text{cov}(\varepsilon_j) = \sigma^2 I_2$.

To separate the $n_S$ aliased voxels at a single voxel location, the goal is to estimate $\beta$, the separated voxel values from one packet. The number of sequential time-points, $n_\alpha$, where $n_\alpha$ is an integer between 1 and $n_S$, is the number of sequential TRs in the Hadamard encoded acquisition included in the separation of a single separated aliased voxel at one time point. If the data is acquired in packets of $n_S$ aliased slices, the net acceleration of the slice image time-series acquisition is

$A=n_S/n_\alpha$.

The measured aliased voxel in Eq. [3.1] is generalized across $n_C$ coils for $n_S$ aliased slices with $n_\alpha$ sequential time-points included in the separation, as

$$a = X_A\beta+\varepsilon. \quad [3.2]$$

In Eq. [3.2], $a$ and $\varepsilon$ are of dimension $2n_Cn_\alpha\times1$, and the error vector, $\varepsilon$, has the mean of

$E(\varepsilon) = 0$,

and a covariance of

$$\text{cov}(\varepsilon) =\sigma^2 I_{2n_Cn_\alpha}, \quad [3.3]$$

$X_A$ is of dimension $2n_Cn_\alpha\times2n_S$, and $\beta$ is of dimension $2n_S\times1$. For the $\delta^{\text{th}}$ aliasing pattern, the aliasing matrix $(X_A)_\delta$ of dimension $2n_C\times2n_S$ is constructed by multiplying the Hadamard coefficients with the coil sensitivities,

$$(X_A)_\delta = \left[ H_{\delta,1} \begin{pmatrix} S_{1,1} \\ \vdots \\ S_{n_C,1} \end{pmatrix}, \ldots, H_{\delta,n_S} \begin{pmatrix} S_{1,n_S} \\ \vdots \\ S_{n_C,n_S} \end{pmatrix} \right].$$

This is generalized to $X_A$, of dimension $2n_\alpha n_C \times 2n_S$, for the incorporation of $n_\alpha$ sequential TRs in the aliased voxel separation,

$$X_A = [(X_A)_1, \ldots, (X_A)_{n_\alpha}]'. \quad [3.4]$$

Similar to previous efforts to disentangle simultaneously excited slices with coil sensitivities [Larkman et al., 2001], although with an additional phase manipulation [Muller et al., 1988; Souza et al., 1988], the $2n_S \times 1$ vector of separated voxel values, $\hat{\beta}$, can be estimated,

$$\hat{\beta} = (X'_A X_A)^{-1} X'_A a,$$

with a covariance between the previously aliased voxels across the $n_S$ slices,

$$\text{cov}(\hat{\beta}) = \sigma^2 (X_A' X_A)^{-1}. \quad [3.5]$$

To reduce the covariance between previously aliased voxels, and thus minimize correlation induced from the aliased voxel separation process, the mSPECS method combines the coil and phase encoding with calibration images into the least squares estimation. The novelty of the mSPECS reconstruction is a bootstrapping sampling and artificial aliasing of calibration voxel values, from a separate acquisition of fully-sampled slice image time-series, that are artificially aliased in the remaining Hadamard pattern for a given TR. This mechanism of incorporating calibration slice images in the SMS-fMRI reconstruction, prevents inter-slice signal leakage, which may present as “clusters” of false activation, between previously aliased voxel regions, as a result of correlation induced during aliased voxel separation.

***Bootstrap Sampling and Artificial Aliasing***

To separate an aliased coil slice image, $n_S$ bootstrap sampled coil slice images from the fully-sampled calibration slice image time-series are averaged, then artificially aliased. This mean bootstrap sampling and artificial aliasing algorithm is repeated for each time-point in the aliased slice image time-series. For a single time-point, a voxel in the same ($x,y$) location across the $n_S$ slices measured at $n_C$ coils, bootstrap sampled from the calibration slice image time-series, is represented in the $2n_Sn_C\times1$ vector, $\nu$, and the mean bootstrap sample for each time point is represented in the $2n_Sn_C\times1$ vector, $\bar{\nu}$ . The true mean voxel values, to be aliased in the same ($x,y$) location across the $n_S$ slices, from the calibration slice images are represented by the $2n_S\times1$ vector $\mu$, with the same voxel indices as in $\beta$ for Eq. [3.2]. The vector, $\nu$, has a $2n_Sn_C\times1$ error vector, $\eta$, with $\eta=(\eta_R,\eta_I)$ corresponding to the real and imaginary parts of the measurement error of the coil calibration slice images for $n_S$ slices measured at $n_C$ coils. The calibration slice coil images measurement error has a mean of

$E(\eta)=0$,

and a covariance of

$$\text{cov}(\eta)=\sigma^2 I_{2n_Cn_S}. \qquad [3.6]$$

In the mSPECS model, for the $\delta^{\text{th}}$ aliasing pattern, in the aliased voxel separation in Eq. [3.2], the mean calibration images, $\bar{\nu}$, are artificially aliased with the $2n_C(n_S-1)\times2n_Sn_C$ aliasing matrix $C_\delta$, is the Kronecker product of the +1 and -1 Hadamard coefficients and vectors of ones, is

$$C_\delta = \mathbf{1}_{n_C} \otimes [\bar{H}_{\delta,1} \otimes \mathbf{1}_2,\ldots, \bar{H}_{\delta,n_S} \otimes \mathbf{1}_2].$$

The $(n_S\text{-}1)\times n_S$ matrix $\overline{H}_\delta$ is the remaining $(n_S\text{-}1)\times n_S$ with the $\delta^{th}$ acquisition removed from the $H$ matrix, so that $C_\delta$ is the remaining $(n_S\text{-}1)$ orthogonal ways the true fully acquired voxels across the $n_S$ slices could be aliased with a Hadamard matrix. An illustration of the origin of $\overline{H}_\delta$ to create the potential aliasing matrices, $C_\delta$, for the $n_S$ aliasing patterns, is shown in Fig. 3.2 for a Hadamard encoded time-series with $n_S$=4 aliased slice images. Fig. 3.2a is the time-series aliasing pattern that repeats every $n_S$ TRs, denoted by the blue dotted line in the figure. The first 4 TRs correspond to Hadamard aliasing of the four aliased slice images shown in Fig. 3.2b, with the four aliasing patterns shown as the sum and difference of the individual slice images. Fig. 3.2c depicts the four artificial aliasing matrices for MB4 for the $\delta^{th}$ aliasing pattern equivalent to the $\delta^{th}$ row of a Hadamard matrix of dimension $n_S\times n_S$ where $\delta$=1…$n_S$, and the gray shaded region designated the $n_S$-1 ways to artificially alias the calibration slice images corresponding to the $\delta^{th}$ aliasing pattern.

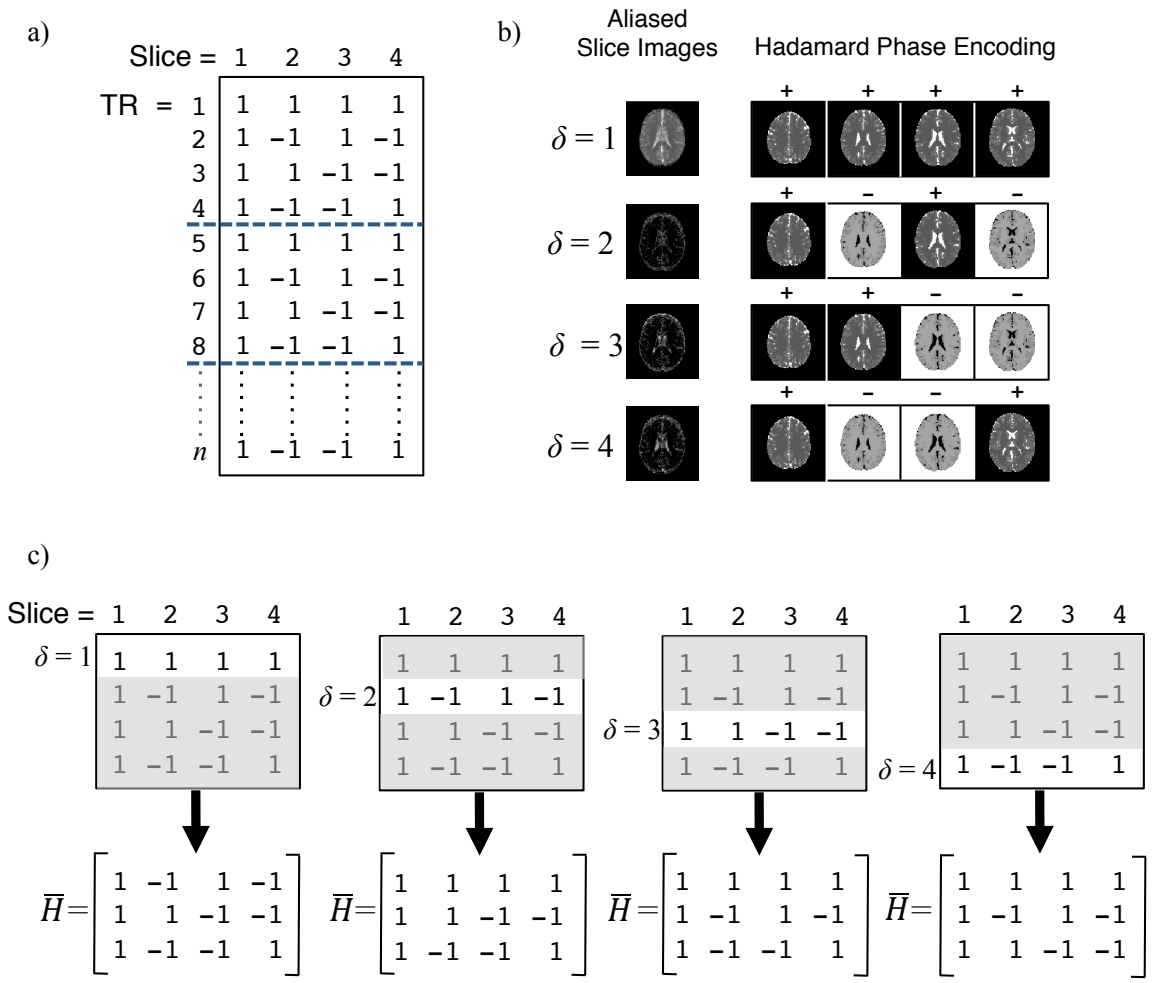


**Figure 3.2: (**a) The rotating Hadamard encodes to alias $n_S$=4 slice images (column) for $n$ time-points (row), repeated every $n_S$ TRs, denoted by the blue dotted line, (b) $n_S$=4 aliased slice images acquired over 4 consecutive time repetitions are the sum and difference of the individual complex-valued slice images, (c) and the corresponding artificial aliasing matrices, $\bar{H}$, for the $\delta^{th}$ aliasing pattern.

To incorporate $n_\alpha$ subsequent TRs from the aliased voxel acquisition, the corresponding aliasing matrices, $C_\delta$, are placed along the diagonal to create a single aliasing matrix $C$, of dimension $2n_C n_\alpha(n_S\text{-}1)\times 2n_S n_C n_\alpha$,

$$C = \begin{bmatrix} C_1 & & 0 \\ & \ddots & \\ 0 & & C_{n_\alpha} \end{bmatrix} \qquad [3.7]$$

Artificially aliasing the mean bootstrap sampled voxels, $\bar{v}$, and the corresponding error vector, $\eta$, from the calibration images with the aliasing matrix in Eq. [3.7] results in a $2n_\alpha n_C(n_S\text{-}1)\times 1$ vector,

$$\upsilon = C\bar{v} = C_A\mu + C\eta, \qquad [3.8]$$

where $\mu$ has been previously defined as the $2n_S\times 1$ vector of the true calibration voxel values with real and imaginary parts. The matrix $C_A$ is a coil sensitivity matrix with Hadamard coefficients, analogous to $(X_A)_\delta$, for the artificially aliased calibration voxels is the $2n_C(n_S\text{-}1)\times 2n_S$ matrix,

$$(C_A)_\delta = \left[\overline{H}_{\delta,1}\otimes\begin{pmatrix} S_{1,1}\\ \vdots \\ S_{n_C,1}\end{pmatrix},\ldots,\overline{H}_{\delta,n_S}\otimes\begin{pmatrix} S_{1,n_S}\\ \vdots \\ S_{n_C,n_S}\end{pmatrix}\right].$$

Similar to Eq. [3.4], $(C_A)_\delta$ is generalized to $C_A$, of dimension $2n_\alpha n_C(n_S\text{-}1)\times 2n_S$, for the incorporation of $n_\alpha$ sequential TRs in the aliased voxel separation,

$C_A = [(C_A)_1, \ldots, (C_A)_{n_\alpha}]'$.

### *A Separation of Aliased Voxel Values*

With the mSPECS approach, to separate the aliased voxel values, Eq. [3.2] and Eq. [3.8] are concatenated into one equation,

$$\begin{bmatrix} a\\ \upsilon\end{bmatrix} = \begin{bmatrix} X_A\beta\\ C_A\mu\end{bmatrix} + \begin{bmatrix} \varepsilon\\ C\eta\end{bmatrix}. \qquad [3.9]$$

If $y_a$ is the $2n_\alpha n_S n_C\times 1$ vector of acquired aliased voxel values stacked over the artificially aliased voxel values such that $y_a = (a', \upsilon')'$, and $X$ is the two aliasing matrices concatenated, $X=[X_A', C_A']'$ of dimension $2n_\alpha n_S n_C\times 2n_S$, then the separation of the aliased voxel values in Eq. [3.9] is a least squares estimate of the form

$\hat{\beta} = (X'X)^{-1}X'y_a$,

The $2n_S \times 1$ vector of estimated separated voxel values with real and imaginary parts, is also written

$\hat{\beta} = (X'_A X_A + C'_A C_A)^{-1}(X'_A a + C'_A \upsilon)$

To view the mSPECS approach as a Bayesian method, where $a \sim N(\beta, \sigma^2 I_{2n_c n_\alpha})$ and $\bar{v} \sim N(\mu, \sigma^2 I_{2n_c n_\alpha n_S})$, so the posterior mean is

$E[\hat{\beta}] = (X'_A X_A + C'_A C_A)^{-1}(X'_A \beta + C'_A \mu)$,

such that the separated voxel values are a weighted combination of prior and likelihood mean voxel values, or calibration and artificially aliased voxel values.

The covariance of the added measurement error of a measured aliased voxel in Eq. [3.2] measured at $n_C$ coils, which is $n_\alpha$ sequential TRs incorporated into mSPECS,

$$\text{cov}(\varepsilon) = \sigma^2 I_{2n_c n_\alpha} \quad [3.10]$$

and the covariance of the artificially aliased $n_S$ calibration voxel values measured at $n_C$ coils, which is $n_\alpha$ sequential TRs in Eq. [3.8] is

$$\text{cov}(C\eta) = \sigma^2 I_{2n_c n_\alpha (n_S - 1)}. \quad [3.11]$$

In both Eq. [3.10] and Eq. [3.11], there is no covariance between the real and imaginary parts, and a constant variance of $\sigma^2$ for both real and imaginary parts. The $2n_\alpha n_C n_S \times 2n_\alpha n_C n_S$ covariance matrix for the $2n_\alpha n_C n_S \times 1$ vector $y_a$, consisting of aliased and artificially aliased voxel values is

$$\text{cov}(y_a) = \begin{bmatrix} \sigma^2 I_{2n_\alpha n_C} & 0 \\ 0 & \tau^2 I_{2n_\alpha n_C (n_S - 1)} \end{bmatrix}. \quad [3.12]$$

If there is no variation, i.e. no random sampling of the calibration voxel values with mSPECS, among the average calibration slice images used to separate each aliased image then $\tau^2$=0. The bootstrapping adaptation averages $n_S$ randomly selected calibration images for each TR in $\bar{v}_j$ to obtain $\tau^2 = \sigma^2$, such that the covariance in Eq. [3.12] results in the $2n_S \times 2n_S$ matrix,

$\text{cov}(\hat{\beta}) = \sigma^2 (X_A' X_A + C_A' C_A)^{-1}$.

The inclusion of the calibration images through the mSPECS method reduces correlation between the previously voxel values, compared to Eq. [3.5], since $C_A' C_A$ acts as a regularizer, which improves the condition of Eq. [3.12]. In SMS-fMRI, induced correlation from the un-aliasing of the slice images throughout the time-series, presents as inter-slice signal leakage among previously aliased voxels, with false activation detected in these regions.

### 3.3 Methods

The mSPECS method is demonstrated with Hadamard encoded simulated phantom and experimental human data. With Hadamard matrix dimensions increasing in powers of two, the design of task timings must also increase in powers of two to accommodate various accelerations determined post acquisition, by varying $n_\alpha$ in the mSPECS method. Table 3.1 lists the accelerations and timings for both the simulation and the experimental human subject data. In both settings, the data is acquired with a MB factor = 8, i.e. $n_S$ = 8 aliased slices. An 8 second TR, for a net acceleration of 1, is based from the timing of full volume acquisitions, so 9 packets of 8 aliased slices are measured

yielding 72 slices in 8 seconds with no acceleration. The net acceleration after slice separation is defined as the number of aliased slices over the number of sequential TRs used included in the reconstruction,

$A = n_S / n_\alpha$ .

The notation "mSPECS 2" denotes an implementation of mSPECS with $A$=2. The number of sequential TRs used for reconstruction changes the TR length, from $TR_{acq}$ (the acquired TR length as defined in Fig. 3.1) to $TR_{sep}$ (the TR length of the separated slice image time-series) with

$TR_{sep} = TR_{acq} n_\alpha$.

The total time of the time-series remains the same, although the number of time points differs before and after slice separation, where the time-points post slice image separation is equivalent to the starting number of TRs divided by $n_\alpha$.

| Acceleration | TRs(acq) | Task | $n_S$ | $n_\alpha$ | $TR_{acq}$ | $TR_{sep}$ | TRs(sep) |
|---|---|---|---|---|---|---|---|
| mSPECS 1 | 600 | 16 s | 8 | 8 | 1 s | 8 s | 75 |
| mSPECS 2 | 600 | 16 s | 8 | 4 | 1 s | 4 s | 150 |
| mSPECS 4 | 600 | 16 s | 8 | 2 | 1 s | 2 s | 300 |
| mSPECS 8 | 600 | 16 s | 8 | 1 | 1 s | 1 s | 600 |

**Table 3.1:** Acquisition and reconstruction timings for mSPECS.

### 3.3.1 Digital Phantom Simulation

An fMRI digital phantom data set was generated with a block-design of task activity, with an initial rest of 64 seconds followed by 9 epochs of 32 seconds no task and 32 seconds task using MATLAB (The Mathworks, Natick, MA, USA). The data was

generated for eight sagittal slice images that are 96×96 in dimension to represent one packet in a full brain volume Hadamard encoded acquisition. The noiseless time series was generated for each slice image with a theoretical $T_2^*$ weighted phantom similar to [Karaman et al., 2016]. The initial $T_2^*$ weighted phantom has initial values between 0 and 1, then weighted for maximum SNR of 30 in the magnitude, yielding an approximate SNR of 30 in the CSF, 15 in the grey matter, and 7 in the white matter, and a mean phase is added to the slice images varied from 8π/36 to π/36 from slice one to slice eight decreasing in increments of π/36. The calibration time-series was generated with 40 TRs from the complex-valued phantom. The slices are first weighted by complex-valued simulated 16-channel coil sensitivity maps, then standard Gaussian noise was added to the real and imaginary components of the time series. The simulated coil profiles were generated with a bivariate normal probability density function, and the first 4 coils are placed in the four corners and the next 4 coils on the four edges, then repeated for a total of 16 receive coils. Sixteen weighting matrices, with values between 0 and 1, are generated, rotated for each slice, and applied to the coil profiles, such that each slice has a unique weighting of the 16-channel coil profiles. For the complex-valued coil profiles, a phase of π/12 is added to each coil profile.

In the simulation, the task was generated in one unique 6×6 voxel square region of interest (ROI) rotating clockwise for each slice with a magnitude CNR, as defined in Eq. [2.9], of 0.5. For a magnitude CNR of 0.5, the magnitude within the ROI is increased by 0.5 for 32 TRs and then returning to baseline for the following 32 TRs for the 9 epochs. Before the complex-valued time-series was summed in the slice direction, the Hadamard phase encoding was simulated. With no in-plane acceleration, i.e. mSPECS,

the rotating Hadamard pattern resembled Fig. 1.4, depending on the number of aliased slices or multiband factor. Once the complex-valued slices are multiplied by the +1 or -1 Hadamard phase encode coefficient, they weighted by the complex-valued 16-channel coil sensitivities, then summed in the slice direction. Standard Gaussian noise was added to the real and imaginary components of the time series. One time-series of Hadamard aliased images, simulated with MB8, was then separated using the mSPECS model and separated with $n_\alpha$=1, 2, 4, and 8, or equivalently written as mSPECS 1, mSPECS 2, mSPECS 4, mSPECS 8, and fMRI activation was calculated in each separated voxel using the complex-valued fMRI model in [Rowe 2005b].

### 3.3.2 Experimental Human Subject Data

An experimental fMRI human data set with Hadamard encoding was acquired with a visual flashing checkerboard stimulus presented in a block design with an initial 64 seconds rest followed by 9 epochs of 32 seconds on and 32 seconds off using a 3.0 T Discovery MR750 MRI scanner (General Electric, Milwaukee, WI) with a 32-channel receive coil. A visual task to maximize the region of activation in the sagittal slice orientation. The data was acquired with nine interleaved sagittal packets that are 96×96 in dimension and 2 mm thick. Eight Hadamard encoded slices are simultaneously magnetized within each slice packet, for a total of 72 slice images after slice image separation. The imaging parameters included a 24.0 cm FOV, a TR/TE of 1000/41 ms, a flip angle of 11°, an acquisition bandwidth of 250 kHz, and an effective echo spacing of 0.500 ms. The phase encoding direction was oriented as posterior to anterior (bottom to

top in images) and images were Nyquist ghost corrected. An experimental non-task fMRI human data set without Hadamard encoding, to be used as the calibration time-series, was acquired using a 3.0 T Discovery MR750 MRI scanner (General Electric, Milwaukee, WI) with a 32-channel receive coil. The data was acquired with 72 sagittal slices that are 96×96 in dimension and 2 mm thick. The imaging parameters included a 24.0 cm FOV, a TR/TE of 8000/41 ms, a flip angle of 11°, an acquisition bandwidth of 250 kHz, and an effective echo spacing of 0.500 ms. The phase encoding direction was oriented as posterior to anterior (bottom to top in images) and images were Nyquist ghost corrected.

Before applying the mSPECS separation to the aliased slices, a phase correction is applied to the aliased time-series, and both a phase and magnitude correction is applied to the calibration images. First, each Hadamard pattern in the aliasing phase time-series is corrected. The mean phase of each Hadamard pattern is estimated, and then subtracted from the phase time-series. The remaining error of the phase time-series is fit to a local third order polynomial, with a the local fit region of 11×11 voxels, and the mean phase is added back to the phase time-series. Second, the full complex-valued Hadamard aliased time-series is separated with addition and subtraction, and the mean phase of the separated slice time-series is estimated. The calibration image phase time-series is also corrected in the same way. The mean phase of the slice time-series is estimated, and then subtracted from the phase time-series. The remaining error of the phase time-series is again fit to a local third order polynomial, with a the local fit region of 11×11 voxels, and the mean phase estimated from the Hadamard separated images is added back to the calibration time-series. The difference in magnitude between the voxels in the calibration coil images and Hadamard coil image time-series is reconciled by multiplying the

magnitude calibration images with a magnitude difference ratio of 0.2. The magnitude difference ratio is the mean magnitude Hadamard separated images at each coil divided by the mean magnitude calibration images at each coil, with the regions of signal dropout masked in the Hadamard separation for the estimation of the ratio.

The raw 32-channel receive coil sensitivity maps are estimated from the calibration slice images. The complex-valued coil sensitivity profiles are estimated by averaging the image mean in the time dimension at each coil. The mean coil images are normalized, by averaging the mean coil images to a single image, and the sensitivity maps are fit to a local polynomial, the local fit region is 13×13 voxels and the polynomial is of order three, to remove variability in the maps. The aliased images were then separated using the mSPECS model, and fMRI activation was calculated in each separated voxel using the complex-valued fMRI model in [Rowe 2005b]. The Hadamard aliased images, acquired with MB8, was then separated using the mSPECS model and separated with $A$=1, 2, 4, and 8, or equivalently written as mSPECS 1, mSPECS 2, mSPECS 4, mSPECS 8, and fMRI activation was calculated in each separated voxel using the complex-valued fMRI model in [Rowe 2005b].

## 3.4 Results

### 3.3.1 Simulation Results

The mean magnitude and phase for the calibration slice images for the eight complex-valued aliased slice images for the digital phantom simulation are shown in Fig.

3.3, the calibration slice images are measured with the simulated 16-channel receive coils and the fully sampled coil images are combined with a SENSE reconstruction. The mean magnitude and phase for the Hadamard separated slice images for the eight complex-valued aliased slice images for the digital phantom simulation are shown in Fig. 3.4, the aliased slice images are measured with the simulated 16-channel receive coils, separated with adding and subtracting the complex-valued images, and the separated slice coil images are combined with a SENSE reconstruction. In Fig 3.5 and Fig 3.6 are the calibration magnitude and phase slice images of the mean time-series separated for the reconstructions of mSPECS 1, mSPECS 2, mSPECS 4, and mSPECS 8. Across the four accelerations, in the mean separated slice magnitude and phase images, there are no signs of residual aliasing (slice leakage) induced from slice image separation.

After the mSPECS slice image separation of the aliased time-series, the fMRI activation statistics are calculated in each voxel with a complex-valued activation model [Rowe 2005b]. The *z*-scores for the activation statistics are mapped in Fig 3.7, and the regions where the activation was placed is highlighted by the green box in each slice. The activation maps are thresholded at 2, and the region outside the digital phantom is masked. Since the activation is placed in a unique 6×6 region in each slice image, before simulating the aliased time-series, and there are no incremental shifts in the FOV, inter-slice signal leakage stemming from the slice separation process is easily identifiable by visually examining previously aliased voxel locations. The regions within the green boxes show strong activation clusters. The average *z*-scores increase as the acceleration increases, as a higher sampling rate corresponds to a strengthened statistical significance, although the *z*-scores in mSPECS 4 and mSPECS 8 appear similar. The *z*-scores in

mSPECS 2 are higher than mSPECS 1, yet the difference between the *z*-scores in mSPECS 2 versus mSPECS 4 or mSPECS 8 is not as large. There are no clusters of "active" voxels outside the green boxes in Fig 3.7, so active voxels outside indicate false positives from noise in the time-series, rather than inter-slice signal leakage.

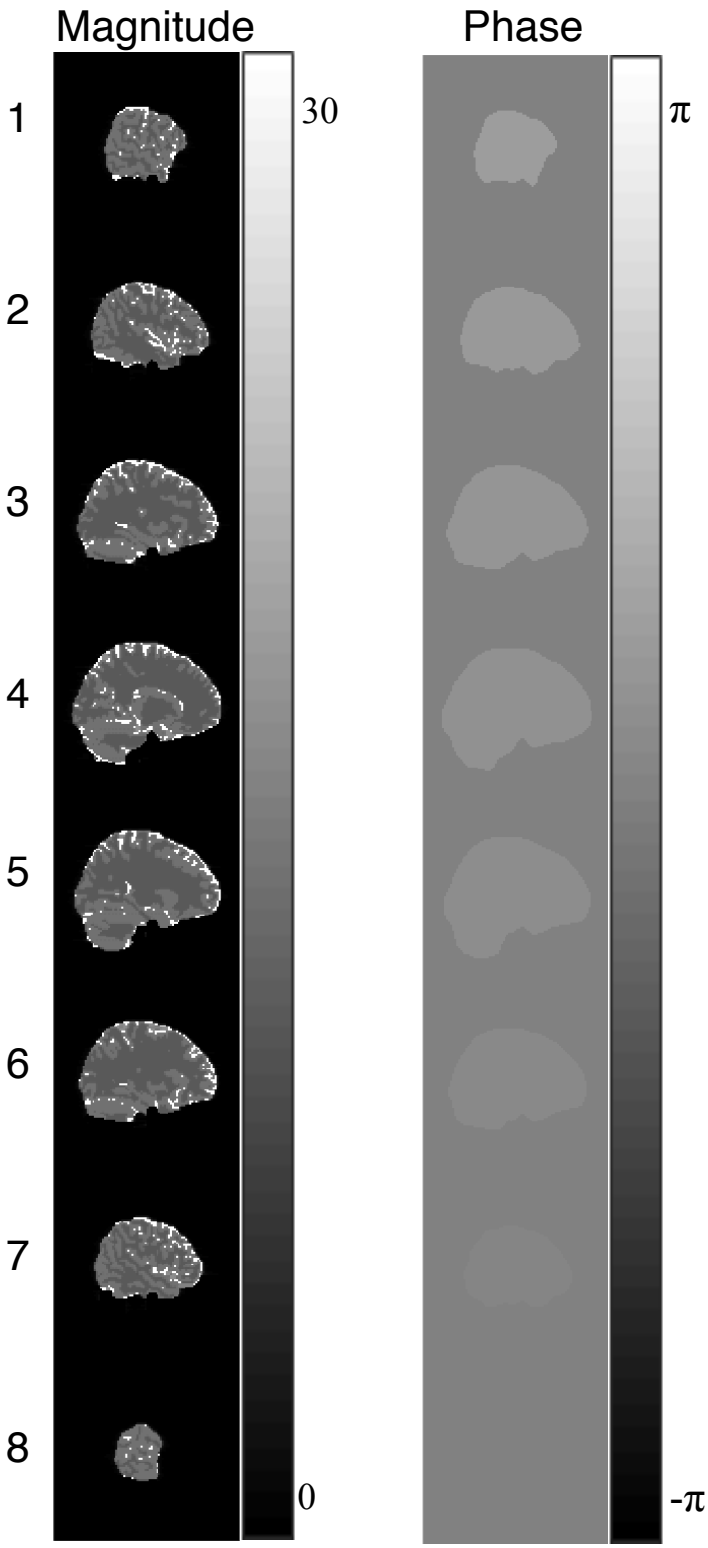


**Figure 3.3**: Mean calibration digital phantom magnitude slice images and phase slice images, with the numbering 1 through 8 referring to the slice image number.

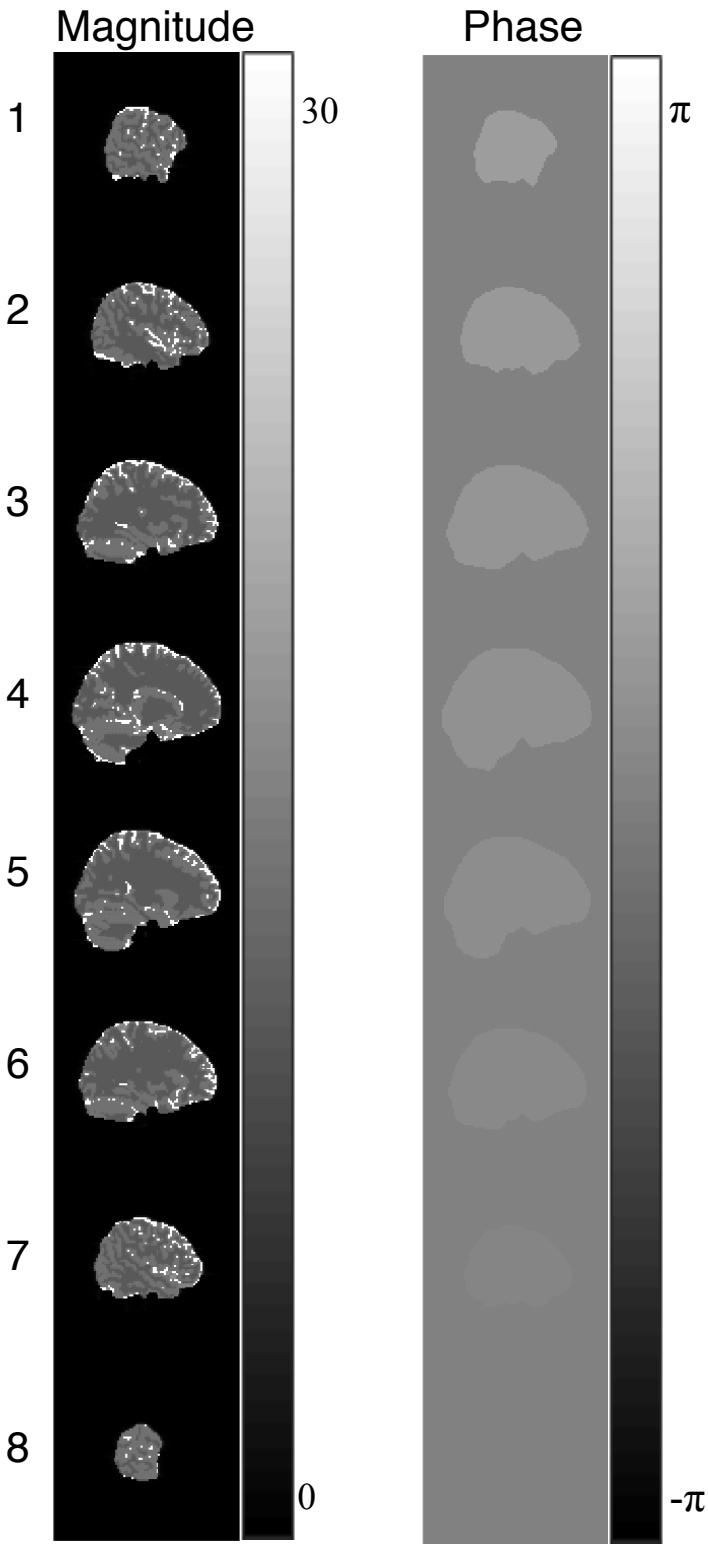


**Figure 3.4**: Time-series mean Hadamard separated digital phantom magnitude slice images and phase slice images, with the numbering 1 through 8 referring to the slice image number.

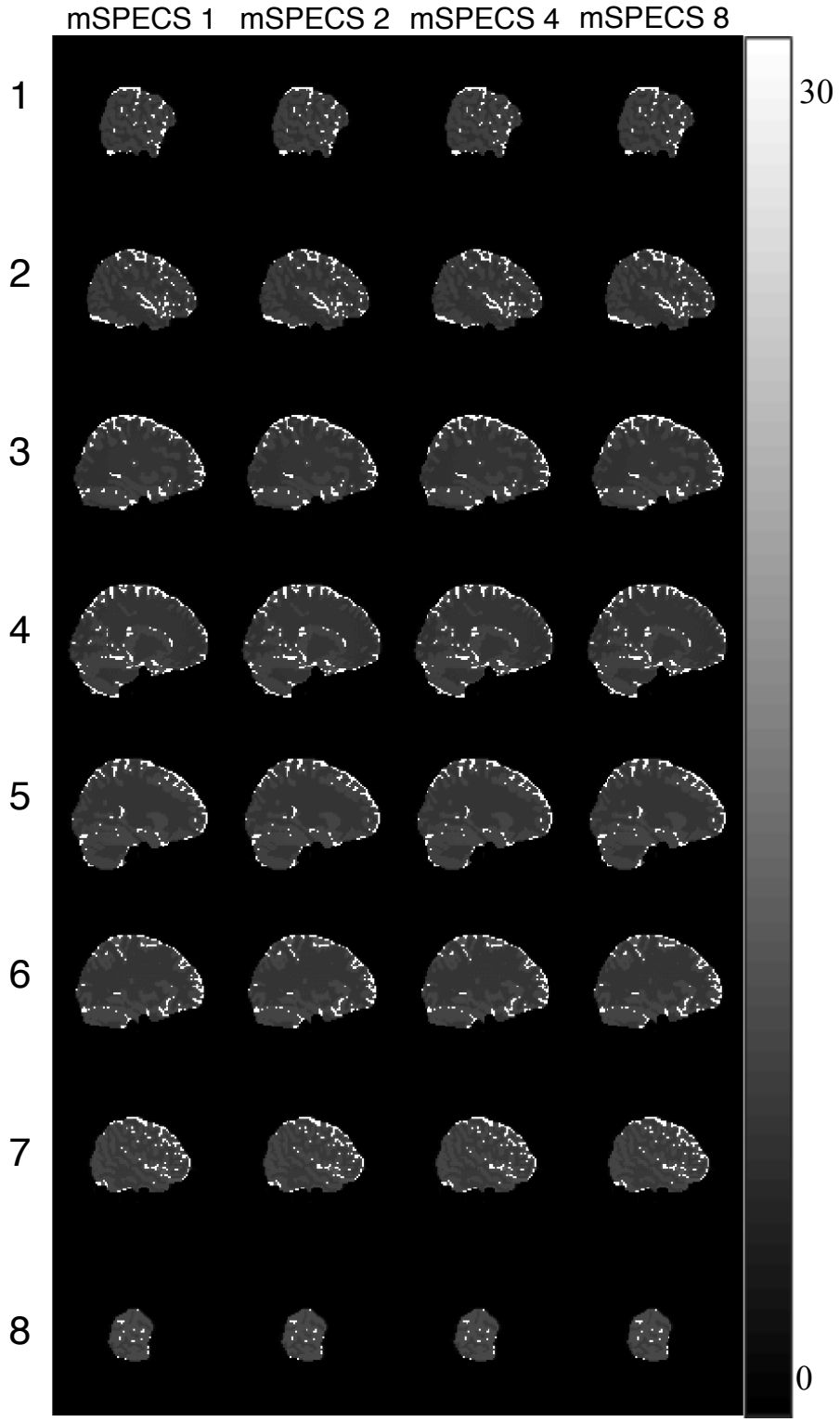


**Figure 3.5:** Mean magnitude mSPECS separated slice images from the Hadamard encoded digital phantom simulation for the accelerations of mSPECS 1, mSPECS 2, mSPECS 4, and mSPECS 8.

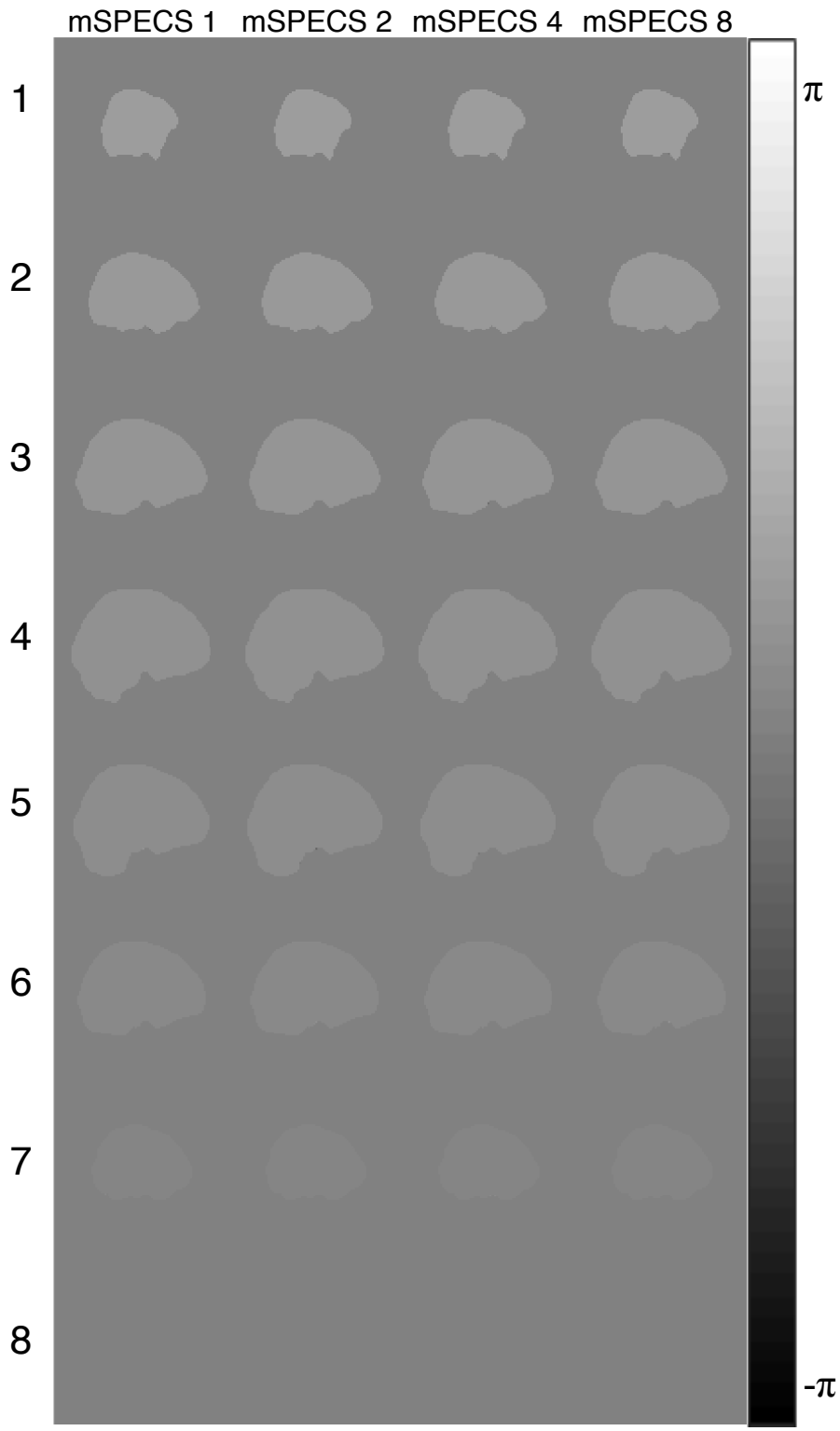


**Figure 3.6:** Mean phase mSPECS separated slice images from the Hadamard encoded digital phantom simulation for the accelerations of mSPECS 1, mSPECS 2, mSPECS 4, and mSPECS 8.

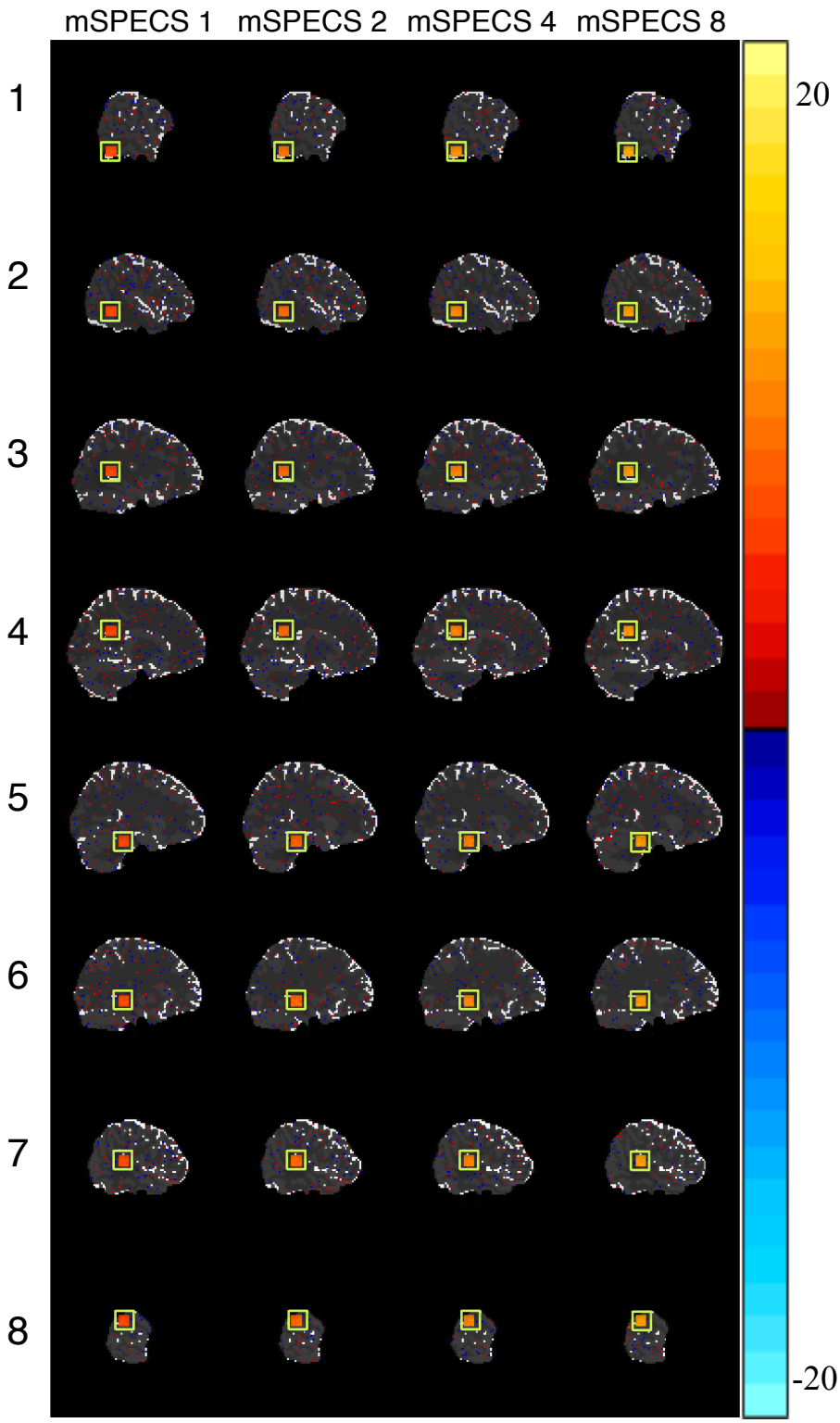


**Figure 3.7:** Activation statistics for the mSPECS separated slice images from digital phantom simulation for the accelerations of mSPECS 1, mSPECS 2, mSPECS 4, and mSPECS 8.

### 3.3.2 Human Subject Data Results

The mean magnitude and phase for the calibration slice images for the eight complex-valued aliased slice images for the digital phantom simulation are shown in Fig. 3.8, the calibration slice images are measured with the 32-channel receive coils and the fully sampled coil images are combined with a SENSE reconstruction. The mean magnitude and phase for the Hadamard separated slice images for the eight complex-valued aliased slice images for the digital phantom simulation are shown in Fig. 3.9, the aliased slice images are measured with the 32-channel receive coils, separated with adding and subtracting the complex-valued images, and the separated slice coil images are combined with a SENSE reconstruction. In Fig 3.10 and Fig 3.11 are the calibration magnitude and phase time-series mean of the slice images separated for the reconstructions of mSPECS 1, mSPECS 2, mSPECS 4, and mSPECS 8. In the four accelerations, there is signal dropout in the same locations across for each slice image. The signal dropout regions in the magnitude in Fig. 3.9 correspond to the same regions seen in Fig. 3.10. The mSPECS separation is susceptible to the same signal dropout observed in the addition and subtraction schemes. This signal dropout is a data quality issue, arising from complications with subject motion, rather than a direct result of the mSPECS separation itself. As acceleration increases, the mean magnitude images in Fig 3.10 show less decreased signal attenuation. During acquisition if there is a “bad” aliasing pattern throughout the time-series, i.e. the +/- orthogonality is not maintained during the slice excitations, the impact will lessen as acceleration increases with the mSPECS approach to aliased slice image separation.

After the mSPECS slice image separation of the aliased time-series, the fMRI activation statistics are calculated in each voxel with a complex-valued activation model [Rowe 2005b]. The *z*-scores for the activation statistics are mapped in Fig 3.12. The activation maps are thresholded at 1.5, and the region outside the brain is masked. While there does not appear to be signal leakage from the BOLD signal, the activation maps are noisy, which may be potentially structured noise as a result of subject motion. Slice 6 shows the most well defined region of activation in the visual cortex, this finding corroborates the signal dropout observed in the magnitude images in Fig. 3.11. Note, the data has been minimally processed, to prevent processing induced correlations presenting in the separated slice image time-series. The activation observed within the frontal lobe, which may be attributed to subject motion with respect to the flashing checkerboard stimulus. As demonstrated in Appendix A, aliased slice images separated with mSPECS are susceptible to artifacts from phase transitions despite efforts to calibrate the Hadamard aliased acquired time-series to the calibration time-series.

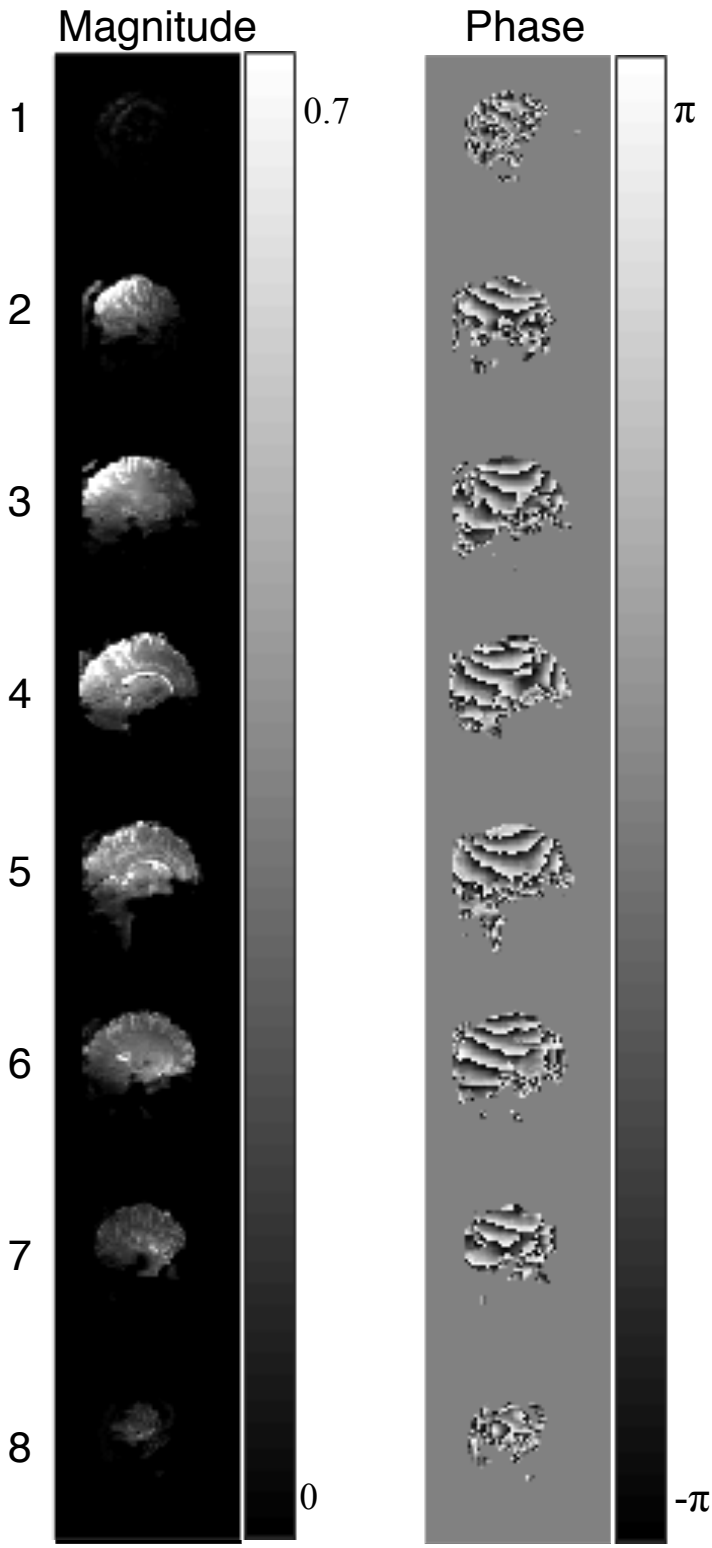


**Figure 3.8** Mean calibration magnitude slice images and phase slice images, with the numbering 1 through 8 referring to the slice image number.

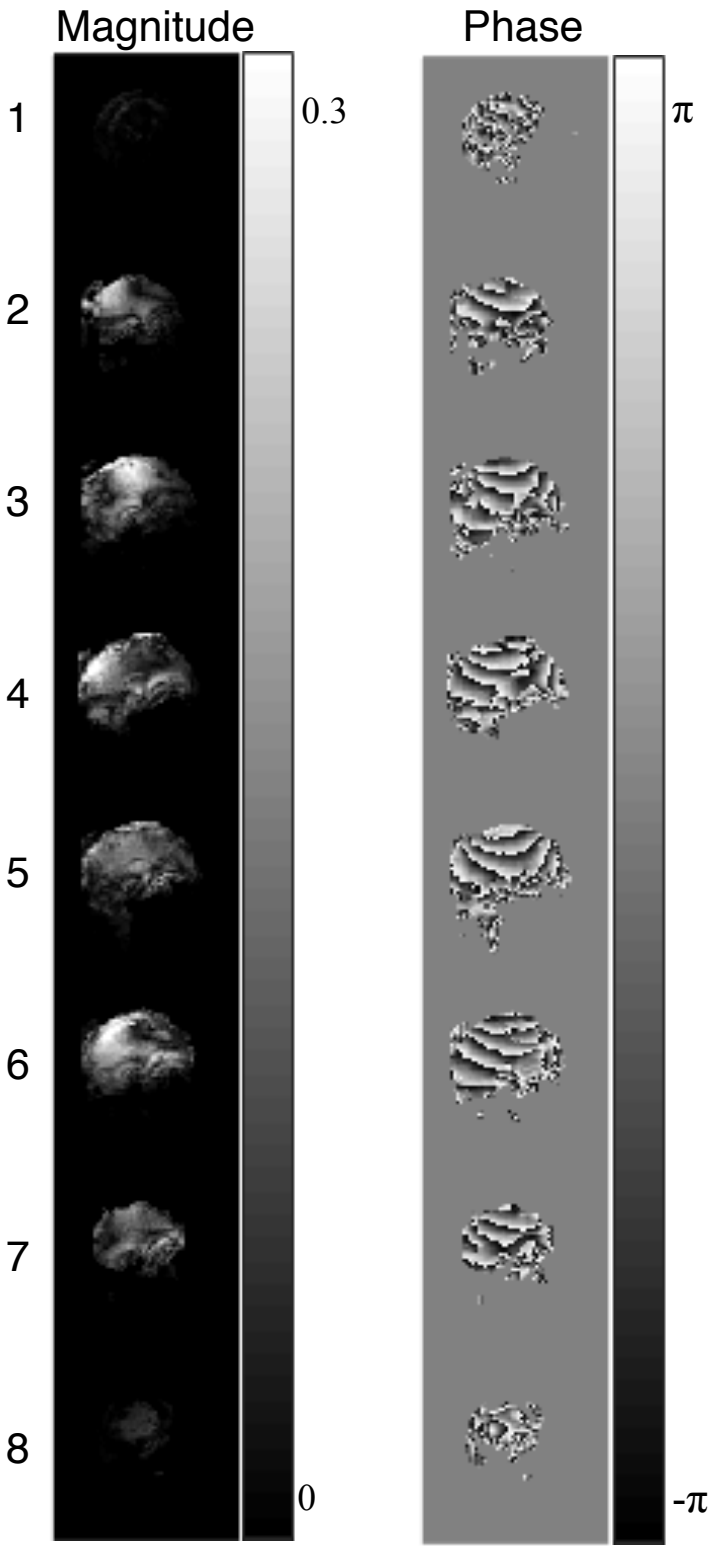


**Figure 3.9:** Mean Hadamard separated magnitude slice images and phase slice images, with the numbering 1 through 8 referring to the slice image number.

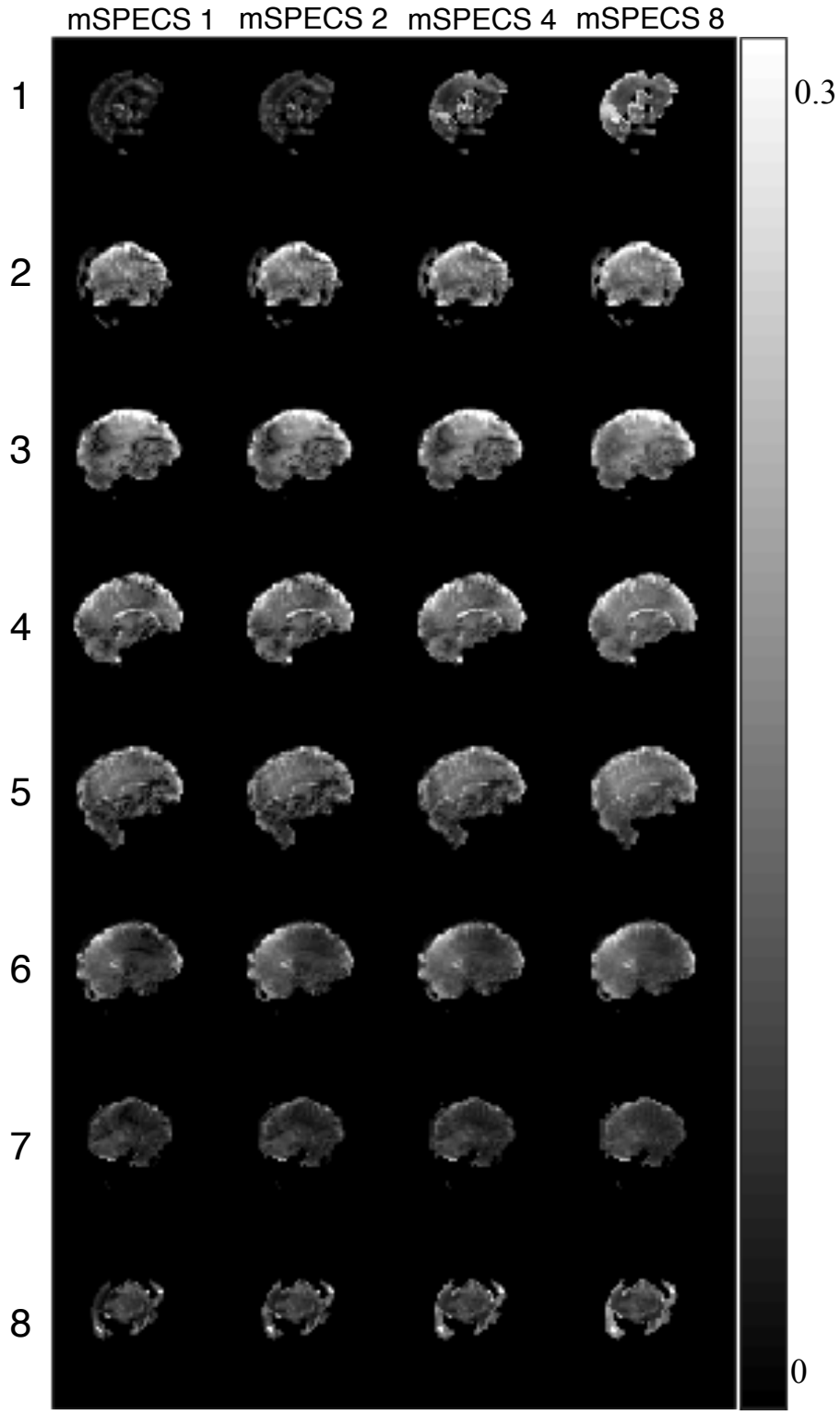


**Figure 3.10:** Mean magnitude mSPECS separated slice images from the Hadamard encoded human subject data for the accelerations of mSPECS 1, mSPECS 2, mSPECS 4, and mSPECS 8.

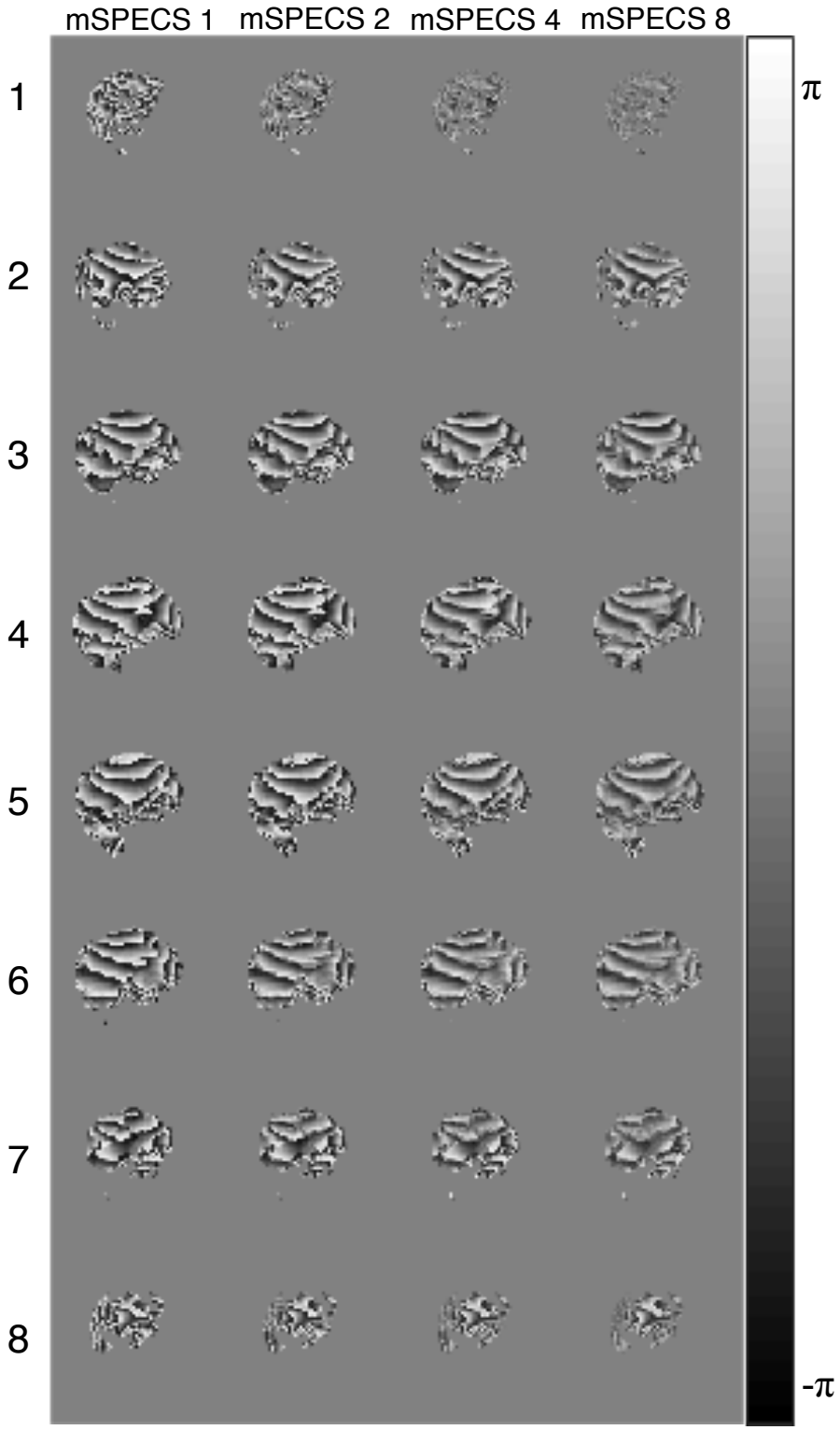


**Figure 3.11:** Mean phase mSPECS separated slice images from the Hadamard encoded human subject data for the accelerations of mSPECS 1, mSPECS 2, mSPECS 4, and mSPECS 8.

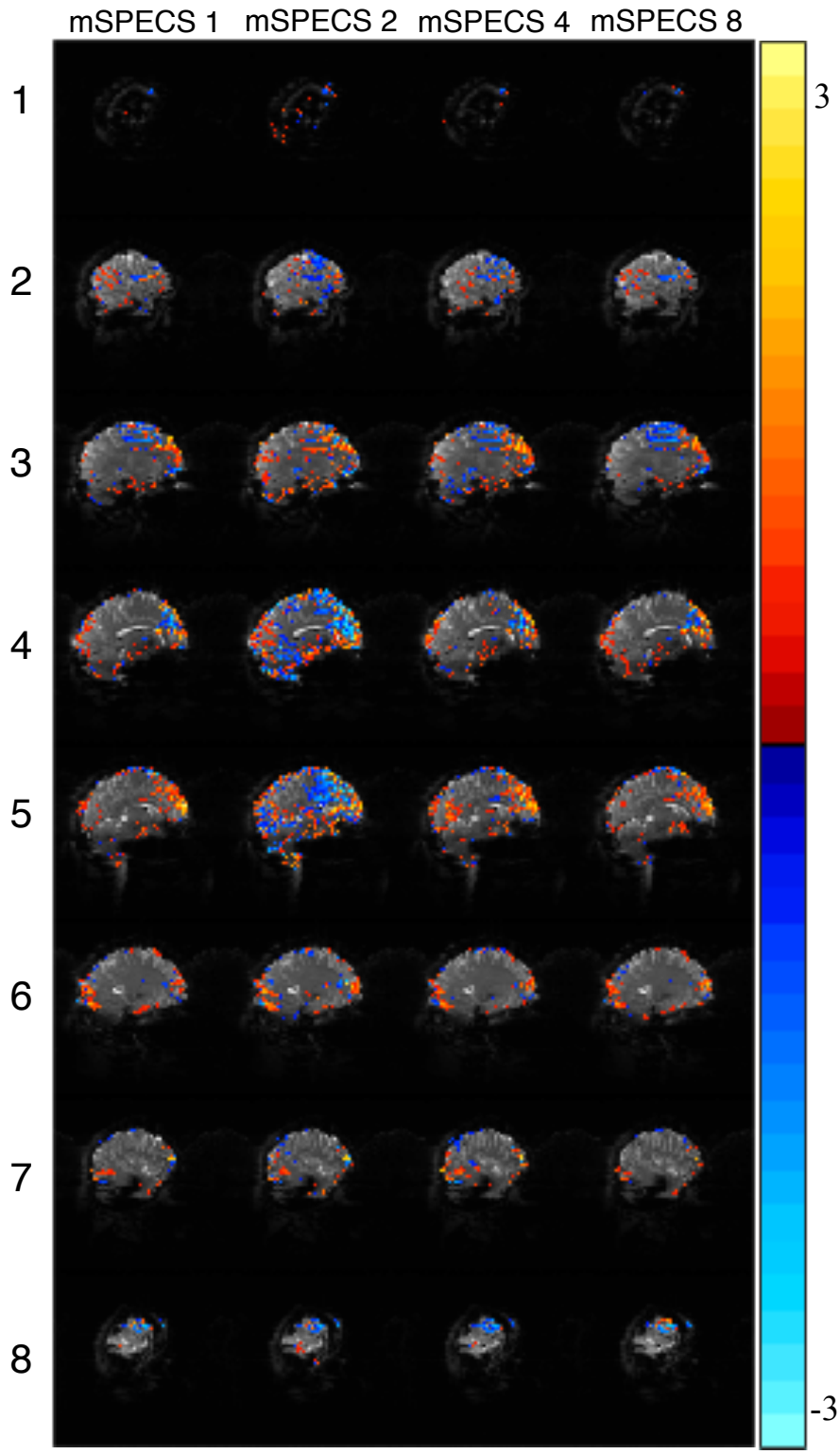


**Figure 3.12:** Activation statistics for the mSPECS separated slice images from the Hadamard encoded human subject data for the accelerations of mSPECS 1, mSPECS 2, mSPECS 4, and mSPECS 8.

### 3.5 Discussion

Without whole brain volume fMRI-SMS acquisitions and separation methods, either spatial or temporal resolution is constrained during experimental data acquisition. Although, many SMS reconstruction techniques ignore the statistical implications of fast imaging methods on the fMRI time-series analysis. The implementation of the mSPECS separation in simulation yields very promising results. In simulation, the activation in each slice is accurately placed and there is no task signal leakage between previously aliased voxels. Increasing the acceleration yields a higher sample size and improves the statistical significance of the data, so larger *z*-scores are observed as the acceleration increases, with the most substantial gains observed the *z*-scores between the reconstructions of mSPECS 1 and mSPECS 2.

The benefits of an implementation of the mSPECS separation in an acquisition of a Hadamard encoded fMRI time-series is less straightforward than observed in simulation. The quality of the mSPECS slice separation is dependent on the acquisition, and Hadamard addition and subtraction schemes are susceptible to signal dropout from subject motion or potentially from non-orthogonal phase encoding arising from magnetic field inhomogeneities. The mSPECS separated slice images from the human experimental data also present artifacts arising in the separated magnitude images from phase transitions between voxels as shown in simulation in Appendix A. Another potential draw back with mSPECS, as with any SMS reconstruction methods, is the potential for artifacts in the separated slice images, as a result of the motion between the calibration and Hadamard MB acquisitions. Despite the impact of phase wrapping in

mSPECS reconstruction, the development of complex-valued SMS reconstruction methods allows for increased statistical significance from a higher sampling rate of time points, and complex-valued fMRI analysis which has been shown to improve fMRI activation statistics.

# Chapter 4: mSPECS-IPA

## 4.1 Introduction

This chapter presents an SMS reconstruction method, a Multi-coil Separation of Parallel Encoded Complex-valued Slices with In-Plane Acceleration (mSPECS-IPA). This chapter builds on the mSPECS reconstruction model in the previous chapter, with an additional acceleration achieved with in-plane subsampling in the SMS-fMRI acquisition. In the absence of pMRI and SMS imaging methods, the temporal resolution of full volume high resolution images in fMRI are constrained by a long TR. As described in the previous chapter, higher sampling rates in fMRI are desirable to increase statistical power of the analysis allowing a faster observation of brain function and reduction of scan time. In fast imaging methods in fMRI, it is possible to subsample both in-plane and through-plane. Note, in this chapter, the MB factor refers to the number of aliased slice images acquired during acquisition, while $R$ refers to the number of rows omitted during the spatial frequency measurements, and the observed acceleration after the collapsed slice image separation and intra-slice unwrapping is the "net acceleration." Achieving an overall net acceleration of 8 by acquiring 8 aliased slices is not equivalent to acquiring 4 aliased sliced with an in-plane acceleration of $R$=2. The phrase "net acceleration" is used loosely in this chapter to refer to the aggregate subsampling in-plane and through-plane, as the scan time speed up observed from simultaneously exciting multiple slices is not equivalent to omitting the equivalent number of lines in $k$-space. Also, SMS methods do not suffer the SNR penalty observed with traditional pMRI methods, or in-plane

accelerations. In the Human Connectome Project, pilot studies evaluated additional in-plane subsampling with SMS acquisitions, and ultimately decided against in-plane subsampling and implemented an MB of 8, although recommended implementing an MB of 6 [Glasser et al., 2013; Ugurbil et al., 2013; Van Essen et al., 2013]. In addition to decreasing SNR, in-plane subsampling also reduces the acceptable number of aliased slices acquired during acquisition, and lower MB factors may lead to a long TRs.

A recent study comparing inter-slice signal leakage in commonly implemented SMS-fMRI EPI acquisition and reconstruction methods, conservatively recommended accelerations of both in-plane acceleration and through-plane accelerations equal to 2, for a net acceleration of 4. Increasing the through-plane acceleration factors to 3 or 4, for a net acceleration of 6 or 8, is recommended if the study design, imaging parameters, and reconstruction algorithms are optimized [Todd et al., 2015]. Without the optimization of these parameters, there is a risk of false activation in previously aliased voxel locations. The study also neglects to compare pure MB factors, i.e. no in-plane subsampling, to acquisitions with accelerations in both in-plane and through-plane.

In the theory section of this chapter, the mSPECS reconstruction method is extended to accommodate additional in-plane acceleration methods. The viability of mSPECS-IPA is shown in simulation, and an examination of the trade-off between in-plane and through-plane accelerations is presented. As with mSPECS, mSPECS-IPA reconstruction method implements a bootstrap sampling algorithm as a key component to mitigate inter-slice signal leakage. Although, the novelty of the mSPECS-IPA reconstruction is the two dimensional phase encoding method proposed in this section, so orthogonality is maintained between the voxels that are aliased both in-plane and through-plane. The

activation statistics for mSPECS and mSPECS-IPA are examined with a digital phantom and experimental human data simulation for various acceleration factors achieved with and without in-plane acceleration.

## 4.2 Theory

The Multi-coil Separation of Parallel Encoded Complex-valued Slices with In-Plane Acceleration (mSPECS-IPA) reconstruction method is a one-step process of aliased voxel separation, with both in-plane and through-plane acceleration, and coil image combination, as opposed to methods of separating the coil images for each slice image then combining the $n_C$ coil images into a single image. In this section, the notation from the mSPECS chapter is written to incorporate additional aliasing from in-plane subsampling.

### *Two-Dimensional Phase Encoding*

As with mSPECS, $H$, as constructed in Eq. [1.7], is the in-plane Hadamard aliasing matrix for an experiment with $n_S$ aliased slices, and is of dimension $n_S \times n_S$. The rotating in-plane Hadamard aliasing pattern, as used in mSPECS, is shown in Fig. 4.1a. Row $\delta$ and column $z$ of $H$ is denoted $H_{\delta,z}$ for the Hadamard aliasing pattern $\delta$, corresponding to a given TR, for slice $z$. With mSPECS-IPA there is an additional in-plane aliasing, as illustrated in Fig. 4.1b for an in-plane acceleration of 2 and 4, the in-plane Hadamard encodes are represented with

$M = (P_R H_R)'$,

where $H_R$ is derived as described in Eq. [1.7] and is of dimension $R \times R$.

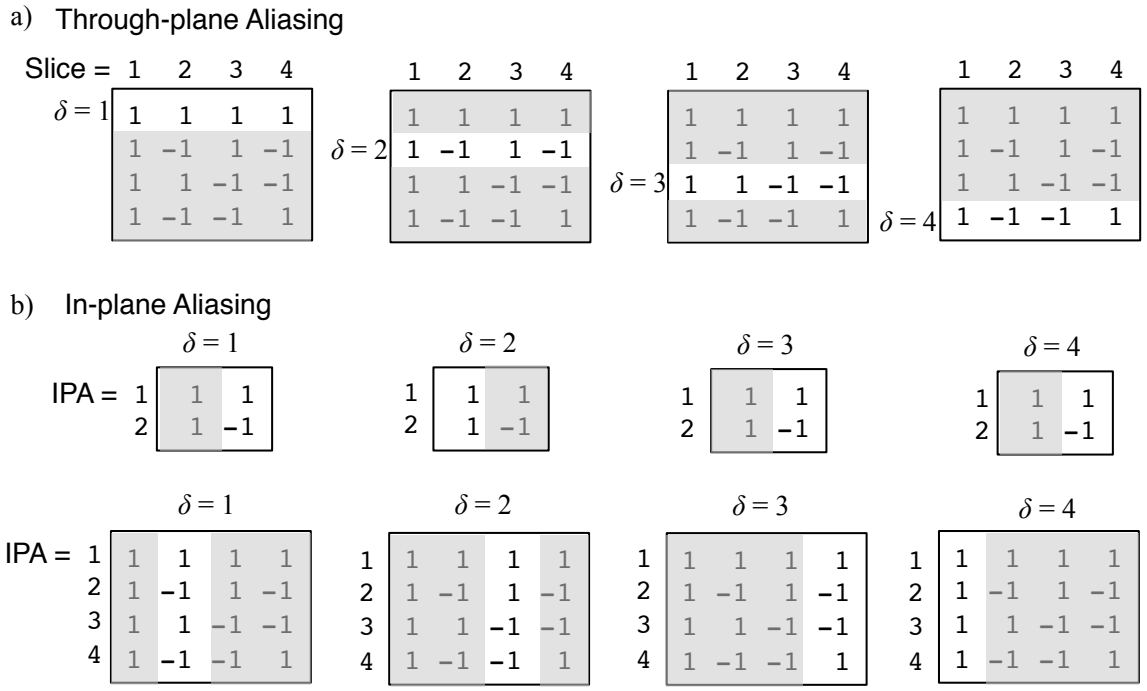


**Figure 4.1:** (a) The through slice plane aliasing pattern for MB4, with $\delta^{th}$ aliasing pattern in white and the artificial aliasing pattern shaded in gray (b) the in-plane aliasing pattern for IPA2 and IPA4, with $\delta^{th}$ aliasing pattern in white and the artificial aliasing pattern shaded in gray.

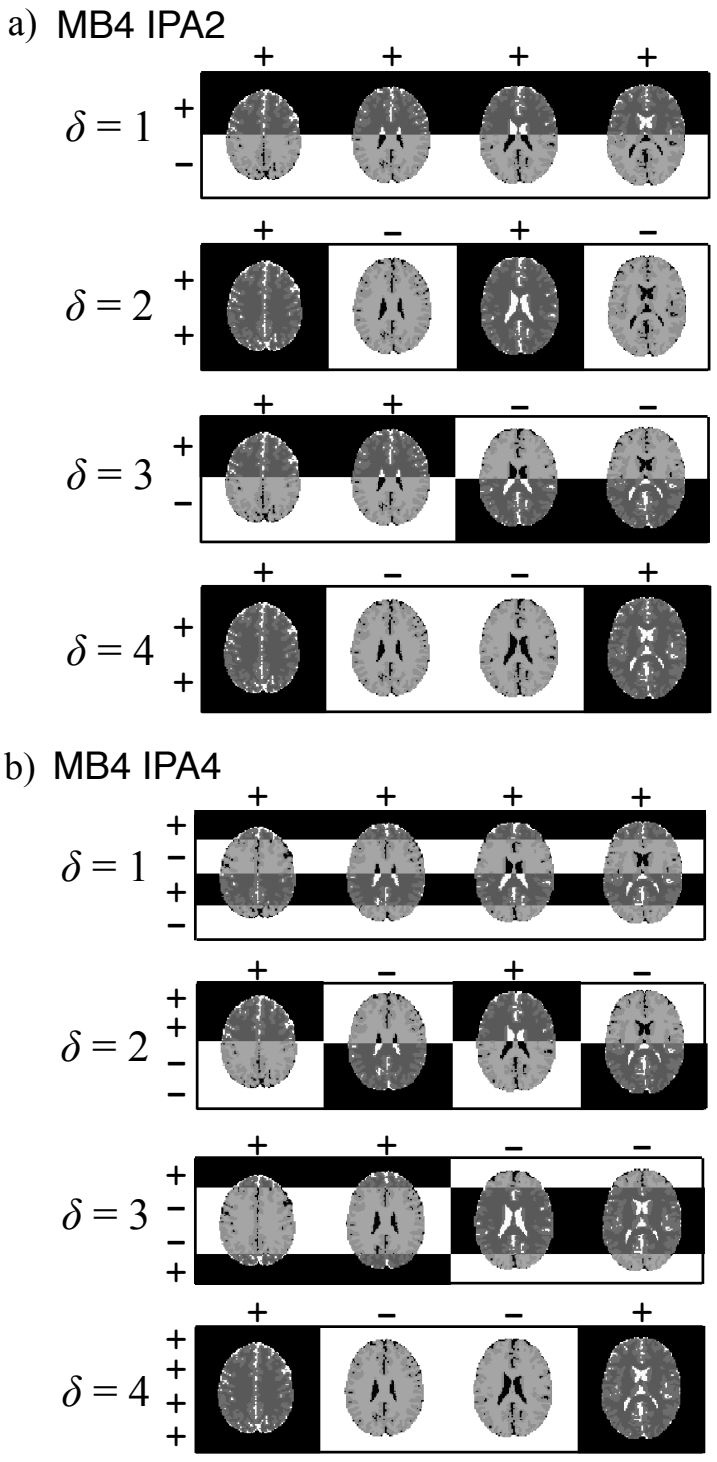


**Figure 4.2:** (a) Two-dimensional Hadamard aliasing pattern for $n_S$=4 aliased slices, with an in-plane acceleration of $R$=2, (b) two-dimensional Hadamard aliasing pattern for $n_S$=4 aliased slices, with an in-plane acceleration of $R$=4.

The matrix operation $P_R$ shifts rows one step

$P_R H_R = P_R(h_1,..,h_R)' = (h_R, h_1,\ldots, h_{R-1})'$,

the shift is required to maintain orthogonality with both the in-plane and through-plane aliasing patterns, as demonstrated in Fig. 4.1b where the in-plane encoding for the first aliasing pattern is the second Hadamard column. In Fig. 4.2a, the two-dimensional aliasing pattern is demonstrated for $n_S$=4 aliased slices, with an in-plane acceleration of $R$=2; in Fig. 4.2b, the two-dimensional aliasing pattern is demonstrated for $n_S$ = 4 aliased slices, with an in-plane acceleration of $R$=4. In the figure, the 1 or -1 across the top of slice images corresponds to the through-plane aliasing, and the 1 or -1 along the side of the slice images corresponds to the in-plane aliasing. The new aliasing matrix for the $\delta^{th}$ acquisition, $G_\delta$ of dimension $R \times n_S$, is constructed with the multiplication $\delta^{th}$ column, $m_\delta$, of the in-plane aliasing matrix, $M$, and $\delta^{th}$ row, $h_\delta$, of through-plane aliasing matrix, $H$,

$$G_\delta = m_\delta h_\delta. \quad [4.1]$$

When $R < \alpha$, which is often the case, and $M$ is of dimension $R \times R$, the number of acquisitions, or aliased slices, exceed the number of columns in $M$, so the in-plane aliasing pattern repeats such that $\delta$=$R$+1 corresponds to the first column in $M$.

Similar to Eq. [3.1] in mSPECS, a single aliased voxel, $a_{j,\delta}$, is aliased across $n_S$ slices through-plane, with an extra in-plane aliasing dimension of acceleration $R$. Fig. 4.3 is an illustration of the indexing of the aliased locations, Fig. 4.3a describes the reconstructed aliasing voxel locations for the subsampled $k$-space readout with an acceleration of $R$=2 for a single slice image. The three images are concatenated to illustrate the wrapping from failing to meet the Shannon-Nyquist sampling rate, and the acceleration of $R$ results in a reconstructed image of dimension $p_y/R \times p_x$, with the red dot

in the aliased image corresponding to the locations of the two blue dots in the fully sampled image. Fig. 4.3b and 4.3c describe the Hadamard aliasing locations in the mSPECS-IPA for the fourth acquisition as described in Fig. 4.1 and Fig. 4.2 in an example with $n_S$=4 aliased slices. The red dot in Fig. 4.3b is the acquired aliased voxel that is the Hadamard sum of voxel locations represented by the blue dots Fig. 4.3c.

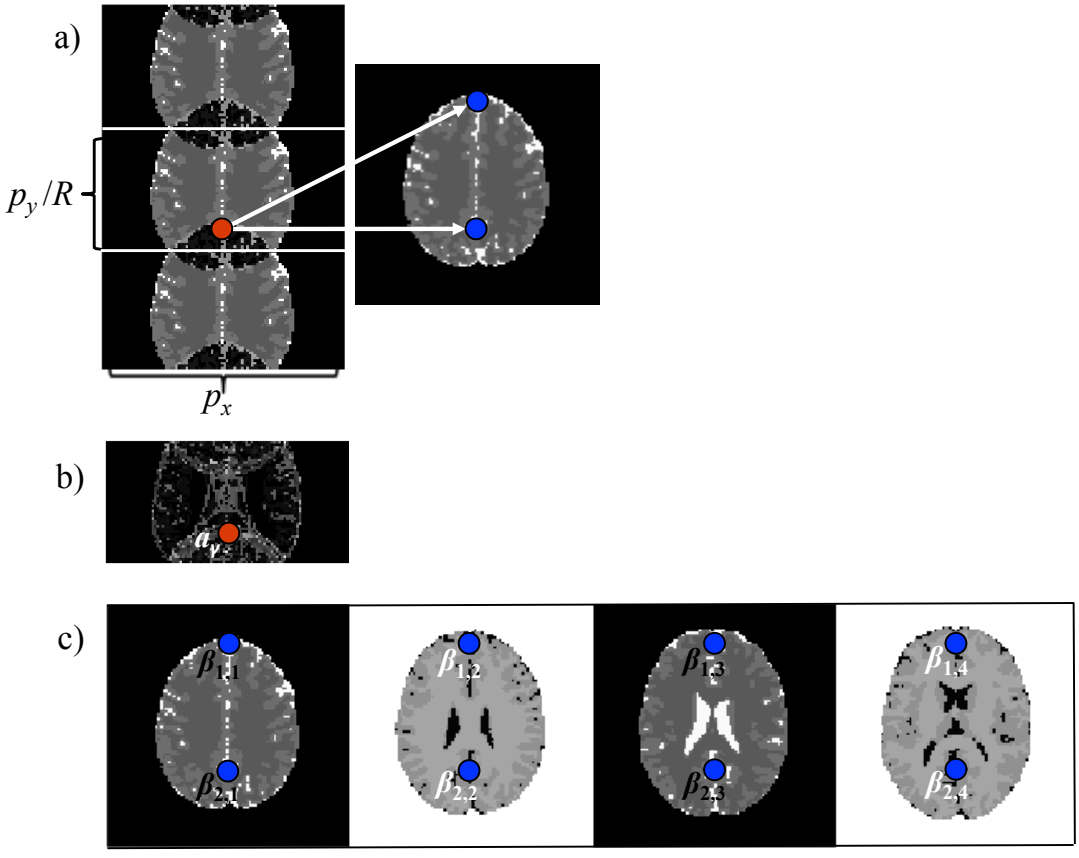


**Figure 4.3:** Aliased voxel locations are depicted for (a) Eq. [1.6] for an in-plane acceleration $R$=2, with arrows pointing to the un-aliased locations, (b) an in-plane acceleration, $R$=2, and through-plane acceleration, $n_S$ =4, as in Eq. [4.2], corresponding to the voxel locations in (c).

### *A Single Aliased Voxel*

In one packet, a single aliased voxel, $a_{j,\delta}$, in the same $(x,y)$ voxel location across $n_S$ slices, with the Hadamard encode $\delta$, measured at coil $j$, in image space is written as the summation

$$a_{j,\delta} = \sum_{m=1}^{R} \sum_{s=1}^{n_S} (G_\delta)_{m,s} (S_j)_{m,s} \beta_{m,s} + \varepsilon_j. \quad [4.2]$$

In Eq. [4.2], if $R$=1, then Eq. [4.2] is equivalent to Eq. [3.1] for a single aliased voxel in mSPECS. The 2×1 vector $a_{j,\delta}$ is written as the sum of the 2×1 vector $\beta_{q,z}$, the real and imaginary parts of the true voxel value $q$ in slice $z$, weighted by the 2×2 matrix of real and imaginary coil sensitivities at coil $j$. The $(G_\delta)_{q,z}$ value is either 1 or -1, and specific to value $q$ in slice $z$. The real and imaginary coil sensitivities $(S_j)_{q,z}$ correspond to the same voxel $q$ location as $\beta_{q,z}$ for slice $z$ at coil $j$, in a skew symmetric matrix,

$(S_j)_{x,z} = [S_R, -S_I; S_I, S_R]_{j,q,z}$.

The 2×1 vector $\varepsilon_j=(\varepsilon_{jR},\varepsilon_{jI})$ is the measurement error with real and imaginary parts at coil $j$ with a mean of $E(\varepsilon_j) = 0$ and covariance of $\text{cov}(\varepsilon_j) = \sigma^2 I_2$.

To separate the $n_S R$ aliased voxels, the goal is to estimate $\hat{\beta}$, the true separated voxel values from one packet. The number of sequential time-points, $n_\alpha$, where $n_\alpha$ is an integer between 1 and $n_S R$, is the number of sequential TRs in the Hadamard encoded acquisition included in the separation of a single separated aliased voxel at one time point. If the data is acquired in packets of $n_S$ aliased slices with an in-plane subsampling of $R$, the net acceleration of the slice image time-series acquisition is defined

$A = n_S R/n_\alpha$.

The measured aliased voxel in Eq. [4.2] is generalized across $n_C$ coils for $n_S R$ voxel locations with $n_\alpha$ sequential time-points included in the separation, as

$$a = X_A\beta+\varepsilon. \quad [4.3]$$

In Eq. [4.5], $a$ and $\varepsilon$ are of dimension $2n_C n_\alpha \times 1$, and the error vector, $\varepsilon$, has the mean of

$E(\varepsilon) = 0$,

and a covariance of

$$\text{cov}(\varepsilon) = \sigma^2 I_{2n_C n_\alpha}, \quad [4.4]$$

$X_A$ is of dimension $2n_\alpha n_C \times 2n_S R$, and $\beta$ is of dimension $2n_S R \times 1$, so $n_S$ and $R$ correspond to the through-plane aliasing and in-plane aliasing dimensions, respectively. The sensitivity aliasing matrix, $X_A$, is the coil sensitivities multiplied by the Hadamard 1 or -1 coefficient, so for the Hadamard aliasing pattern $\delta$, and the real-valued $n_C$ coil sensitivities for voxel $q$ in slice $z$ are represented in

$$\lambda_{q,z} = ([S_1, \ldots, S_{n_C}]')_{q,z}$$

of dimension $2n_C \times 2$, so

$$(X_A)_\delta = \left[(G_\delta)_{1,1}\lambda_{1,1}, \ldots, (G_\delta)_{1,n_S}\lambda_{1,n_S}, \ldots, (G_\delta)_{R,1}\lambda_{R,1}, \ldots, (G_\delta)_{R,n_S}\lambda_{R,n_S}\right].$$

This is generalized to $X_A$, of dimension $2n_\alpha n_C \times 2n_S R$, for the incorporation of $n_\alpha$ sequential TRs in the aliased voxel separation,

$$X_A = [(X_A)_1, \ldots, (X_A)_{n_\alpha}]'. \quad [4.5]$$

Similar to previous efforts to reconstruct images with lines of *k*-space omitted during image acquisition [Pruessmann et al., 1999], disentangling simultaneously excited slices with coil sensitivities [Larkman et al., 2001], with an additional phase manipulation [Muller et al., 1988; Souza et al., 1988], the $2n_S R \times 1$ vector of separated voxel values, $\hat{\beta}$, can be estimated,

$\hat{\beta} = (X'_A X_A)^{-1} X'_A a,$

with a covariance between the previously aliased voxels across the $n_S$ slices,

$$\mathrm{cov}(\hat{\beta}) = \sigma^2 (X_A' X_A)^{-1}. \quad [4.6]$$

To reduce the covariance between previously aliased voxels and improve the aliased voxel separation, and thus minimize correlation induced from the aliased voxel separation process, the mSPECS-IPA method combines the coil encoding and a two dimensional Hadamard phase encoding, with calibration images into the least squares estimation. The novelty of the mSPECS-IPA reconstruction is the two dimensional Hadamard phase encoding, in addition to the bootstrapping sampling and artificial aliasing of calibration voxel values. The mechanism of incorporating calibration slice images in the SMS-fMRI reconstruction, mitigates inter-slice signal leakage, which may present as "clusters" of false activation, between previously aliased voxel regions, as a result of correlation induced during aliased voxel separation.

***Bootstrap Sampling and Artificial Aliasing***

In the mSPECS-IPA reconstruction model, calibration images are artificially aliased with the two-dimensional aliasing patterns, shown in Fig. 4.1 and Fig. 4.2, to achieve higher accelerations in post acquisition image separation. To separate an aliased coil slice image, $n_S R$ bootstrap sampled coil slice images from the fully-sampled calibration slice image time-series are averaged, then artificially aliased. This mean bootstrap sampling and artificial aliasing algorithm is repeated for each time-point in the aliased slice image time-series. For a single time-point, a voxel in the same $(x,y)$ location

across the $n_S R$ voxels measured at $n_C$ coils, bootstrap sampled from the calibration time-series, is represented in the $2n_C n_S R \times 1$ vector, $\nu$, and the mean sample for each time point is represented in the $2n_C n_S R \times 1$ vector, $\bar{\nu}$. The true mean voxel values of the mean calibration images, $\bar{\nu}$, to be aliased in the same $n_S R$ voxel locations, are represented by the $2n_S R \times 1$ vector $\mu$, with the same voxel indices as in $\beta$ for Eq. [4.3]. The vector, $\nu$, has a $2n_C n_S R \times 1$ error vector, $\eta$, with $\eta=(\eta_R,\eta_I)$ corresponding to the real and imaginary parts of the measurement error of the coil calibration slice images for $n_S R$ voxels measured at $n_C$ coils. The calibration slice coil images measurement error has a mean of

$E(\eta)=0$,

and a covariance of

$\text{cov}(\eta)=\sigma^2 I_{2n_C n_S R}$.

In the mSPECS-IPA model, for the $\delta^{\text{th}}$ aliased pattern, in the aliased voxel separation in Eq. [4.3], the mean calibration images, $\bar{\nu}$, are artificially aliased with the $2n_\alpha n_C(n_S\text{-}1)\times 2n_S n_C R$ aliasing matrix $C_\delta$, is the Kronecker product of the +1 and -1 Hadamard coefficients and vectors of ones, is

$C_\delta = \mathbf{1}_{n_C} \otimes [(\bar{G}_\delta)_{1,1} \otimes \mathbf{1}_2,\ldots, (\bar{G}_\delta)_{1,n_S} \otimes \mathbf{1}_2,\ldots, (\bar{G}_\delta)_{R,1} \otimes \mathbf{1}_2,\ldots, (\bar{G}_\delta)_{R,n_S} \otimes \mathbf{1}_2]$.

The $(n_S\text{-}1)R \times n_S R$ matrix $\bar{G}_\delta$ is the remaining $(n_S\text{-}1)R \times n_S R$ with the $\delta^{\text{th}}$ acquisition removed from the $G$ matrix, so that $C_\delta$ is the remaining $(n_S\text{-}1)$ orthogonal ways the true fully acquired voxels across the $n_S$ slices could be aliased with a Hadamard matrix. An illustration of the origin of $\bar{G}_\delta$ to create the potential aliasing matrices, $C_\delta$, for the $n_S R$ aliasing patterns, is shown in Fig. 4.4 for a Hadamard encoded time-series with $n_S$=4 aliased slice images with an in-plane acceleration of $R$=2, also written as mSPECS 4 – IPA 2. Fig. 4.4a is the time-series through-plane aliasing pattern that repeats every $n_S$

TRs, and Fig 4.4b is the time-series in-plane aliasing pattern that repeats every $R$ TRs. Fig. 4.4c and Fig. 4.4d depict the artificial aliasing matrices for mSPECS 4 – IPA 2 for the $\delta^{th}$ aliasing pattern equivalent to the $\delta^{th}$ row of a Hadamard matrix of dimension $n_S \times n_S$ where $\delta = 1 \ldots n_S$, and the gray shaded region designated the $n_S$-1 ways to artificially alias the calibration slice images corresponding to the $\delta^{th}$ aliasing pattern, and $q$ corresponds to the in-plane aliasing pattern such that $q = 1 \ldots R$.

To incorporate $n_\alpha$ subsequent TRs from the aliased voxel acquisition, the corresponding aliasing matrices, $C_\delta$, are placed along a the diagonal to create a single aliasing matrix $C$, of dimension $2n_C n_\alpha(n_S\text{-}1) \times 2n_S n_C n_\alpha R$,

$$C = \begin{bmatrix} C_1 & & 0 \\ & \ddots & \\ 0 & & C_{n_\alpha} \end{bmatrix} \quad [4.7]$$

Artificially aliasing the mean bootstrap sampled voxels, $\bar{v}$, and the corresponding error vector, $\eta$, from the calibration images with the aliasing matrix in Eq. [4.7] results in a $2n_\alpha n_C(n_S\text{-}1)R \times 1$ vector,

$$\upsilon = C\bar{v} = C_A\mu + C\eta, \quad [4.8]$$

where $\mu$ has been previously defined as the $2n_S R \times 1$ vector of the true calibration voxel values with real and imaginary parts. The matrix $C_A$ is a coil sensitivity matrix with Hadamard coefficients, analogous to $(X_A)_\delta$, for the artificially aliased calibration voxels is the $2n_C(n_S\text{-}1) \times 2n_S R$ matrix,

$$(C_A)_\delta = \left[(\bar{G}_\gamma)_{1,1} \otimes \lambda_{1,1}, \ldots, (\bar{G}_\gamma)_{1,n_S} \otimes \lambda_{1,n_S}, \ldots, (\bar{G}_\gamma)_{R,1} \otimes \lambda_{R,1}, \ldots, (\bar{G}_\gamma)_{R,n_S} \otimes \lambda_{R,n_S}\right].$$

Similar to Eq. [4.5], $(C_A)_\delta$ is generalized to $C_A$, of dimension $2n_\alpha n_C(n_S\text{-}1) \times 2n_S R$, for the incorporation of $n_\alpha$ sequential TRs in the aliased voxel separation,

$$C_A = [(C_A)_1, \ldots, (C_A)_{n_\alpha}]'.$$

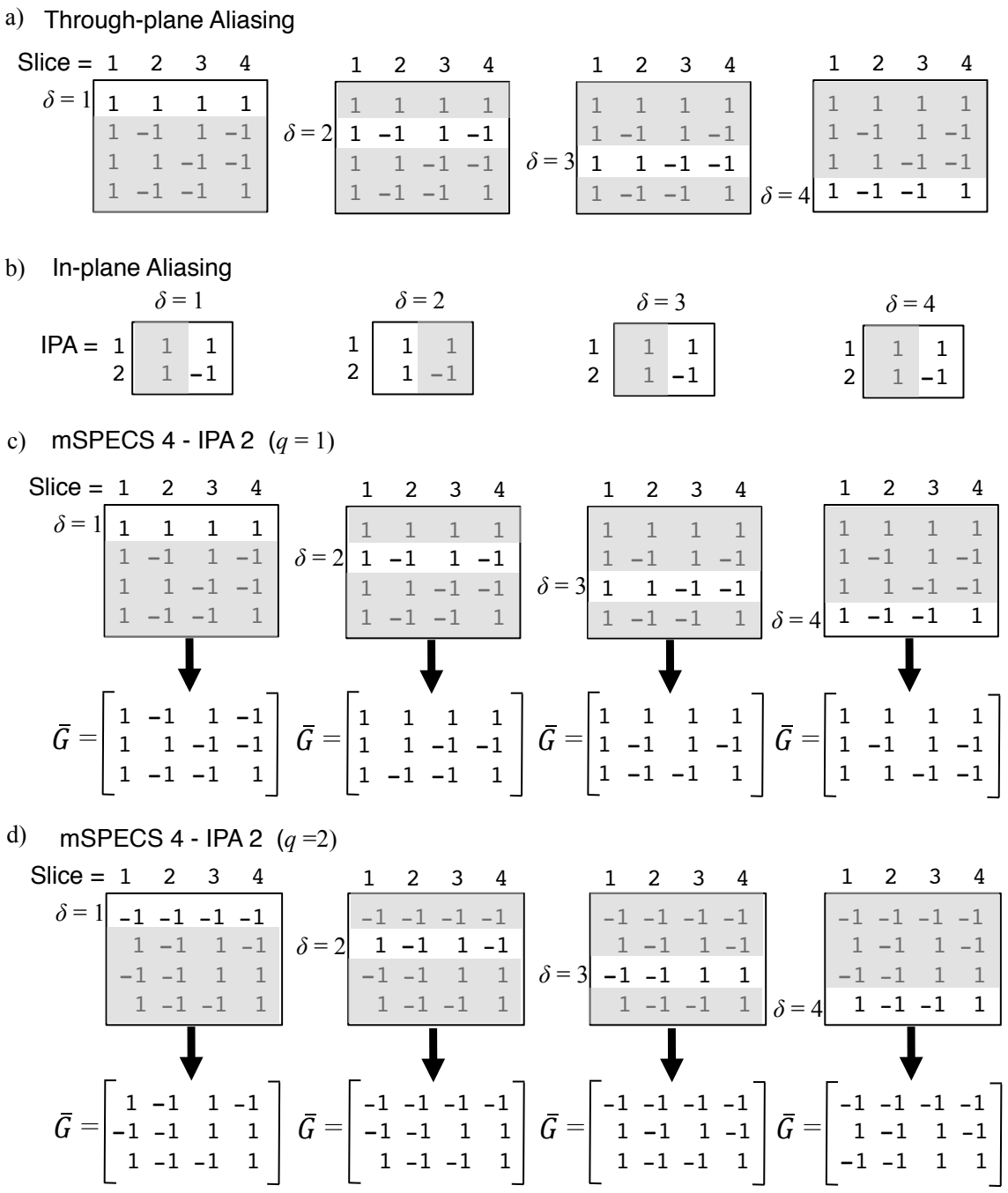


**Figure 4.4** (a) The through slice plane aliasing pattern for MB4, with $\delta^{th}$ aliasing pattern in white and the artificial aliasing pattern shaded in gray (b) the in-plane aliasing pattern for IPA2, with $\delta^{th}$ aliasing pattern in white and the artificial aliasing pattern shaded in gray, (c) the corresponding artificial aliasing matrices, $\bar{G}$, for the $\delta^{th}$ aliasing pattern for the in-plane aliasing pattern $q$=1, and (d) the corresponding artificial aliasing matrices, $\bar{G}$, for the $\delta^{th}$ aliasing pattern for the in-plane aliasing pattern $q$=2.

***A Separation of Aliased Voxel Values***

With the mSPECS approach, to separate the aliased voxel values, Eq. [4.3] and Eq. [4.8] are concatenated into one equation,

$$\begin{bmatrix} a \\ \upsilon \end{bmatrix} = \begin{bmatrix} X_A\beta \\ C_A\mu \end{bmatrix} + \begin{bmatrix} \varepsilon \\ C\eta \end{bmatrix}. \quad [4.9]$$

If $y_a$ is the $2n_\alpha n_C n_S R \times 1$ vector of acquired aliased voxel values stacked over the artificially aliased voxel values such that $y_a = (a', \upsilon')'$, and $X$ is the two aliasing matrices concatenated, $X=[X_A', C_A']'$ of dimension $2n_\alpha n_S n_C \times 2n_S R$, then the separation of the aliased voxel values in Eq. [4.9] is a least squares estimate of the form

$\hat{\beta} = (X'X)^{-1}X'y_a$,

The $2n_S R \times 1$ vector of estimated separated voxel values with real and imaginary parts, is also written

$\hat{\beta} = (X'_A X_A + C'_A C_A)^{-1}(X'_A a + C'_A \upsilon)$

To view the mSPECS-IPA approach as a Bayesian method, where $a \sim N(\beta, \sigma^2 I_{2n_c n_\alpha})$ and

$\bar{\nu} \sim N(\mu, \sigma^2 I_{2n_c n_\alpha n_{sR}})$, so the posterior mean is

$E[\hat{\beta}] = (X'_A X_A + C'_A C_A)^{-1}(X'_A \beta + C'_A \mu)$,

such that the separated voxel values are a weighted combination of prior and likelihood mean voxel values, or calibration and artificially aliased voxel values.

The covariance of the added measurement error of a measured aliased voxel in Eq. [4.3] measured at $n_C$ coils, with is $n_\alpha$ sequential TRs incorporated into mSPECS,

$$\text{cov}(\varepsilon) = \sigma^2 I_{2n_c n_\alpha} \quad [4.10]$$

and the covariance of the artificially aliased $n_S$ calibration voxel values measured at $n_C$ coils, with is $n_\alpha$ sequential TRs in Eq. [4.9] is

$$\text{cov}(C\eta)=\sigma^2 I_{2n_C n_\alpha (n_S-1)R}. \quad [4.11]$$

In both Eq. [4.10] and Eq. [4.11], there is no covariance between the real and imaginary parts, and a constant variance of $\sigma^2$ for both real and imaginary parts. The $2n_\alpha n_C n_S R \times 2n_\alpha n_C n_S R$ covariance matrix for the $2n_\alpha n_C n_S R \times 1$ vector $y_a$, consisting of aliased and artificially aliased voxel values is

$$\text{cov}(y_a)=\begin{bmatrix} \sigma^2 I_{2n_\alpha n_C} & 0 \\ 0 & \tau^2 I_{2n_\alpha n_C (n_S-1)R} \end{bmatrix}. \quad [4.12]$$

If there is no variation, i.e. no random sampling of the calibration voxel values with mSPECS-IPA, among the average calibration slice images used to separate each aliased image then $\tau^2=0$. The bootstrapping adaptation averages $n_S R$ randomly selected calibration images for each TR in $\bar{v}_j$ to obtain $\tau^2=\sigma^2$, such that the covariance in Eq. [4.12] results in the $2n_S R \times 2n_S R$ matrix,

$$\text{cov}(\hat{\beta})=\sigma^2 (X_A' X_A + C_A' C_A)^{-1}.$$

The inclusion of the calibration images through the mSPECS-IPA method reduces correlation between the previously voxel values, both in-plane and through-plane, since $C_A' C_A$ acts as a regularizer. In SMS-fMRI, induced correlation from the un-aliasing of the slice images throughout the time-series, presents as inter-slice signal leakage among previously aliased voxels, with false activation detected in these regions.

## 4.3 Methods

The mSPECS-IPA method is demonstrated with a MATLAB digital phantom simulation and an experimental human data simulation. With Hadamard matrix dimensions increasing in powers of two, the design of task timings must also increase in powers of two to accommodate various accelerations determined post acquisition, by varying $n_\alpha$ in the mSPECS-IPA method. In this section, various in-plane and through-plane accelerations are also examined as described in Table 4.1, with the IPA and MB parameters. In the six scenarios, the following through-plane aliasing is examined- an acquisition of 8 aliased slice images, for an MB8, with 8 aliased slices acquired in a single packet, an acquisition of 4 aliased slice images, for an MB4, with 4 aliased slices acquired in two packets where the first packet contains slices 1, 3, 5, and 7, and the second packet contains slices 2, 4, 6, and 8, an acquisition of 2 aliased slice images, for an MB2, with 2 aliased slice images acquired in four packets where the first packet contains slices 1 and 5, the second packet contains slices 2 and 6, the third packet contains slices 3 and 7, and the fourth packet contains slices 4 and 8. The three through-plane accelerations, MB2, MB4, and MB8, are simulated with no in-plane acceleration, IPA1, and with an in-plane acceleration of 2, IPA2, with the subsequent net accelerations written in Table 4.1. Note, in the theory section of this chapter, $n_S$ denotes the number of aliased slices or MB factor, and $R$ is the in-plane acceleration or IPA, which is the number of rows omitted in $k$-space. Only an in-plane acceleration of 2 is demonstrated, as an in-plane acceleration of 4 is not feasible in fMRI studies since the echo time is too

short for BOLD contrast, and an in-plane acceleration of 3 will not maintain the orthogonality of the 2-dimensional Hadamard encoding.

| Scenario | IPA | MB | Net acceleration |
|---|---|---|---|
| **1** | 2 | 8 | 16 |
| **2** | 2 | 4 | 8 |
| **3** | 2 | 2 | 4 |
| **4** | 1 | 8 | 8 |
| **5** | 1 | 4 | 4 |
| **6** | 1 | 2 | 2 |

**Table 4.1:** Scenarios examined for varying accelerations in mSPECS(-IPA).

The timings for the mSPECS-IPA reconstructions are described in Table 4.2, similar to the notation in the previous section, "mSPECS 4 – IPA 2" denotes an mSPECS-IPA reconstruction with a through-plane acceleration of 4 and an in-plane acceleration of 2. Although the mSPECS 2 – IPA 1 and mSPECS 4 – IPA 1, are different reconstructions than the mSPECS 2 and mSPECS 4 in the previous chapter, since an MB of 2 and 4 is used, rather than MB8. The simulations generated for the six scenarios are acquired over the same length of time, 672 seconds. Increasing the net acceleration factor corresponds to a higher sampling rate. An acceleration of 8 corresponds to a TR of 1 second. This is chosen as the baseline TR, since the goal of the mSPECS(-IPA) reconstruction methods is to implement in whole volume fMRI and acquire multiple packets within the TR. With a 1 second TR, 8 other packets with 8 aliased slices within each packet, yield a total of 72 slices acquired. An MB of 8 was achieved with the human connectome project, although implementing an MB of 6 is recommended from the human

connectome researchers [Glasser et al., 2013; Ugurbil et al., 2013; Van Essen et al., 2013].

| Reconstruction | IPA | MB | $n_{pack}$ | TR | TRs |
|---|---|---|---|---|---|
| mSPECS 2 – IPA 1 | 1 | 2 | 4 | 4 s | 84 |
| mSPECS 4 – IPA 1 | 1 | 4 | 2 | 2 s | 168 |
| mSPECS 8 – IPA 1 | 1 | 8 | 1 | 1 s | 336 |
| mSPECS 2 – IPA 2 | 2 | 2 | 4 | 2 s | 168 |
| mSPECS 4 – IPA 2 | 2 | 4 | 2 | 1 s | 336 |
| mSPECS 8 – IPA 2 | 2 | 8 | 1 | 0.5 s | 672 |

**Table 4.2:** Scenarios examined for varying accelerations in mSPECS(-IPA).

The coil sensitivity maps in this chapter, for both the digital phantom simulation and human data simulation, were generated with a bivariate normal probability density function, and the first 4 coils are placed in the four corners and the next 4 coils on the four edges, then repeated for a total of 16 receive coils. Sixteen weighting matrices, with values between 0 and 1, are generated, rotated for each slice, and applied to the coil profiles, such that each slice has a unique weighting of the 16-channel coil profiles. For the complex-valued coil profiles, a phase of $\pi/12$ is added to each coil profile.

### 4.3.1 Digital Phantom Simulation

A fMRI digital phantom data set was generated with a block-design of task activity, with an initial rest of 16 second rest followed by 21 epochs of 16 seconds on and 16 seconds using MATLAB (The Mathworks, Natick, MA, USA). The data was generated for eight axial slice images that are 96×96 in dimension to represent one packet

in a full brain volume Hadamard encoded acquisition. The noiseless time series was generated for each slice with a theoretical $T_2^*$ weighted phantom similar to [Karaman et al., 2016]. The initial $T_2^*$ weighted phantom has initial values between 0 and 1, then weighted for maximum SNR of 30 in the magnitude, yielding an approximate SNR of 30 in the CSF, 15 in the grey matter, and 7 in the white matter, and a mean phase is added to the slice images varied from $8\pi/36$ to $\pi/36$ from slice one to slice eight decreasing in increments of $\pi/36$. The SNR and CNR valued in the digital phantom simulation are based of the human subject data used in the experimental simulation. A calibration time-series was generated with 45 TRs from the complex-valued phantom. The slices are first weighted by the simulated complex-valued 16-channel coil sensitivities. Then standard Gaussian noise was added to the real and imaginary components of the time series.

In the simulation, the task was generated in one unique 6×6 voxel square region of interest (ROI) rotating clockwise for each slice with a magnitude CNR of 0.5, as defined in Eq. [2.9]. For a magnitude CNR of 0.5, the magnitude within the ROI is increased by 0.5 for 16 TRs and then returning to baseline for the following 16 TRs. Before the complex-valued time-series was summed in the slice direction, the Hadamard phase encoding was simulated. With no in-plane acceleration, i.e. mSPECS, the rotating Hadamard pattern resembled Fig. 1.4, depending on the number of aliased slices or multiband factor. Once the complex-valued slices are multiplied by +/- Hadamard phase encode, they were weighted by the complex-valued 16-channel coil sensitivities, then summed in the slice direction. Standard Gaussian noise was added to the real and imaginary components of the time series. For the scenarios with in-plane acceleration, or IPA 2, the rotating Hadamard pattern for the slice encoding resembled Fig. 4.1,

depending on the number of aliased slices or multiband factor. After the phase encoding, the slice images are Fourier transformed to *k*-space, every other line is deleted to simulate in an in-plane acceleration of $R$=2, and the spatial frequencies are inverse Fourier transformed back to image space. The new images are now of dimension 96/$R$×96, or 48×96.

The main goal of the mSPECS(-IPA) reconstructions is faster observation of brain function, to illustrate this mechanism time-series of the six scenarios outlined in Table 4.1, mSPECS 2 – IPA 1, mSPECS 4 – IPA 1, mSPECS 8 – IPA 1, mSPECS 2 – IPA 2, mSPECS 4 – IPA 2, mSPECS 8 – IPA 2, for net accelerations of 2, 4, 8, 4, 8, and 16, respectively. In each scenario, the time-series is 672 seconds, although the number of TRs varies depending on the acceleration, as the net acceleration factors increase, a higher the sampling rate is achieved. The aliased slice time-series images were then separated using the mSPECS(-IPA) separation method, and the fMRI activation was calculated in each separated voxel using the complex-valued fMRI model in [Rowe et al., 2005b]. To evaluate the mSPECS(-IPA) separation, the separated time-series is compared to the original, with the activation statistics are further examined at each acceleration, by plotting the *z*-statistic, to demonstrate the power of high MB factors in fMRI analysis.

### 4.3.2 Human Subject Data Simulation

An experimental fMRI human data set was acquired with bilateral finger tapping in a block design with an initial 16 s rest followed by 22 epochs of 16 s on and 16 s off using a 3.0 T Discovery MR750 MRI scanner (General Electric, Milwaukee, WI) with a

GE single channel quadrature head coil. The data was acquired with ten interleaved axial slices that are 96×96 in dimension and 4 mm thick. The two most inferior slices were omitted so that there were eight slice images, for simulation up to MB8, utilized in the experimental human data simulation. The imaging parameters included a 24.0 cm FOV, a TR/TE of 1000/39 ms, a flip angle of 25°, an acquisition bandwidth of 111 kHz, and an effective echo spacing of 0.672 ms. The phase encoding direction was oriented as posterior to anterior (bottom to top in images). Images were Nyquist ghost corrected using the three navigator echoes method [Nencka et al., 2009] and dynamic B0 field corrected using the TOAST single echo technique [Hahn et al., 2009]. Over the course of 22 epochs, a bilateral finger tapping experiment was performed in a block-design, and the SNR was determined, using Eq. [2.9] and Eq. [2.10] to be about 50 in the gray matter and 20 in the white matter and magnitude CNR was approximately 1, which were incorporated for the previous simulation. The starting mean magnitude for the slice images is shown in Fig. 4.20. The complex-valued activation statistics [Rowe, 2005b], smoothed with a Gaussian kernel with a FWHM of 3, for the original time-series is also shown in Fig. 4.20.

Before implementing mSPECS-IPA, a phase correction is applied to the phase time-series for the calibration time-series and aliased time-series. This phase correction applied is similar to the method described in the single-coil version of the mSPECS(-IPA) separation, SPECS [Rowe et al., 2016]. First, the angular phase mean of the time-series is estimated and removed for each voxel time-series. The resultant difference of the voxel time-series was fit to a local second order polynomial a local fit region of 11×11 voxels, then the polynomial fitted difference phase is added to a mean phase for each

slice. The first 3 time point in for each slice time-series were deleted, and the next 45 time repetitions are set as the calibration complex-valued time-series, leaving the remaining 672 time repetitions for the Hadamard aliased time-series simulation. The calibration images are weighted by the complex-valued 16-channel coil sensitivities.

As with the digital phantom simulation, to generate the aliased functional time-series, the Hadamard phase encoding was simulated based on the acquisition, as well as the number of aliased slices and the in-plane acceleration. With no in-plane acceleration, i.e. mSPECS, the rotating Hadamard pattern resembled Fig. 1.4, depending on the number of aliased slices or multiband factor. Once the complex-valued slices are multiplied by +/- Hadamard phase encode, they were weighted by the complex-valued 16-channel coil sensitivities, then summed in the slice direction. Standard Gaussian noise was added to the real and imaginary components of the time series. For the scenarios with in-plane acceleration, the rotating Hadamard pattern for the slice encoding resembled Fig. 4.1, depending on the number of aliased slices or multiband factor. After the phase encoding, the slice images are Fourier transformed to *k*-space line, every other line is deleted to simulate in an in-plane acceleration of $R$=2, and the spatial frequencies are inverse Fourier transformed back to image space. The new images are now of dimension $96/R \times 96$, or $48 \times 96$.

The main goal of the mSPECS(-IPA) reconstructions is faster observation of brain function, to illustrate this mechanism time-series of the six scenarios outlined in Table 4.2, mSPECS 2 – IPA 1, mSPECS 4 – IPA 1, mSPECS 8 – IPA 1, mSPECS 2 – IPA 2, mSPECS 4 – IPA 2, mSPECS 8 – IPA 2, for net accelerations of 2, 4, 8, 4, 8, and 16, respectively. The aliased slice time-series images were then separated using the

mSPECS(-IPA) separation method, and the fMRI activation was calculated in each separated voxel using the complex-valued fMRI model in [Rowe et al., 2005b]. To evaluate the mSPECS(-IPA) separation, the separated time-series is compared to the activation statistics for the original activation statistics.

## 4.4 Results

### 4.4.1 Digital Phantom Simulation Results

The initial digital phantom magnitude and phase axial slice images for the simulation are shown in Fig. 4.5. The separated magnitude images of the time-series mean are shown in Fig. 4.6 for the mSPECS 2, mSPECS 4, and mSPECS 8 with no in-plane acceleration, or IPA 1, and shown in Fig. 4.8 for the mSPECS 2, mSPECS 4, and mSPECS 8 with an in-plane acceleration of $R$=2, or IPA2. The corresponding separated phase images of the time-series mean are shown in Fig. 4.6 for the mSPECS 2, mSPECS 4, and mSPECS 8 with no in-plane acceleration, or IPA1, and shown in Fig. 4.8 for the mSPECS 2, mSPECS 4, and mSPECS 8 with an in-plane acceleration of $R$=2, or IPA2. For the $R$=1 scenario, or the mSPECS reconstruction, there is no apparent residual aliasing from the time-series separation, and each acceleration appears identical in the separated magnitude and phase images. For the $R$=2 scenario, or the mSPECS-IPA reconstruction, there is residual aliasing from the time-series separation. Although, the residual aliasing is an in-plane artifact, with a pattern resembling the fold-over artifacts illustrated in Fig. 4.3a. The in-plane aliasing is more noticeable as the number of aliased

slices within a packet increases, is observed in both the separated magnitude and phase slice images of the time-series mean, and also appears to be a function of the mean phase in the initial slice image time-series. Phase transitions in mSPECS(-IPA) is further explored in Appendix A. Another comparison with the mSPECS(-IPA) methods is to examine the trade-off with number of aliased slices and in-plane acceleration for the same acceleration factors. For an acceleration of 4, the preferred scenario for the mSPECS(-IPA) methods is the mSPECS 4 – IPA 1 over the mSPECS 2 – IPA 2. Unlike parallel imaging methods or in-plane accelerations, there is no intrinsic SNR penalty with SMS methods. However, for an acceleration of 8, the preferred scenario is not as straightforward when comparing the mean magnitude and phase of mSPECS 8 – IPA 1 to mSPECS 4 – IPA 2. To distinguish the favorable scenarios for the same accelerations, the activation statistics are examined.

After the mSPECS(-IPA) slice image separation of the aliased time-series, the fMRI activation statistics are calculated in each voxel with a complex-valued activation model [Rowe 2005b]. The *z*-scores for the activation statistics are mapped in Fig 4.10 and Fig. 4.11, and the regions where the activation was originally placed is highlighted by the green box in each slice. The activation maps are thresholded at 2.5, and the region outside the digital phantom is masked. Since the activation is placed in a unique 6×6 region in each slice image, before simulating the aliased time-series, and there are no incremental shifts in the FOV, inter-slice signal leakage stemming from the slice separation process is easily identifiable by visually examining previously aliased voxels in the same ($x$,$y$) locations. Intra-slice signal leakage, or aliasing artifacts from the image wrapping due to in-plane acceleration, will appear in the fold-over as described in Fig. 4.3. The regions

within the green boxes show strong activation clusters. As discussed in the mSPECS chapter, the average *z*-scores increase as the acceleration increases, with a comparison of IPA 1 and IPA 2, the activation statistics in IPA 1 are slightly increased, although there is not a substantial difference between the two scenarios. There are no apparent clusters of "active" voxels outside the green boxes in Fig 4.10 and Fig. 4.11, so any active voxels outside the voxels indicate false positives from noise in the time-series, rather than inter-slice signal leakage.

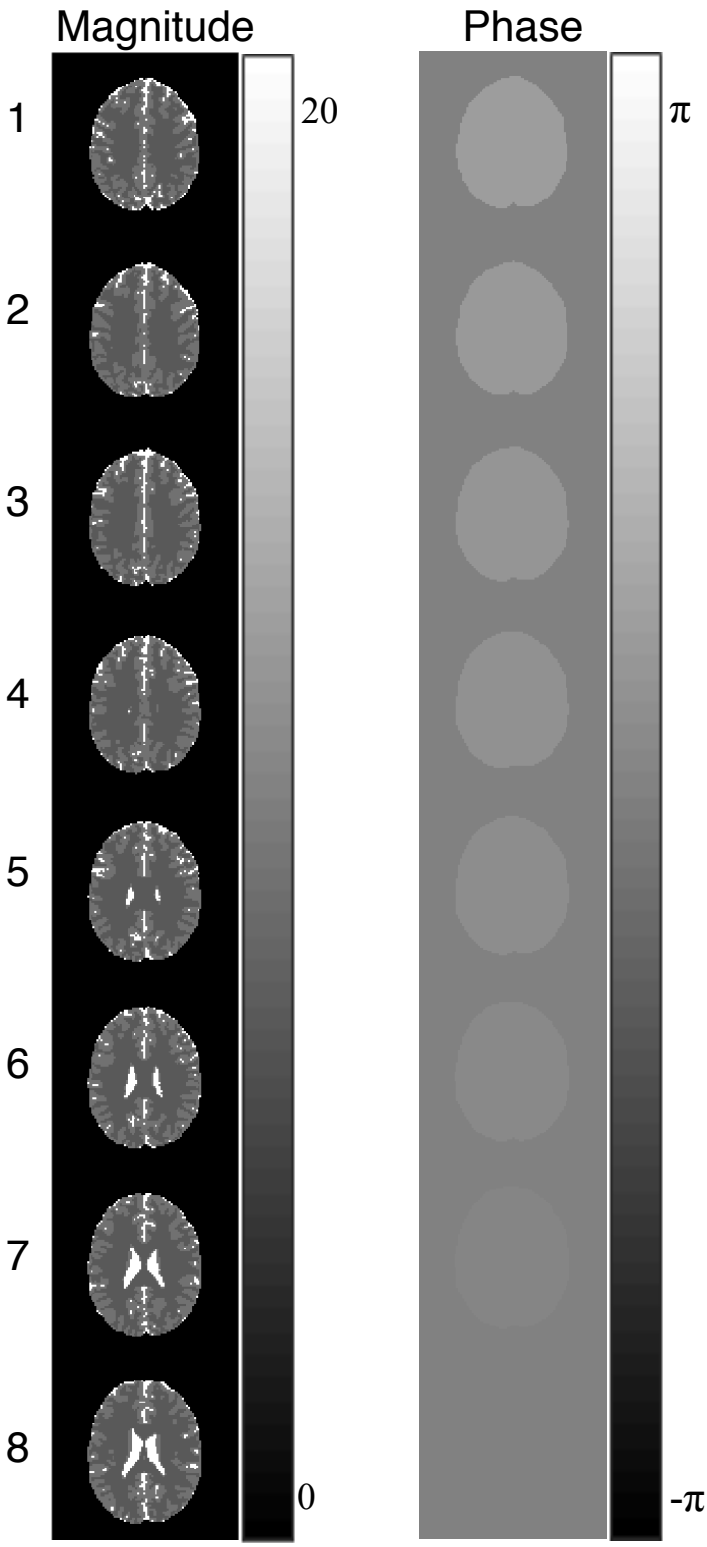


**Figure 4.5:** Initial magnitude slice images and phase slice images for the phantom simulation,, with the numbering 1 through 8 referring to the slice image number.

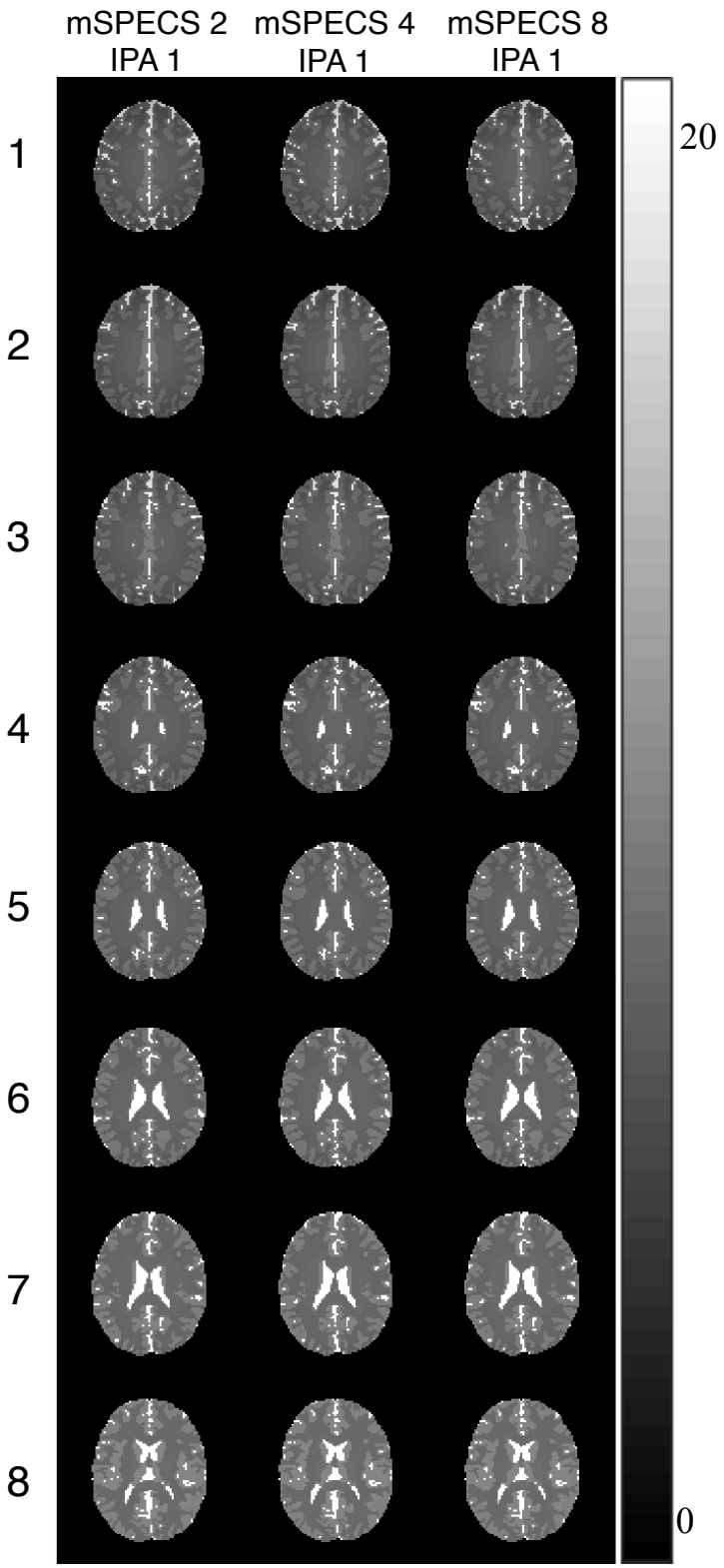


**Figure 4.6:** Mean magnitude separated images from the digital phantom simulation for the net acceleration of 2 (mSPECS 2 – IPA 1), 4 (mSPECS 4 – IPA 1), and 8 (mSPECS 8 – IPA 1).

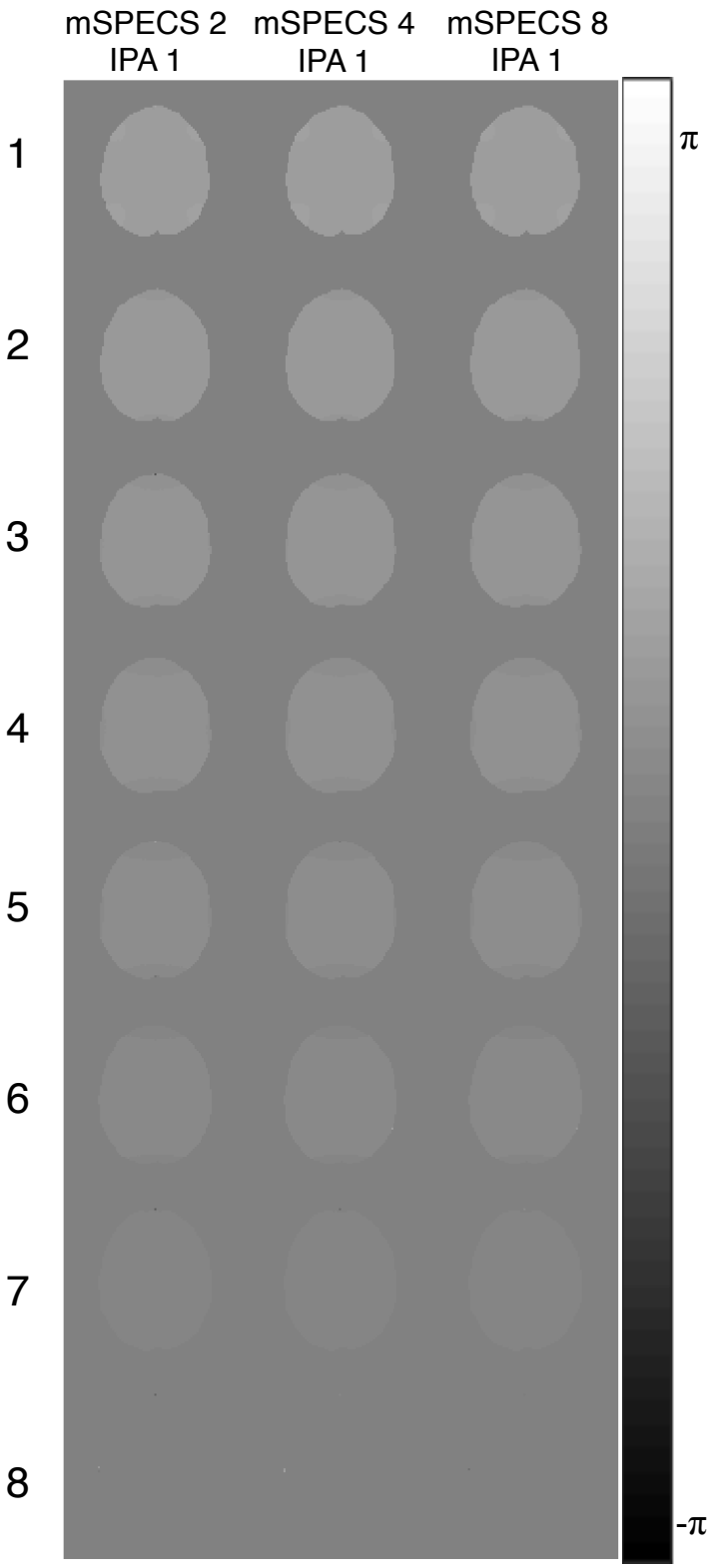


**Figure 4.7:** Mean phase separated images from the digital phantom simulation for the net acceleration of 2 (mSPECS 2 – IPA 1), 4 (mSPECS 4 – IPA 1), and 8 (mSPECS 8 – IPA 1).

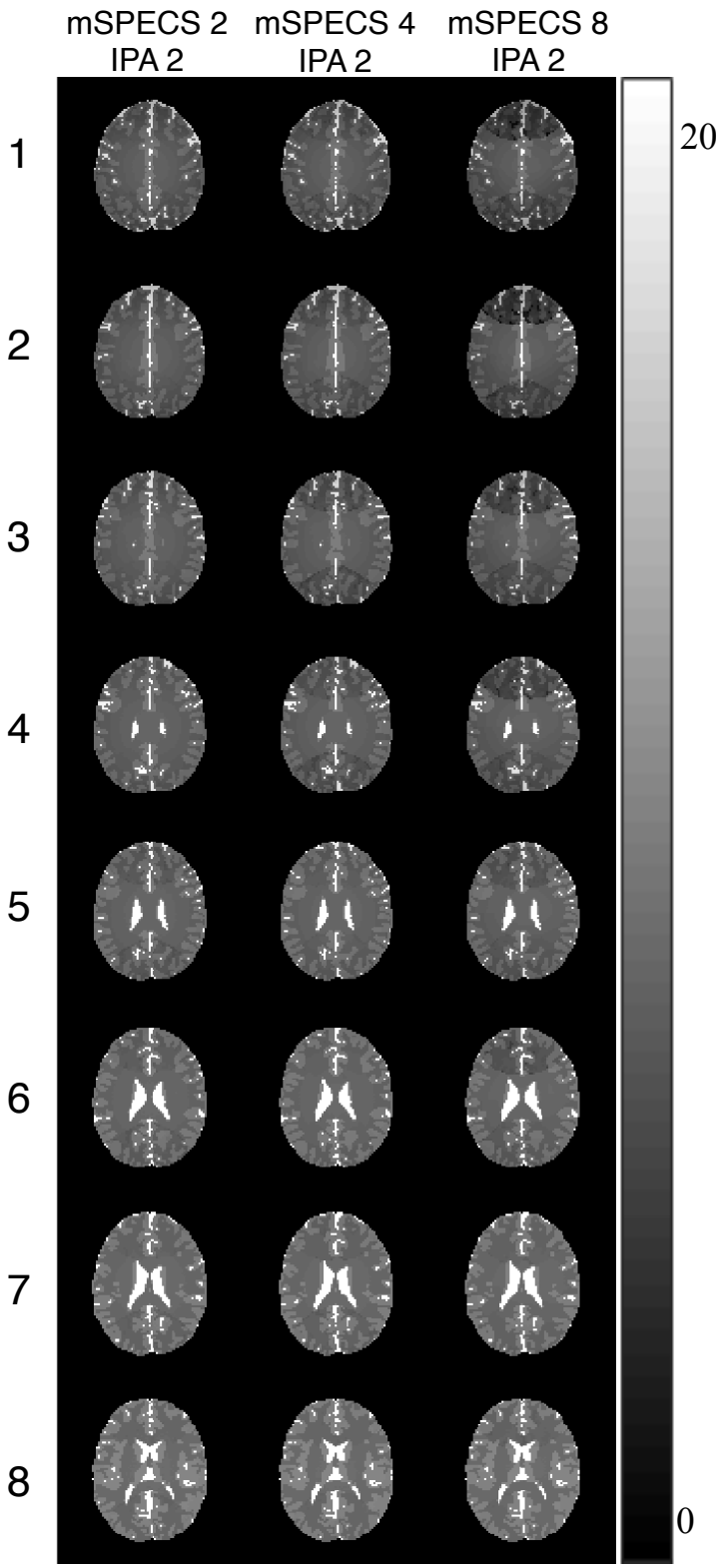


**Figure 4.8:** Mean magnitude separated images from the digital phantom simulation for the net acceleration of 4 (mSPECS 2 – IPA 2), 8 (mSPECS 4– IPA 2), and 16 (mSPECS 8 – IPA 2).

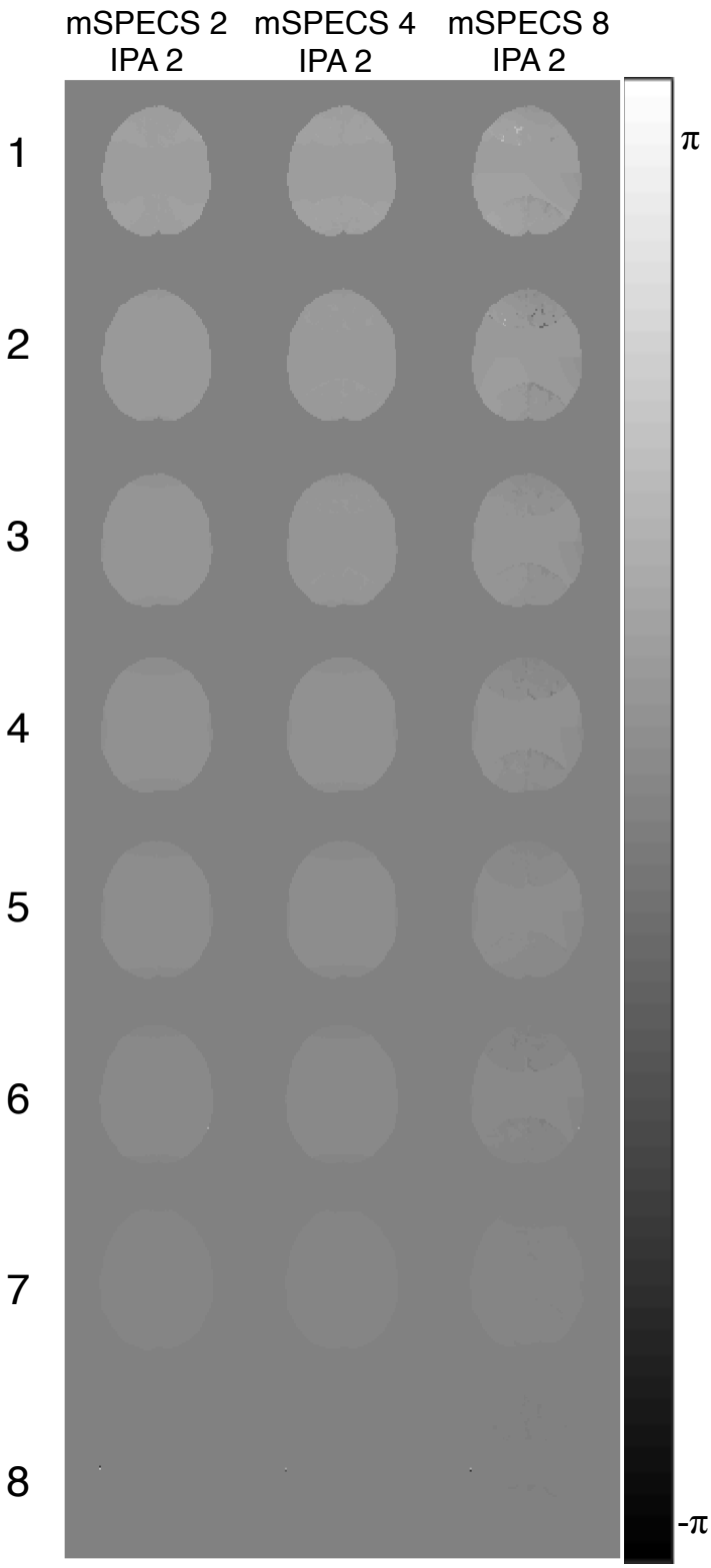


**Figure 4.9:** Mean phase separated images from the digital phantom simulation for the net acceleration of 4 (mSPECS 2 – IPA 2), 8 (mSPECS 4– IPA 2), and 16 (mSPECS 8 – IPA 2).

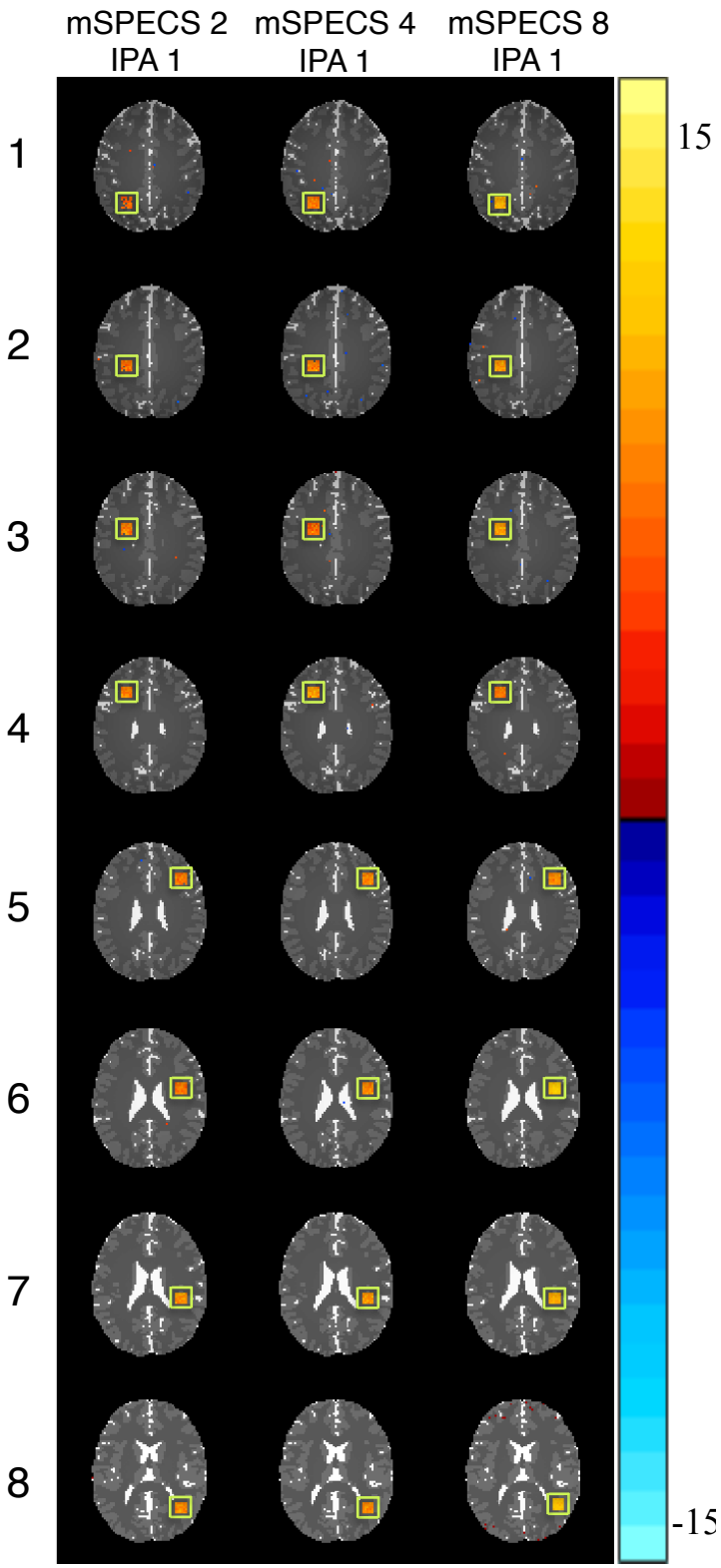


**Figure 4.10:** Activation statistics from the mSPECS separated images from the digital phantom simulation for the net acceleration of 2 (mSPECS 2 – IPA 1), 4 (mSPECS 4 – IPA 1), and 8 (mSPECS 8 – IPA 1).

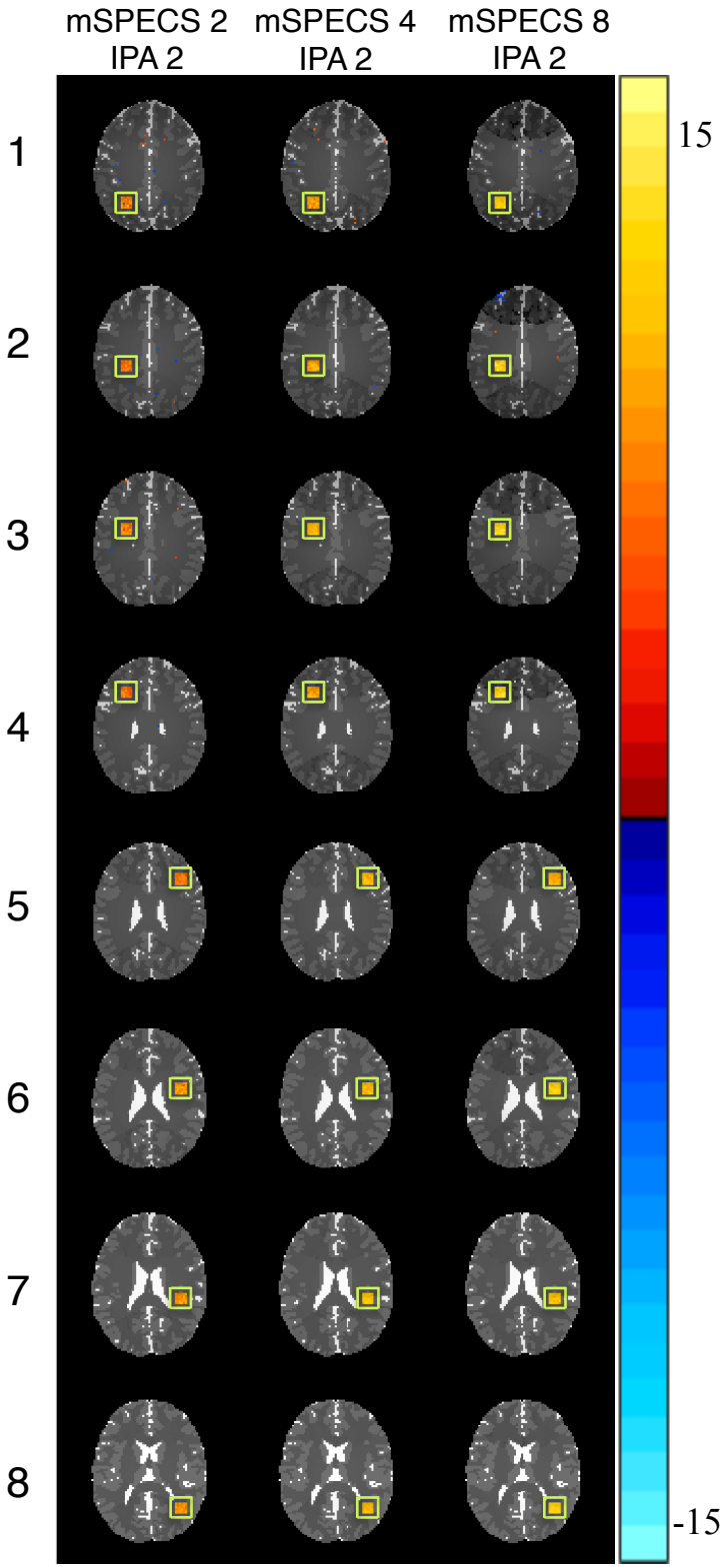


**Figure 4.11:** Activation statistics from the mSPECS separated images from the digital phantom simulation for the net acceleration of 4 (mSPECS 2 – IPA 2), 8 (mSPECS 4– IPA 2), and 16 (mSPECS 8 – IPA 2).

### 4.4.2 Experimental Human Subject Data Simulation Results

The initial experimental human subject data magnitude and phase axial slice images for the simulation are shown in Fig. 4.12. The separated magnitude images of the mean time-series are shown in Fig. 4.13 for the mSPECS 2, mSPECS 4, and mSPECS 8 with no in-plane acceleration, or IPA 1, and shown in Fig. 4.15 for the mSPECS 2, mSPECS 4, and mSPECS 8 with an in-plane acceleration of $R$=2, or IPA2. The corresponding separated phase images of the mean time-series are shown in Fig. 4.14 for the mSPECS 2, mSPECS 4, and mSPECS 8 with with no in-plane acceleration, or IPA1, and shown in Fig. 4.16 for the mSPECS 2, mSPECS 4, and mSPECS 8 with with an in-plane acceleration of $R$=2, or IPA2. For the $R$=1 scenario, or the mSPECS reconstruction, there is no apparent residual aliasing from the time-series separation, and each acceleration appears identical in the separated magnitude images. Although, the is a discrepancy between the mSPECS(-IPA) separated slice images in Fig. 4.14 and Fig 4.16 and the initial phase images in Fig. 4.12 at the $\pi$/-$\pi$ boundary. For the $R$=2 scenario, or the mSPECS-IPA reconstruction, there is residual aliasing from the time-series separation. Although, the residual aliasing is an in-plane artifact, with a pattern resembling the fold-over artifacts illustrated in Fig. 4.3a. The in-plane aliasing is more noticeable as the number of aliased slices within a packet increases, is observed in both the mean separated magnitude and phase slice images, and the wrap-around artifacts are more noticeable in the phase images for mSPECS 4 - IPA 2 and mSPECS 8 - IPA 2, as seen in Fig. 4.15. Phase transitions in mSPECS(-IPA) and signal attenuation is further explored in Appendix A. Another comparison with the mSPECS(-IPA) methods is to

examine the trade-off with number of aliased slices and in-plane acceleration for the same acceleration factors. For an acceleration of 4, the preferred scenario for the mSPECS(-IPA) methods is the mSPECS 4 – IPA 1 over the mSPECS 2 – IPA 2. Unlike parallel imaging methods or in-plane accelerations, there is no intrinsic SNR penalty with SMS methods. However, for an acceleration of 8, the preferred scenario is more straightforward when comparing the mean magnitude and phase of mSPECS 8 – IPA 1 to mSPECS 4 – IPA 2, than in the digital phantom simulation. In the experimental human data simulation, the slice image quality degrades faster at higher acceleration from the uncontrolled phase, or phase wrapping. Compared to the digital phantom simulation, the detail of the experimental human data makes potential residual aliasing artifacts harder to identify. To distinguish the favorable scenarios for the same accelerations, the activation statistics are examined.

After the mSPECS(-IPA) slice image separation of the aliased time-series, the fMRI activation statistics are calculated in each voxel with a complex-valued activation model [Rowe 2005b]. The *z*-scores for the activation statistics are mapped in Fig 4.17 and Fig. 4.18. The activation maps are thresholded at 1.25, and the region outside the brain is masked. Since there are no incremental shifts in the FOV, inter-slice signal leakage stemming from the slice separation process is easily identifiable by visually examining previously aliased voxels in the same ($x$,$y$) locations. The motor cortex show strong activation clusters in Slice 1 and Slice 2 for IPA1 and IPA2. As discussed in the mSPECS chapter, the average *z*-scores increase as the acceleration increase, which is apparent in the comparison of mSPECS 2 and mSPECS 4 for both IPA1 and IPA2. The activation statistics for mSPECS 8 IPA1 and mSPECS 8 IPA2 compared to the other accelerations,

show reduced false activation outside the primary motor cortex and the primary motor cortex is more distinguishable. With a comparison of IPA1 and IPA2, the activation statistics in IPA1 are slightly increased, although there is not a substantial difference between the two scenarios. There are no apparent new clusters of “active” voxels in the motor cortex region in Fig 4.17 and Fig. 4.18 in the inferior slice images, so any active voxels outside the voxels indicate false positives from noise in the time-series, rather than inter-slice signal leakage.

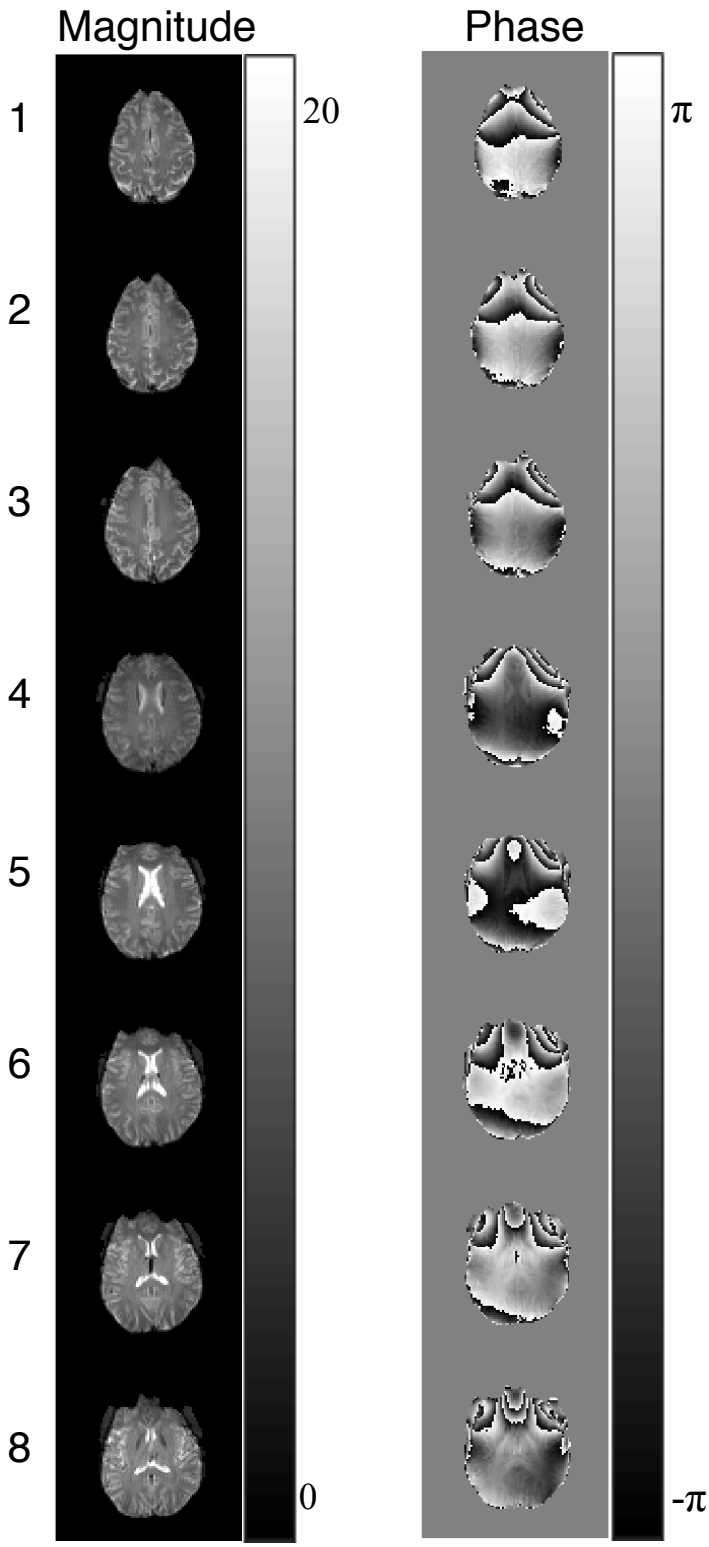


**Figure 4.12:** Initial magnitude and phase slice images for the experimental human data simulation, with the numbering 1 through 8 referring to the slice image number**.**

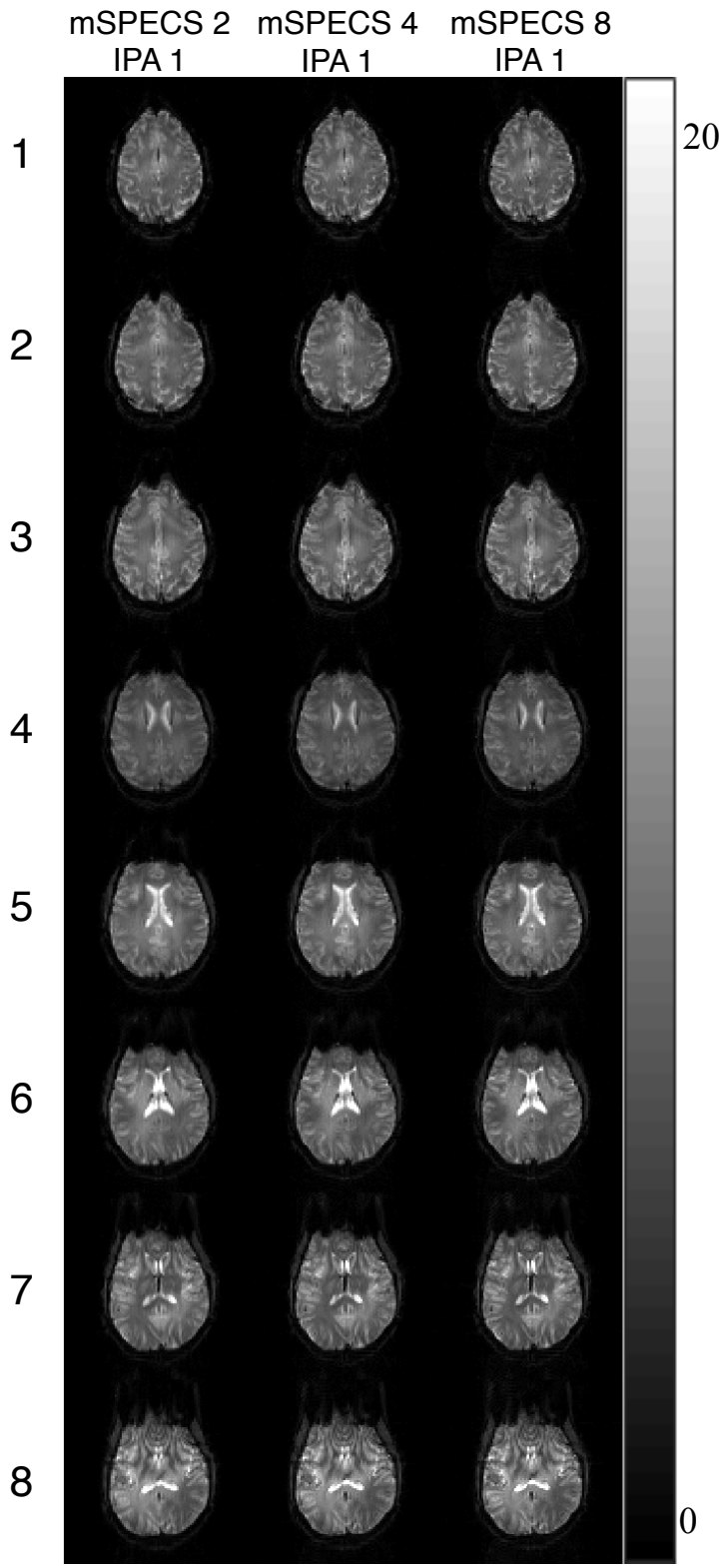


**Figure 4.13:** Mean magnitude separated images from the human data simulation for the net acceleration of 2 (mSPECS 2 – IPA 1), 4 (mSPECS 4 – IPA 1), and 8 (mSPECS 8 – IPA 1).

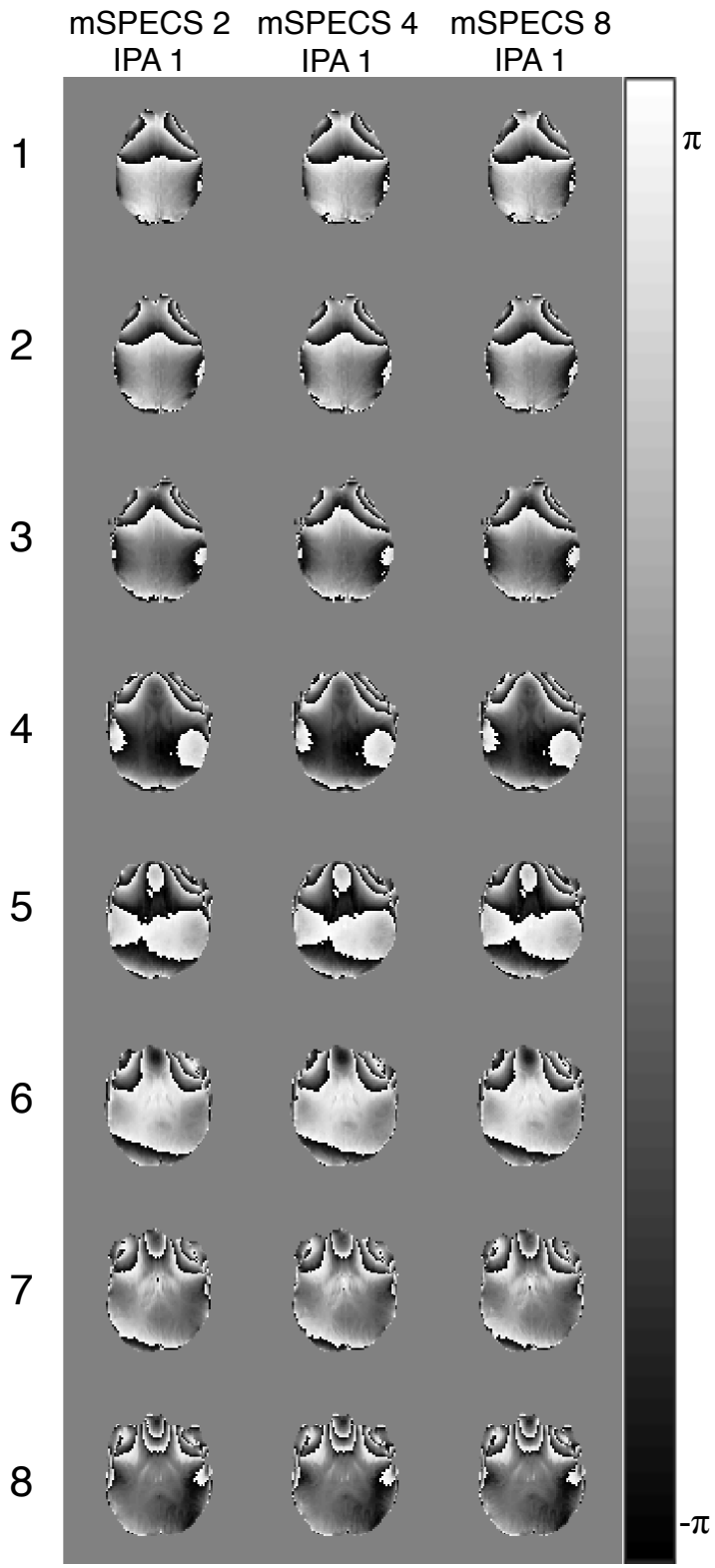


**Figure 4.14:** Mean phase separated images from the human data simulation for the net acceleration of 2 (mSPECS 2 – IPA 1), 4 (mSPECS 4 – IPA 1), and 8 (mSPECS 8 – IPA 1).

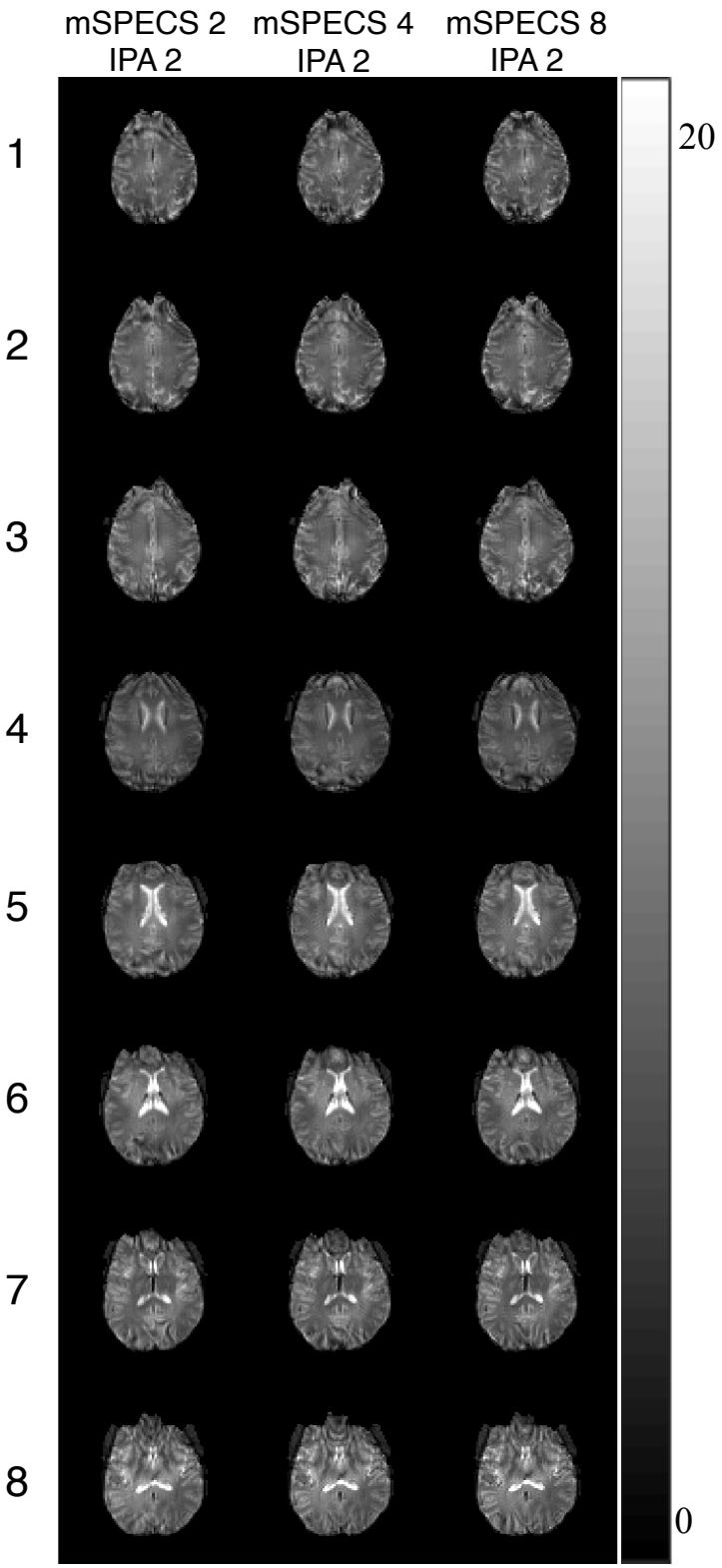


**Figure 4.15:** Mean magnitude separated images from the human data simulation for the net acceleration 4 (mSPECS 2 – IPA 2), 8 (mSPECS 4– IPA 2), and 16 (mSPECS 8 – IPA 2).

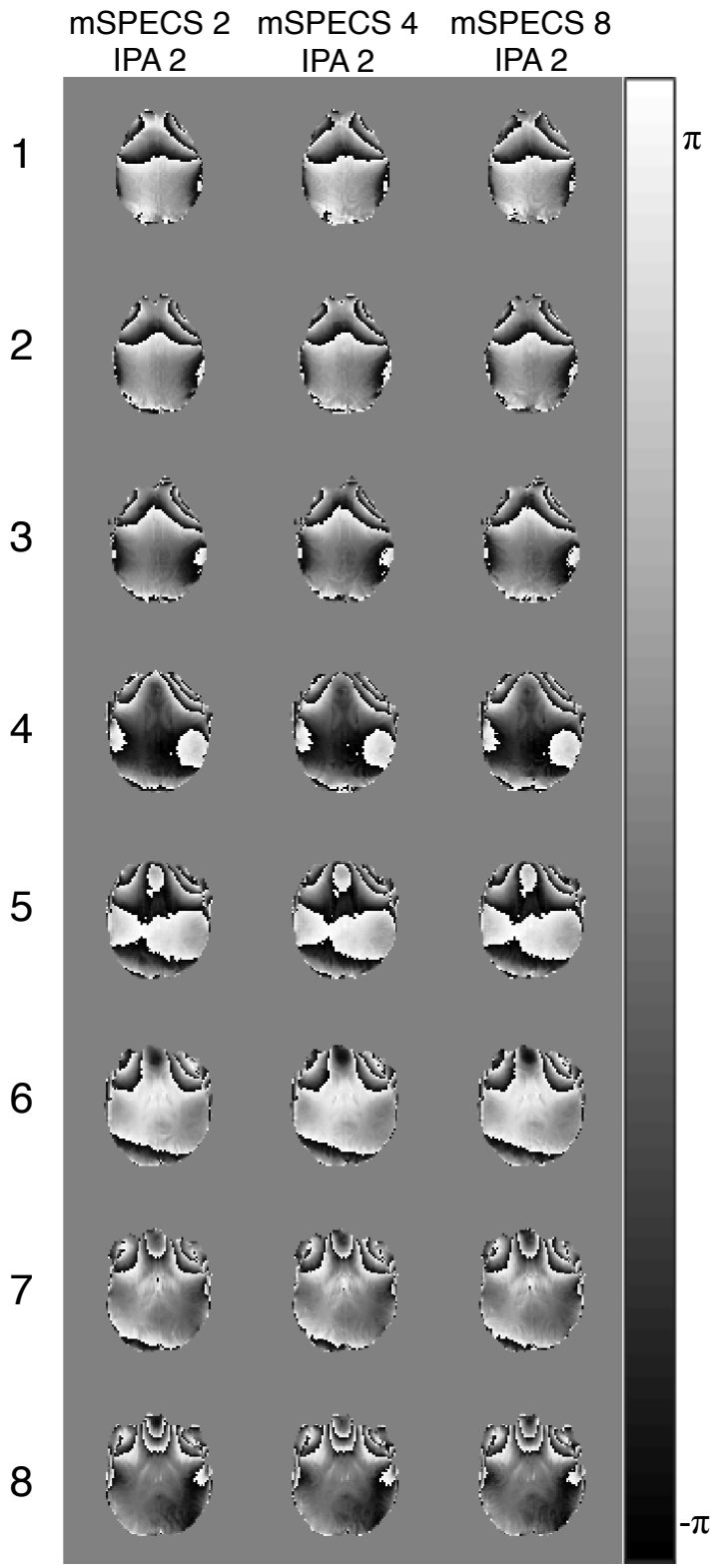


**Figure 4.16:** Mean phase separated images from the human data simulation for the net acceleration of 4 (mSPECS 2 – IPA 2), 8 (mSPECS 4– IPA 2), and 16 (mSPECS 8 – IPA 2).

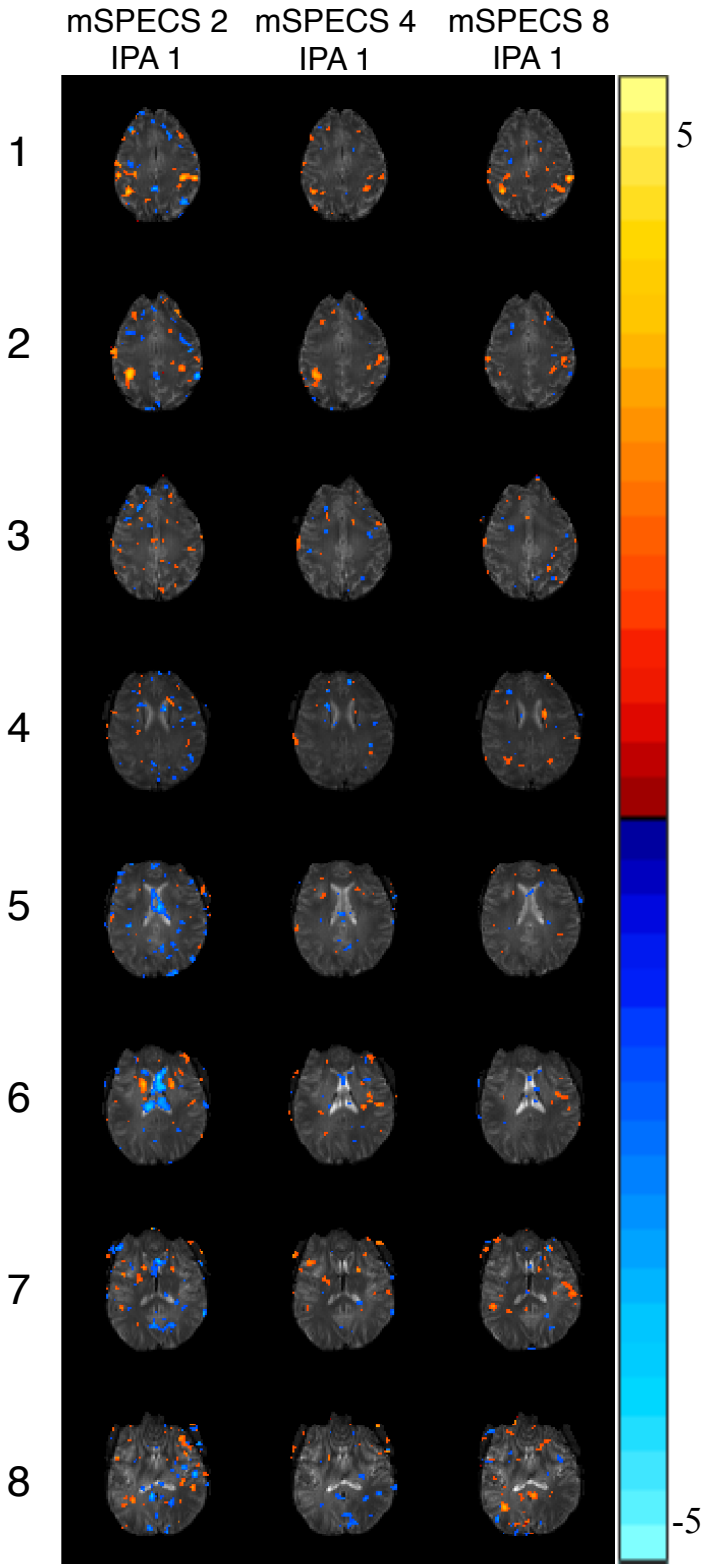


**Figure 4.17:** Activation statistics from the human data simulation for the net acceleration of 2 (mSPECS 2 – IPA 1), 4 (mSPECS 4 – IPA 1), and 8 (mSPECS 8 – IPA 1).

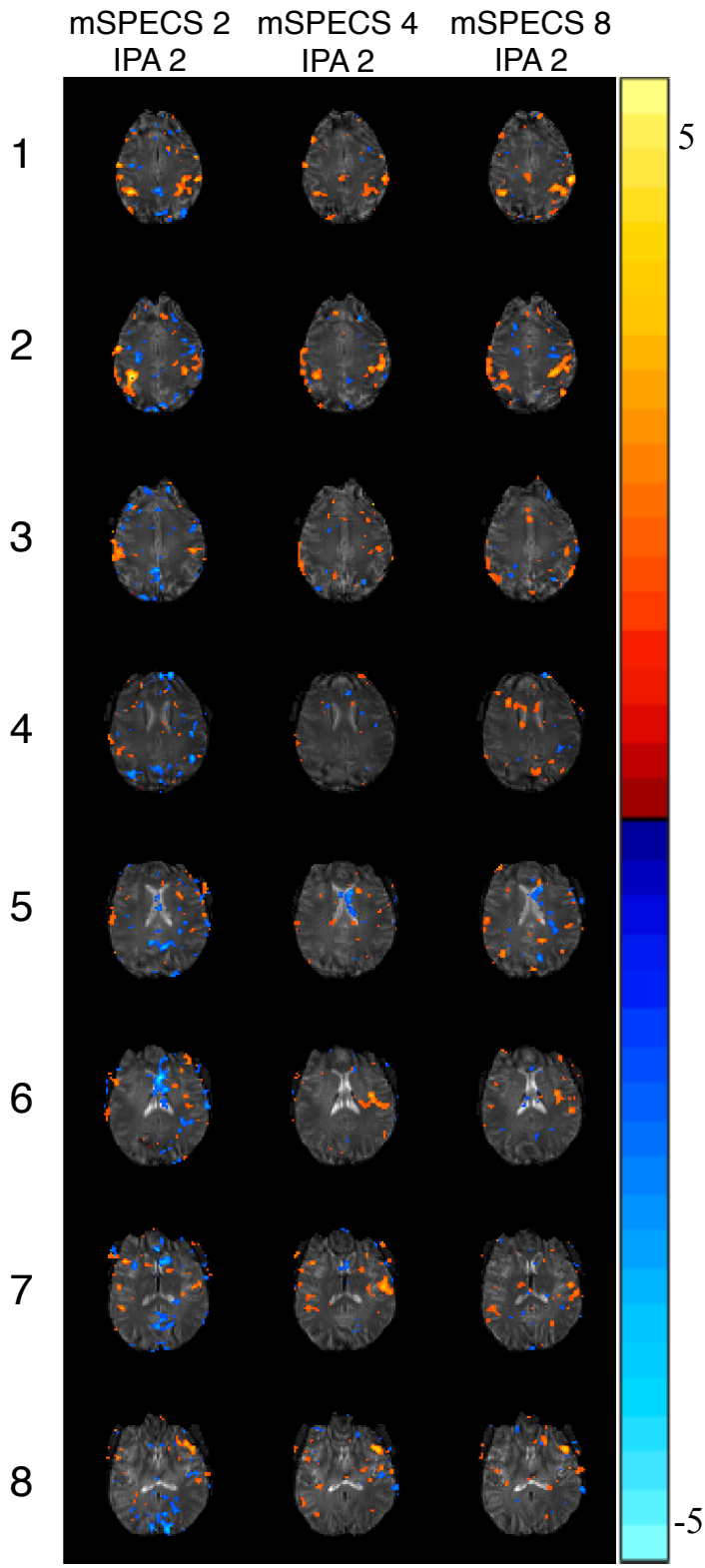


**Figure 4.18:** Activation statistics from the human data simulation for the net acceleration 4 (mSPECS 2 – IPA 2), 8 (mSPECS 4– IPA 2), and 16 (mSPECS 8 – IPA 2).

## 4.5 Discussion

The results of the digital phantom and experimental human simulations readily demonstrate the utility of the mSPECS-IPA reconstruction algorithm for accelerations up to 16 for Hadamard SMS data acquisitions with in-plane subsampling. Not only is the bootstrap calibration algorithm adopted from mSPECS for mSPECS-IPA, but the novelity introduced with mSPECS-IPA is the spatial encoding to maintain orthogonality both in-plane and through-plane. This approach places the activation in the correct location through minimizing the correlation induced for voxel separation. The mSPECS(-IPA) methods address the lack of SMS reconstruction techniques that allow a true reduction of the time required for the time-series acquisition, without sacrificing the quality of the activation statistics.

The time-series unaliasing artifacts, from in-plane unaliasing, in the digital phantom simulations are more apparent than in the experimental human simulations. They may be more visually apparent in the digital phantom simulations, since the magnitude images are less intricate compared to the experimental human data slice images, so the artifacts are easily identifiable. The in-plane artifacts in the mean phase images for both simulations display similar levels of residual in-plane aliasing particularly in mSPECS 4 – IPA 2 and mSPECS 8 – IPA 2. In the experimental human simulation, the increased acceleration factor yields a more distinguishable motor cortex region, with or without the in-plane acceleration, as this increases the number of time points sampling, which corresponds to increased statistical confidence in the data. The

development of mSPECS to include the in-plane aliasing dimensions, yields a more dynamic SMS reconstruction method.

# Chapter 5: Conclusions

## 5.1 Summary of Presented Work

The development of novel complex-valued statistical analysis and reconstruction methods in fMRI, improves the modeling of the fMRI time-series so the true neural networks of interest are accurately identified. With the complex-valued description of correlation, increased sensitivity and specificity was demonstrated with seed voxels in the motor cortex with low CNR. With a reduction of spurious false correlation observed in the complex-valued data, the increased power of the complex-valued description of covariance is particularly advantageous for low CNR fMRI data sets or small population studies. The increased specificity and sensitivity of complex-valued data over magnitude-only data also reduces the post reconstruction processing required to improve the SNR and CNR of the fMRI data before the analysis. This is a beneficial aspect of the complex-valued framework, as signal processing has been shown to induce correlations, and different processing pipelines may induce systematic correlations across multiple subjects.

The ability to identifying neural networks of interest is also a function of the quality of the slice image acquisition and reconstruction methods. SMS-fMRI methods are advantageous for fMRI, as they correspond to a higher sampling rate yielding a higher sample size compared to traditional EPI methods with no acceleration. More time points increases the degrees of freedom, which increases the number of regression coefficients for a more robust analysis of the fMRI data. Whole volume SMS-fMRI

acquisitions are also beneficial to freeze out motion artifacts within the volume acquisition for a single TR. Although, minimizing induced correlation and residual aliasing artifacts are a substantial obstacle in SMS-fMRI acquisition and reconstruction schemes. The mSPECS(-IPA) reconstruction methods presented address the need for the development of SMS reconstruction methods that prevent inter-slice signal leakage in previously aliased voxels.

Correlation between previously aliased slices is a result of poor disentanglement of the signal or separation of the mean voxel values. The mSPECS separation technique, avoids residual artifacts from unaliasing, by implementing a bootstrap sampling algorithm of calibration images for each TR across the time-series, and incorporating the orthogonal coefficients of Hadamard coefficients in the acquisition and the coil sensitivity separation matrix. The mSPECS-IPA method builds on the mSPECS method by incorporating in-plane subsampling to achieve higher accelerations for ultra-fast observation of brain function. The novelty of mSPECS-IPA is the orthogonal 2-dimensional Hadamard phase encoding of the aliased slice images, so the orthogonality aliased images is maintained in-plane and through-plane. Both mSPECS and mSPECS-IPA were shown to accurately place the BOLD signal after the aliased slice image separation, and showed promising results for accelerations with an MB8 and IPA2. Optimizing fMRI analysis methods and SMS-fMRI techniques of data acquisition and reconstruction with respect to slice separation methods allows for faster observation of the true cognitive dynamics, and increases the application of fMRI in clinical settings.

## 5.2 Future Work

As for the work described in the first chapter on complex-valued correlation in low CNR data sets, a natural extension of the project would be to apply the framework to functional connectivity MRI (fcMRI). In fcMRI, the subject does not perform a task during the time-series image acquisition. The resting state neural networks are found in the low temporal frequency range, and detected with seed voxel correlation analysis. Another interesting application to the temporal Fourier framework would be to implement the framework to fcMRI or fMRI data sets to a population study. Including the phase in the time-series analysis increases the statistical power of the analysis, making complex-valued fMRI analysis particularly advantageous for studies with a small number of subjects. Thus, an interesting study would be to examine the threshold, at which the number of subjects in the study reduces the significance of the added sensitivity and specificity of including the phase in the statistical analysis of the data.

As for the last two chapters, an application of the mSPECS and mSPECS-IPA reconstruction methods, to a blipped-CAIPI acquisition, rather than Hadamard encoded acquisitions, would be a worthwhile application to the reconstruction methods. Although, there are potential difficulties associated with blipped-CAIPI acquisitions, such as disentangling the signal of interest from the ghosting artifacts in the reconstructed images. The mSPECS and mSPECS-IPA methods easy facilitate the blipped-CAIPI acquisitions by changing the Hadamard aliasing matrices to reflect the shifted FOV aliasing patterns associated with blipped-CAIPI acquisitions. A single coil version, the

Separation of Parallel Encoded Complex-valued Slices (SPECS), with the blipped-CAIPI shifts has been recently published [Rowe et al., 2016].

# Appendix A: A demonstration of signal attenuation in mSPECS(-IPA) images from phase accumulation in the aliased time-series.

A MATLAB simulation demonstrates the signal attenuation in mSPECS(-IPA) separated Hadamard encoded arising from phase wrapping. Four slices are generated with a magnitude with a theoretical $T_2^*$ weighted phantom similar to [Karaman et al., 2016]. The initial $T_2^*$ weighted phantom has values between 0 and 1, the magnitude is weighted by a factor of 20, and a mean phase is added to each slice of 1π/36, 5π/36, 9π/36, 15π/36. To demonstrate the phase wrapping a phase differential in a 14×14 region is added to the phase in each slice of 1π/3, 2π/3, π, 4π/3, respectively. The initial mean magnitude and phase images are shown in Fig. A.1. A time-series is generated of 100 time points for each slice, then weighted by the complex-valued 32-channel coil sensitivities , with standard Gaussian noise added to each slice image. The Hadamard encoded time-series is simulated for an mSPECS-IPA reconstruction, as described in Chapter 4 of this dissertation, with an MB factor of 4 and in-plane subsampling of 2, MB4 IPA2.

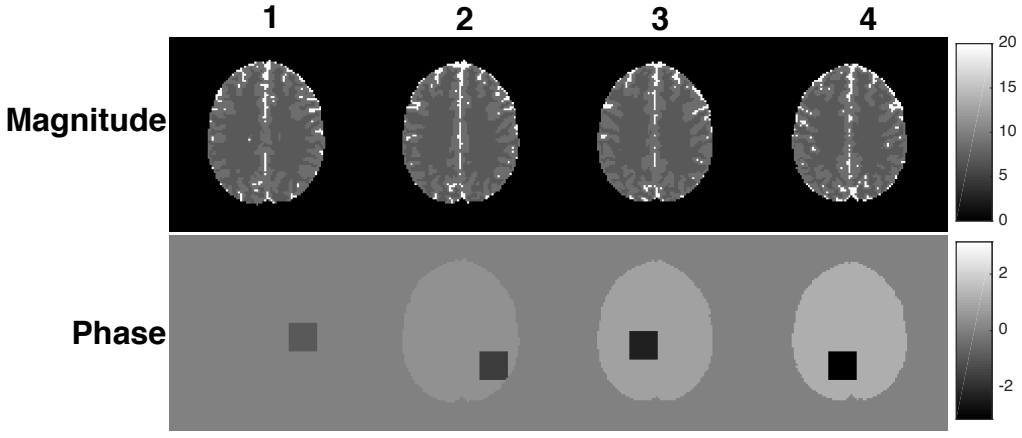


**Figure A.1:** Original mean magnitude and phase images across 4 slices.

The calibration images for the four slices are simulated with the same magnitude and phase as with the aliased time-series. Two separation scenarios are demonstrated in the simulation. In the first scenario, the fully sampled calibration time-series is generated with the 14×14 phase wrapped regions, and in the second scenario, the fully sampled calibration time-series is generated without the phase wrapped regions. The calibration time-series is then generated for 16 time points, then weighted by the complex-valued 32-channel coil sensitivities, and standard Gaussian noise is added to each slice image.

The aliased time-series is separated with the mSPECS-IPA method described in Chapter 4. The mean separated magnitude and phase slice images are shown for scenario 1, the scenario with the 14×14 phase wrapped regions in the calibration images, in Fig. A.2, and for scenario 2, the scenario without the 14×14 phase wrapped regions in the calibration images, in Fig. A.3.

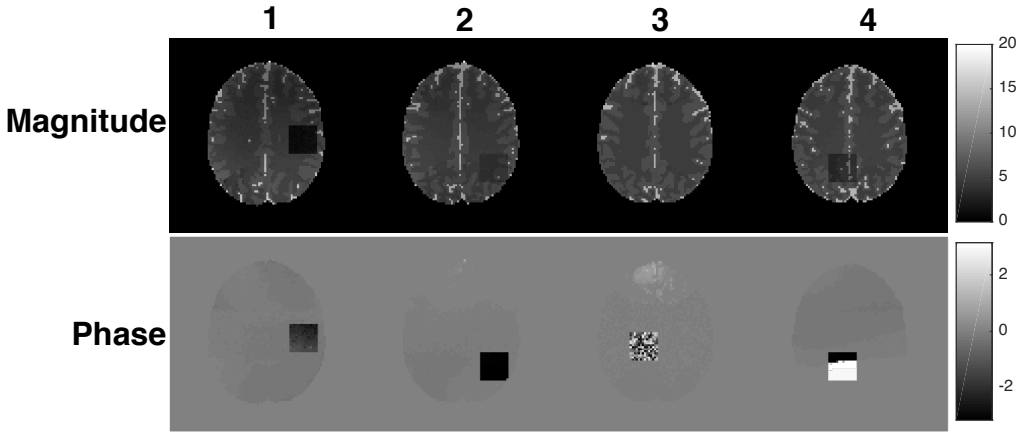


**Figure A.2:** mSPECS-IPA reconstructed mean magnitude and phase images across 4 slices with the calibration images described in scenario 1.

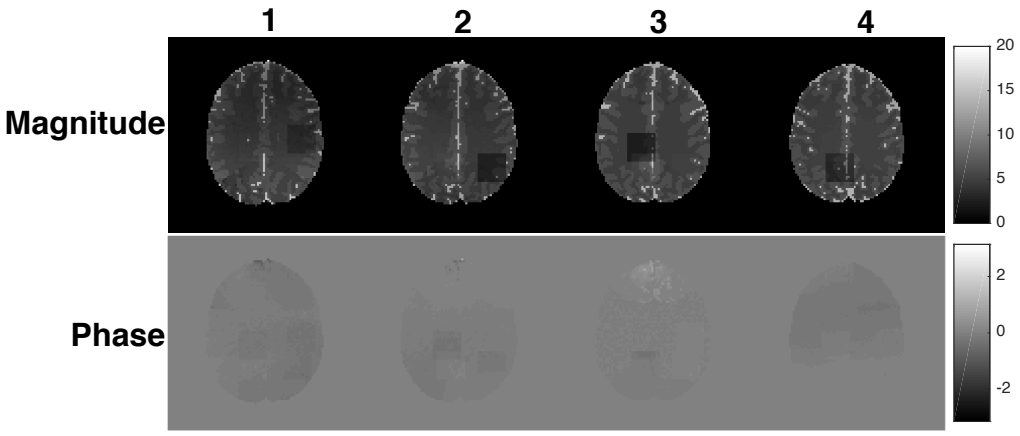


**Figure A.3:** mSPECS-IPA reconstructed mean magnitude and phase images across 4 slices with the calibration images described in scenario 2.

In both scenarios, the wrapping in the phase time-series spreads to the magnitude images after slice separation with mSPECS-IPA. Since the mSPECS(-IPA) separation method is a reconstruction using the real and imaginary parts of the acquired series, discontinuities initially presented in the phase time-series that are not reflected in the magnitude time-series, may arise in the post separation magnitude time-series, despite the calibration time-series.

## Appendix B: Magnitude correlation for mSPECS(-IPA).

The magnitude-only correlation is computed for mSPECS(-IPA) separated sliced images in the MATLAB simulation in Aim 3. In Fig. B.1 and Fig. B.2, the center voxel is chosen as the seed voxel for each slice in the second packet, which contains the four even slices, reconstructed with mSPECS 4 – IPA 1 and mSPECS 4 – IPA 2. In the figures, the 96×96 images along the diagonal correspond to the correlation between the seed voxel and the other voxels within the slice, and the off diagonal 96×96 images correspond to the correlation between the seed voxel and another slice denoted by the slice column number. Without an mSPECS(-IPA) reconstruction high correlation among previously aliased regions is expected. In both scenarios, no increased correlation among previously aliased voxels is observed.

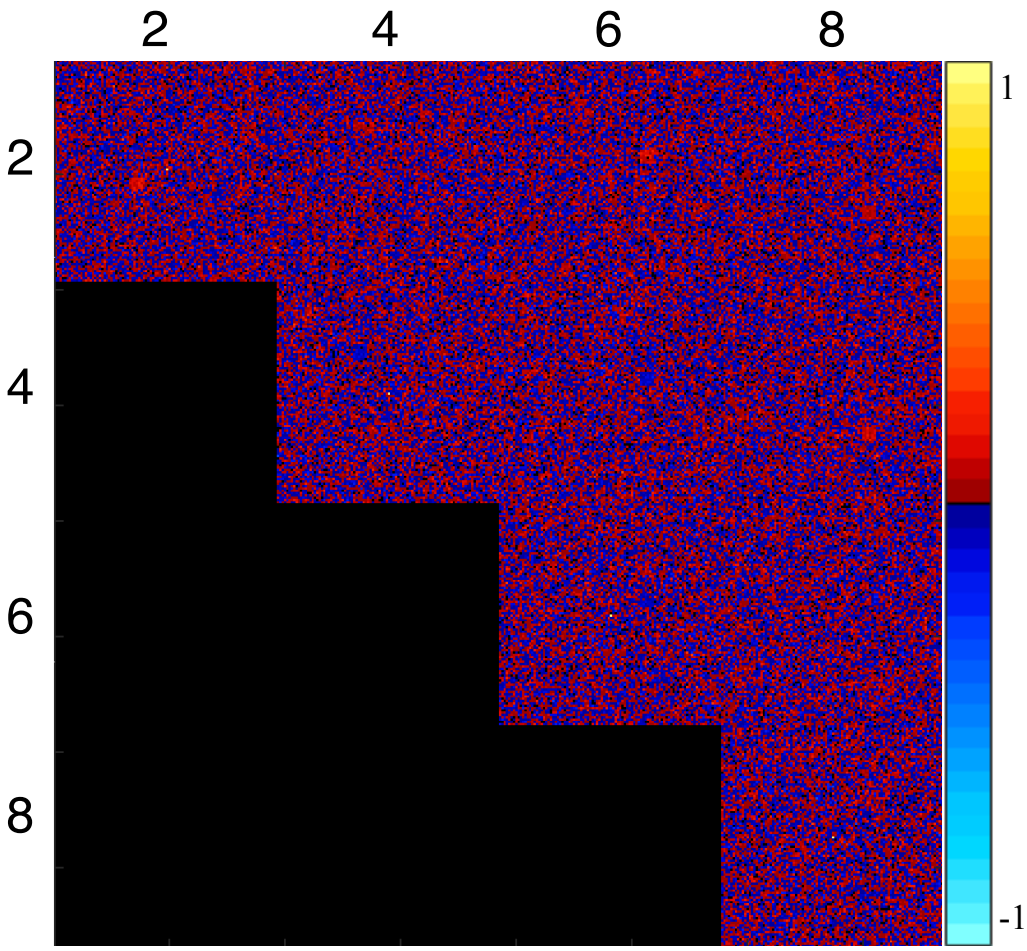


**Figure B.1:** MO correlation for the second packet reconstructed with mSPECS 4 - IPA 1.

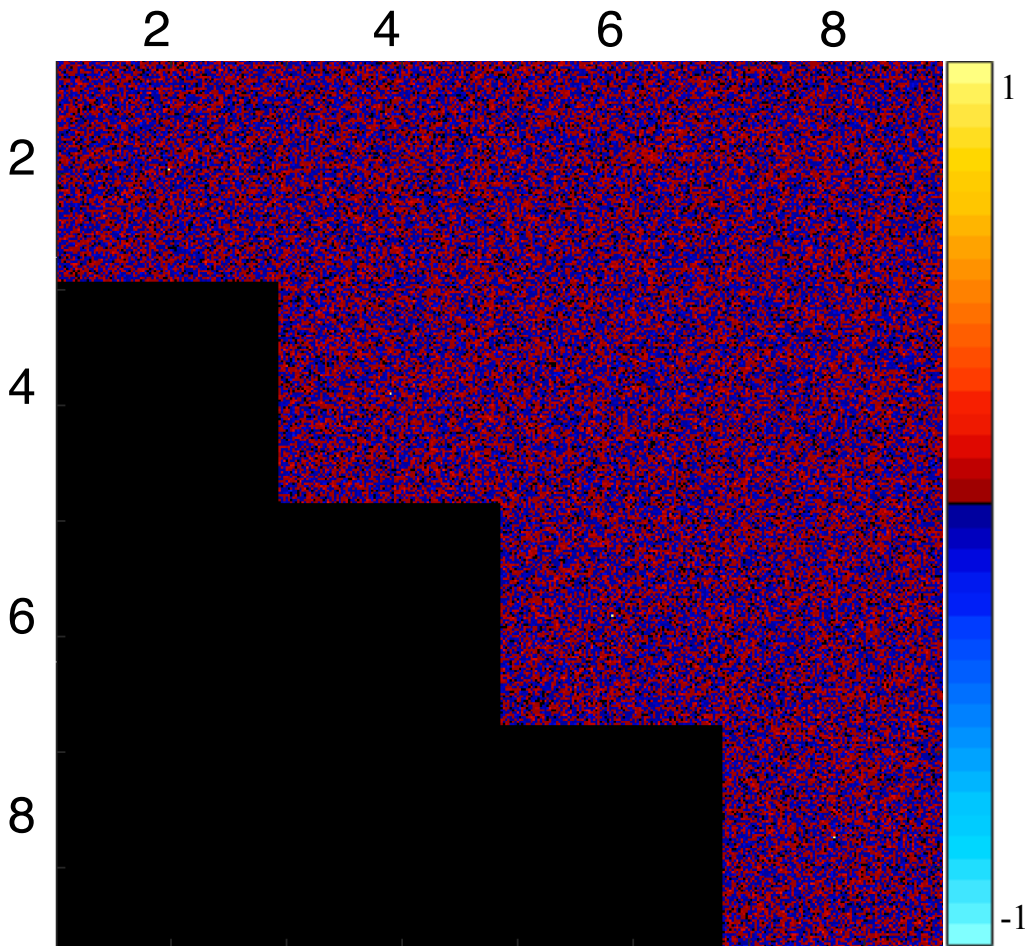


**Figure B.2:** MO correlation for the second packet reconstructed with mSPECS 4 - IPA 2.

# BIBLIOGRAPHY

Arja SK, Feng Z, Chen Z, Caprihan A, Kiehl KA, Adali T, Calhoun VD. Changes in fMRI magnitude data and phase data observed in block-design and event-related tasks, Neuroimage 2010;49:3149–60.

Bandettini PA, Wong EC, Hinks RS, Tikofsky RS, Hyde JS. Time course EPI of human brain function during task activation. Magn Reson Med 1992;25:390–397.

Bandettini PA, Jesmanowicz A, Wong EC, Hyde JS. Processing strategies for time course data sets in functional MRI of the human brain. Magn Reson Med 1993;30:161–173.

Bandettini PA, Petridou N, Bodurka J. Direct detection of neuronal activity with MRI: fantasy, possibility, or reality? Applied Magn Reson 2005; 29(1):65–88.

Barth M, Breuer F, Koopmans PJ, Norris DG, Poser BA. Simultaneous Multislice (SMS) Imaging Techniques. Magn Reson Med 2016;75:63-81.

Bhattacharyya PK, Lowe MJ. Cardiac-induced physiologic noise in the tissue is a direct observation of cardiac-induced fluctuations. Magn Reson Imaging 2004;22:9–13.

Birn RM, Diamond JB, Smith MA, Bandettini PA. Separating respiratory-variation-related fluctuations from neuronal-activity-related fluctuations in fMRI. Neuroimage 2006;31,1536–1548.

Blaimer M, Breuer FA, Mueller MF, Heidemenn RM, Griswold MA, Jakob PM. SMASH, SENSE, PILS, GRAPPA How to Choose the Optimal Method. Magn Reson Imaging 2004;15(4),223–236.

Blaimer M, Choli M, Jakob PM, Griswold MA, Breuer FA. Multiband Phase Constrained Parallel MRI. Magn Reson Med 2013;69(4):974-980.

Blaimer M, Gutberlet M, Kellman P, Bruer FA, Kostler H, Griswold MA. Virtual Coil Concept for Improved Parallel MRI Employing Conjugate Symmetric Signals. Magn Reson Med 2009;61: 93–102.

Bloch F. Nuclear Induction. Phys Rev 1946; 70:460-474.

Breuer FA, Blaimer M, Heidemenn RM, Mueller MF, Griswold MA, Jakob PM. Controlled Aliasing in Parallel Imaging Results in Higher Acceleration (CAIPIRINHA) for Multi-Slice Imaging. Magn Reson Med 2005;53:684–691.

Breuer FA, Blaimer M, Heidemenn RM, Griswold MA, Jakob PM. Controlled Aliasing in Parallel Imaging Results in Higher Acceleration (CAIPIRINHA). MAGNETOM Flash 2012;135–142.

Bruce IP, Karaman MM, Rowe DB. A statistical examination of the SENSE reconstruction via an isomorphism representation. Magn Reson Imaging 2011;29,1267–1287.

Bruce IP, Rowe DB. Quantifying the statistical impact of GRAPPA in fcMRI data with a real-valued isomorphism. IEEE Trans Med Imaging 2014;33,495–503.

Bodurka J, Bandettini PA. Toward direct mapping of neuronal activity: Mri detection of ultraweak, transient magnetic field changes. Magn Reson Med 2002; 47(6):1052–8.

Bodurka J, Jesmanowicz A, Hyde JS, Xu H, Estkowski L, Li SJ. Current-induced magnetic resonance phase imaging. J Mag Reson 1999; 137(1):265–71.

Cauley SF, Polimeni J, Bhat H, Wald LL, Setsompop K. Interslice Leakage Artifact Reduction Technique for Simultaneous Multislice Acquisitions. Magn Reson Med 2014;72:93–102.

Chai XJ, Castanon AN, Ongur D, Whitfield-Gabrieli S. Anticorrelations in resting state networks without global signal regression. Neuroimage 2012; 16;59(2):1420-28.

Cordes D, Haughton VM, Arfanakis K, Carew JD, Turski PA, Quigley MA, Meyerand ME. Frequencies contributing to functional connectivity in the cerebral cortex in "resting-state" data. Am J Neuroradiol 2001;22:1326–1333.

Cox RW, Jesmanowicz A, Hyde JS. Real-time functional magnetic resonance imaging. Magn Reson Med 1995;33:230–236.

Chen L, Vu A, Xu J, Moeller S, Ugurbil K, Yacoub E, Feinberg DA. Evaluation of Highly Accelerated Simultaneous Multi-Slice EPI for FMRI. Neuroimage 2015; 104: 452-59.

Davey CE, Grayden DB, Egan GF, Johnston LA. Filtering induces correlation in fMRI resting state data. Neuroimage 2013;64,728–740.

Feinberg DA, Moeller S, Smith SM, Auerbach E, Ramanna S, Glasser MF, Miller KL, Ugurbil K, Yacoub E. Multiplexed echo planar imaging for sub-second whole brain fMRI and fast diffusion imaging. PLoS ONE 2010;5:e15710.

Feinberg DA, Setsompop K. Ultra-fast MRI of the human brain with simultaneous multi-slice imaging. J Magn Reson 2013;229:90–100.

Feng Z, Caprihan A, Blagoev KB, Calhoun VD. Biophysical modeling of phase changes in BOLD fMRI. Neuroimage 2009;47(2):540-8.

Friston KJ, Josephs O, Zarahan E, Holmes AP, Rouquette S, Poline JB. To smooth or not to smooth? Bias and efficiency in fMRI time-series analysis. Neuroimage 2000;12, 196–208.

Griswold MA, Jakob PM, Heidemann RM, Nittka M, Jellus V, Wang J, Kiefer B, Haase A. Generalized Autocalibrating Partially Parallel Acquisitions (GRAPPA). Magn Reson Med 2002;47:1202–1210.

Glasser MF, Sotiropoulos SN, Wilson JA, Coalson TS,Fischl B, Andersson JL, Xu J, Jbabdi S, Webster M, Polimeni JR, Van Essen DC, Mark Jenkinson, The minimal preprocessing pipelines for the Human Connectome Project. NeuroImage 2013; 80: 105-124.

Glover GH. Phase-Offset Multiplanar (POMP) volume imaging - a new technique. J Magn Reson Imaging 1991;1:457–461.

Glover GH, Li TQ, Ress D. Image-based method for retrospective correction of physiological motion effects in fMRI: RETROICOR. Magn Reson Med 2000;44,162–167.

Gudbjartsson H, Patz S. The Rician Distribution of Noisy MRI Data. Magn Reson Med 1995;34(6):910-914.

Haacke EM, Brown R, Thompson M, Venkatesan R. Magnetic resonance imaging: physical principles and sequence design. New York, NY, USA: John Wiley and Sons 1999.

Hahn AD, Nencka AS, Rowe DB. Improving robustness and reliability of phase-sensitive fMRI analysis using temporal off resonance alignment of single-echo time series (TOAST). Neuroimage 2009; 44:742–752.

Hahn AD, Nencka AS, Rowe DB. Enhancing the utility of complex-valued functional magnetic resonance imaging detection of neurobiological processes through post acquisition estimation and correction of dynamic $B_0$ errors and motion. Hum Brain Mapp 2012;33:288–306.

Heller L, Barrowe B, George J. Modeling direct effects of neural current on MRI. Hum Brain Mapp, 2007; 30:1–12.

Hoogenraad FG, Pouwels PJ, Hofman MB, Reichenbach JR, Sprenger M, Haacke EM. Quantitative differentiation between BOLD models in fMRI. Magn Reson Med 2001;45;233–46.

Hu X, Le TH, Parrish T, Erhard P. Retrospective estimation and correction of physiological fluctuation in functional MRI. Magn Reson Med 1995;34, 201–212.

Karaman MM, Bruce IP, Rowe DB. Incorporating relaxivities to more accurately reconstruct MR images. Magn Reson Imaging 2015;33:85–96.

Karaman MM, Bruce IP, Rowe DB. Quantification of the Statistical Effects of Spatiotemporal Processing of Nontask fMRI Data. Brain. Connect. 2014; 4,649-61.

Klein A, Andersson J, Ardekani BA, Ashburner J, Avants B, Chiang M, Christensen GE, Collins DL, Gee J, Hellier P, Song JH, Jenkinson M, Lepage C, Rueckert D, Thompson P, Vercauteren T, Woods RP, Mann JJ, Parsey RV. Evaluation of 14 nonlinear deformation algorithms applied to human brain MRI registration. Neuroimage 2009;46(3):786–802.

Kociuba MC, Rowe DB. Complex-Valued Time-Series Correlation Increases Sensitivity in FMRI Analysis. Magn Reson Imaging. 2016: 34; 765-770.

Larkman DJ, Hajnal JV, Herlihy AH, Coutts GA, Young IR, Ehnholm G. Use of multicoil arrays for separation of signal from multiple slices simultaneously excited. Magn Reson Imag 2001;13:313-317.

Larkman DJ, deSouza NM, Bydder M, Hajnal JV. An Investigation into the Use of Sensitivity Encoded Techniques to Increase Temporal Resolution in Dynamic Contrast-Enhanced Breast Imaging. Magn Reson Imag 2001;14:329–335.

Larkman DJ, Nunes RG. Parallel magnetic resonance imaging. Phys Med Biol 2007;52:15– 55.

Lauterbur PC. Image formation by induced local interactions: Examples employing nuclear magnetic resonance. Nature 1973; 242: 190–191.

Mansfield P. Multi-planar image formation using NMR spin echoes. Journal of Physics C: Solid State Physics. 1977;10:L55.

Mansfield P, Maudsley AA. Medical imaging by NMR. Br J Radiol. 1977;50:188–94.

Menon RS. Postacquisition suppression of large-vessel BOLD signals in high-resolution fMRI. Magn Reson Med 2002;47:1–9.

Moeller S, Yacoub E, Olman CA, Auerbach E, Strupp J, Harel N, Ugurbil K. Multiband multislice GE-EPI at 7 Tesla, with 16-fold acceleration using partial parallel imaging with application to high spatial and temporal whole-brain fMRI. Magn Reson Med 2010;63:1144–1153.

Moeller S, Junqian X, Auerbach E, Yacoub E, Ugurbil K. Signal Leakage(L-Factor) as a Measure for Parallel Imaging Performance Among Simultaneously Multi- Slice (SMS) Excited and Acquired Signals. ISMRM 20th Annual Meeting; 2012. p. 0519.

Muller S. Multifrequency selective RF pulses for multislice MR imaging. Magn Reson Med 1998;6:364–371.

Murphy K, Birn RM, Handwerker DA, Jones TB, Bandettini PA. The impact of global signal regression on resting state correlations: are anti-correlated networks introduced? Neuroimage 2009; 44:893-905.

Nencka AS, Rowe DB. Reducing the unwanted draining vein BOLD contribution in fMRI with statistical post-processing methods. Neuroimage. 2007;37:177–188.

Nencka AS, Hahn AD, Rowe DB. The use of three navigator echo in Cartesian EPI reconstruction reduces Nyquist ghosting. Proc Int Soc Mag Reson Med 2008; 16:3032.

Nencka AS, Hahn AD, Rowe DB. A mathematical model for understanding statistical effects of k-space (AMMUST-k) preprocessing on observed voxel measurements in fcMRI and fMRI. J Neurosci Methods 2009;181:268–282.

Nunes RG, Hajnal JV, Golay X, Larkman DJ. Simultaneous slice excitation and reconstruction for single shot EPI. In Proceedings of the 14th Annual Meeting of ISMRM, Seattle, Washington, USA, 2006. Abstract 293.

Ogawa S, Lee TM, Kay AR, Tank DW. Brain magnetic resonance imaging with contrast dependent on blood oxygenation. Proc Natl Acad Sci USA 1990;87:9868–9872.

Pruessmann KP, Weiger M, Scheidegger MB, Boesiger P. SENSE: Sensitivity Encoding for fast MRI. Magn Reson Med 1999;42:952–962.

Rowe DB, Logan BR. A complex way to compute fMRI activation. Neuroimage 2004;23:1078–92.

Rowe, D.B., Logan, B.R. Complex fMRI analysis with unrestricted phase is equivalent to a magnitude-only model. Neuroimage 2005; 24: 603-606.

Rowe DB. Modeling both the magnitude and phase of complex-valued fMRI data. Neuroimage 2005;25:1310–24.

Rowe DB, Nencka AS, Hoffmann RG. Signal and noise of Fourier reconstructed fMRI data. J Neurosci Methods 2007;159:361–369.

Rowe DB, Nencka AS. Induced Correlation In FMRI Magnitude Data From *k*-Space Preprocessing. Proc Intl Soc Mag Reson Med 2009; 17:1721.

Rowe DB, Bruce IP, Nencka AS, Hyde JS, Kociuba MC. Separation of parallel encoded complex-valued slices (SPECS) from a single complex-valued aliased coil image. Magn Reson Imaging 2016;34:349–69.

Saad Z, Gotts SJ, Murphy K, Chen G, Jo HJ, Martin A, Cox RW. Trouble at rest: how correlation patterns and group differences become distorted after global signal regression. Brain. Connect. 2012;2(1):25-32.

Setsompop K, Gagoski BA, Polomeni JR, Witzel T, Wedeen VJ, Wald LL. Blipped-Controlled Aliasing in Parallel Imaging (blipped-CAIPI) for simultaneous multi-slice EPI with reduced g-factor penalty. Magn Reson Med. 2012;67(5):1210–1224.

Setsompop K, Cohen-Adad J, Gagoski BA, Raij T, Yendiki A, Keil B, Wedeen VJ, Wald LL. Improving diffusion MRI using simultaneous multi-slice echo planar imaging. Neuroimage 2012;63:569–580.

Severini, T.A. Likelihood methods in statistics. Oxford: Oxford University Press, 2001.

Shmueli K, van Glederen P, de Zwart JA, Horovitz SG, Fukunaga M, Jansma JM, Duyn JH. Low-frequency fluctuation in the cardiac rate as a source of variance in the resting-state fMRI BOLD signal. Neuroimage 2007;38:306–320.

Sodickson, D.K., Manning, W.J. Simultaneous acquisition of spatial harmonics (SMASH): fast imaging with radiofrequency coil arrays. Magn. Reson. Med. 1999; 38: 591-603.

Souza SP, Szumowski J, Dumoulin CL, Plewes DP, Glover G. SIMA: simultaneous multislice acquisition of MR images by Hadamard-encoded excitation. Comput Assist Tomogr 1988;12:1026–1030.

Sylvester JJ. Thoughts on Orthogonal Matrices, Simultaneous Sign-Successions, and Tessellated Pavements in Two or More Colours, with Applications to Newton's Rule, Ornamental Tile-Work, and the Theory of Numbers. Phil. Mag. 1867; 34, 461-475.

Todd N, Moeller S, Auerbach EJ, Yacoub E, Flandin G, Weiskopf N. Evaluation of 2D multiband EPI imaging for high resolution, whole brain task-based fMRI studies at 3T: Sensitivity and slice leakage artifacts. NeuroImage 2016;124:32-42.

Thulborn KR, Waterton JC, Matthews PM, Radda GK. Oxygenation dependence of the transverse relaxation time of water protons in whole blood at high field. Biochem Biophys Acta 1982; 714:265-70.

Ugurbil K, Xu J, Auerbach EJ, Moeller S, Vu AT, Duarte-Carvajalino JM, Lenglet C, Wu X, Schmitter S, Van de Moortele PF, Strupp J, Sapiro G, De Martino F, Wang D, Harel N, Garwood M, Chen L, Feinberg DA, Smith SM, Miller KL, Sotiropoulos SN, Jbabdi S, Andersson JLR, Behrens TEJ, Glasser MF, Van Essen DC, Yacoub E. Pushing spatial and temporal resolution for functional and diffusion MRI in the Human Connectome Project. . NeurorImage 2013;80:80-104.

Van Essen DC, Smith SM, Barch DM, Behrens TEJ, Yacoub E, Ugurbil K. The WU-Minn Human Connctome Project: An Overview. NeurorImage 2013;80:62-79.

Weiger M, Pruessman KP, Boesiger P. 2D SENSE for faster 3D MRI. Magn Reson Mat in Phys, Bio, and Med 2002;14:10–19.

Xu J, Moeller S, Auerbach EJ, Strupp J, Smith SM, Feinberg DA, Yacoub E, Ugurbil K. Evaluation of slice accelerations using multiband echo planar imaging at 3 T. Neuroimage. 2013; 83:991–1001.

Ying L, Liu B, Steckner MC, Wu G, Wu M, Li SJ. A statistical approach to SENSE regularization with arbitrary *k*-space trajectories. Magn Reson Med 2008;60:414–21.

Zhao F, Jin T, Wang P, Hu X, Kim SG. Sources of phase changes in BOLD and CBV-weighted fMRI. Magn Reson Med 2007;57:520–7.

Zhao K, Zaitsiev M, Bao S. Reliable Two-Dimensional Phase Unwrapping Method Using Region Growing and Local Linear Estimation. Magn Reson Med 2009;62;1085–90.